

LUDWIG-MAXIMILIANS-UNIVERSITÄT MÜNCHEN

Large-Scale Structure Probes of Accelerated Expansion

DISSERTATION

Steffen Hagstotz



Munich 2018

Large-Scale Structure Probes of Accelerated Expansion

Steffen Hagstotz

Dissertation
an der Fakultät für Physik
der Ludwig-Maximilians-Universität
München

vorgelegt von
Steffen Hagstotz
aus Vaihingen/Enz

München, den 25. Juli 2018

Erstgutachter: Prof. Dr. Jochen Weller

Zweitgutachter: Dr. Martin Kerscher, PD

Tag der mündlichen Prüfung: 5. September 2018

LUDWIG-MAXIMILIANS-UNIVERSITÄT MÜNCHEN

Zusammenfassung

Large-Scale Structure Probes of Accelerated Expansion

Die Kosmologie hat in den letzten beiden Dekaden weitreichende Fortschritte gemacht. Wir sind heute in der Lage, die Geschichte des Universums mit beeindruckender Präzision zu rekonstruieren. Eine Vielzahl von bahnbrechenden Beobachtungen hat zur Entwicklung des kosmologischen Standardmodells geführt: Λ CDM.

Doch trotz dieser Erfolge bleiben noch viele Fragen offen: ist die beobachtete beschleunigte Expansion des Universums auf eine kosmologische Konstante zurück zu führen? Falls nicht, was ist die Natur der dunklen Energie, die diesen Prozess antreibt? Wird Gravitation auf allen Skalen von Einsteins Allgemeiner Relativitätstheorie beschrieben?

Diese Dissertation versucht zur Beantwortung dieser Fragen mithilfe der Struktur der Materieverteilung im Universum beizutragen. Eine besonders wichtige Rolle spielen hierbei Galaxienhaufen, da ihre Anzahl empfindlich von der zugrundeliegenden Dynamik des Dichtefeldes abhängt. Gleichzeitig sind sie als massivste Strukturen im Universum über riesige Distanzen sichtbar und erlauben es somit, Theorien mit Beobachtungen zu konfrontieren.

Nach einer Einführung in die moderne Kosmologie in Kapitel 1, untersuche ich die Möglichkeit, mit der Anzahl der beobachteten Galaxienhaufen mehr über die Parameter des Λ CDM-Modells zu lernen. In Kapitel 2 werden die Ergebnisse des Planck-Satelliten diskutiert, der eine Vielzahl von Haufen entdeckt hat. Dabei diskutiere ich das theoretische Modell, das notwendig ist um aus der beobachteten Häufigkeit kosmologische Schlussfolgerungen zu ziehen. Dabei werden einige Verbesserungen vorgeschlagen, die in meine Vorhersagen für die Galaxienhaufen-Analysen des momentan geplanten CORE-Satelliten einfließen.

In Kapitel 3 werden Parametrisierungen vorgestellt, um Abweichungen von Standard-Gravitation möglichst modellunabhängig zu messen. Zunächst wird das Problem in der Newtonschen Theorie diskutiert, bevor wir einen relativistischen Zugang finden der es erlaubt, die kosmologischen Störungsgleichungen im frühen Universum konsistent für parametrische Modelle zu lösen. Beispielfhaft diskutiere ich eine modifizierte Gravitationstheorie, $f(R)$, und wie sich die Zeitentwicklung des Dichtefeldes auf die zuvor präsentierte Parametrisierung abbilden lässt.

Anschliessend wird in Kapitel 4 eine theoretische Massenfunktion entwickelt, die es erlaubt, die erwartete Häufigkeit von Galaxienhaufen in $f(R)$ -Theorien vorherzusagen und damit nach Abweichungen von Standardgravitation zu suchen. Dabei wird die Rolle von Neutrinos miteinbezogen, die den erwarteten Effekt von modifizierter Gravitation kaschieren können. Ich diskutiere die Auswirkung anhand von Vorhersagen für derzeitige und zukünftige Beobachtungen. Diese demonstrieren, dass Neutrinos in der Suche nach modifizierter Gravitation nicht zu vernachlässigen sind.

Abstract

Large-Scale Structure Probes of Accelerated Expansion

Cosmology made impressive strides forward in the last two decades. Today, we are able to reconstruct the history of the Universe to astonishing precision. A multitude of ground-breaking observations lead to the establishment of a cosmological standard model: Λ CDM.

Despite the success, many questions remain: is the observed accelerated expansion of the Universe caused by a cosmological constant? If this is not the case, what is the nature of dark energy driving this process? Is gravity described by Einstein's theory of general relativity on all scales?

This dissertation tries to approach these questions by analysing the structure of the matter distribution in the Universe. Clusters of galaxies are of special interest here, since their abundance depends sensitively on the dynamics of the underlying density field. At the same time, they are observable over vast distances, which allows to confront theory with measurements.

After an introduction to modern cosmology in Chapter 1, I discuss the possibilities to learn more about the Λ CDM parameters with clusters of galaxies. In Chapter 2 I present the cluster results from the Planck satellite and develop the theoretical model used to draw cosmological conclusions from the observed cluster catalogue. Various improvements to previously employed methods are discussed, that are then incorporated in cosmological cluster forecasts for the currently planned CORE satellite.

In Chapter 3 various parametric methods to detect deviations from standard gravity without assuming specific models are discussed. Starting from a framework in Newtonian theory, it is then extended to a fully relativistic setting that allows to solve the cosmological perturbation equations for the early Universe in parametric extensions of the standard model. As an example I discuss a specific modified gravity theory, $f(R)$, and present a mapping between the evolution of the density field in the modified gravity model and the parametric approach.

Subsequently, in Chapter 4 I develop a theoretical mass function that allows to predict the cluster number counts in $f(R)$ theories to search for deviations from standard gravity in the observed abundance. The role of neutrinos is included in the framework, since they can potentially mask effects of modified gravity. I demonstrate the degeneracy with various forecasts for current and future cluster surveys, which shows that neutrinos can not be neglected in searches for modified gravity.

Contents

1	Introduction	1
1.1	The homogeneous universe	2
1.1.1	The cosmological constant problem	6
1.1.2	Scalar fields as dark energy	9
1.2	The cosmic density field	11
1.2.1	Gaussian random fields	11
1.2.2	Ergodic principle and cosmic variance	13
1.2.3	Linear growth of structures	14
1.3	The non-linear Universe	16
1.4	Outline of this work	18
2	Cosmology with SZ cluster surveys	21
2.1	The Sunyaev Zel'dovich effect	21
2.2	The Planck cluster sample	23
2.2.1	Modelling of number counts	23
2.2.2	Likelihood and correlated cluster abundance	28
2.2.3	Planck cluster cosmology	34
2.3	From Planck to CORE	37
2.3.1	CORE cluster abundance	38
2.3.2	Cosmological constraints from CORE	39
2.4	Conclusion	43
3	Structure growth in parametrised modified gravity	45
3.1	Relativistic perturbations	46
3.1.1	Metric decomposition	46
3.1.2	Gauge freedom	47
3.2	Parametrised growth equation	49
3.3	Parametrised Einstein equations	50
3.4	$f(R)$ gravity	54
3.5	Conclusion	57
4	Halo Mass Function for $f(R)$ Gravity and Massive Neutrinos	61
4.1	Introduction	61
4.2	The DUSTGRAIN- <i>pathfinder</i> simulations	62
4.3	Joint mass function	64
4.3.1	Diffusing, drifting barrier	66
4.3.2	Non-markovian corrections	67
4.3.3	Spherical collapse in modified gravity	68
4.3.4	Neutrinos	71
4.3.5	Halo bias and cluster clustering	73
4.3.6	Calibration and comparison	74
4.4	Forecasts	77
4.4.1	Optical cluster surveys	79

4.4.2	SZ cluster surveys	82
4.4.3	Searching for modified gravity with other parametrisations	85
4.5	Cluster kinematics in modified gravity	86
4.6	Conclusion	87
5	Summary and outlook	89
	Acknowledgements	93
	Bibliography	95

List of Figures

1.1	Cosmological distance measures	6
1.2	The sky seen by Planck	11
1.3	Linear growth	15
1.4	Evolution of the cluster abundance	17
2.1	Sunyaev-Zel'dovich distortion of the CMB blackbody spectrum	22
2.2	Multiwavelength observations of the Shapley supercluster	24
2.3	Planck sky-averaged instrumental noise	25
2.4	Planck completeness	27
2.5	Planck limiting mass and theoretical cluster redshift distribution	28
2.6	Halo power spectrum and shot noise	29
2.7	Cross-correlation coefficient for neighboring redshift bins	33
2.8	Theoretical and measured Planck SZ cluster redshift distribution	35
2.9	Planck cluster constraints on $\Omega_m - \sigma_8$	36
2.10	Mass bias $(1 - b_M)$ for various measurements	37
2.11	Sky-averaged noise for CORE	38
2.12	Limiting mass and redshift distribution of the CORE cluster sample	39
2.13	Cosmological constraints from CORE	40
2.14	Sample variance effect on CORE	41
2.15	Dark energy constraints from CORE	42
3.1	Parametrised linear growth function	50
3.2	Matter power spectrum in $f(R)$ gravity	55
3.3	CMB temperature anisotropy in $f(R)$ gravity	57
3.4	Constraints on parametrised modified gravity from KiDS	58
4.1	Effect of the barrier width on halo abundance	66
4.2	Screening mass and resulting changes in the collapse barrier and halo abundance	69
4.3	Evolution of the threshold with z and f_{R0}	70
4.4	Neutrino effect on the collapse threshold and resulting halo abundance	71
4.5	Combined ν and $f(R)$ collapse threshold	72
4.6	Effect of massive neutrinos and $f(R)$ on the linear bias	73
4.7	Comparison of virial and calibrated halo mass function	74
4.8	Calibrated halo mass function compared to $f(R)$ simulations	76
4.9	Comparison of the joint halo mass function with simulations	78
4.10	Expected constraints on $\Omega_m - f_{R0}$ from shallow or deep optical cluster surveys	80
4.12	Evolution of cluster counts with redshift and richness for a shallow or deep optical cluster survey	81
4.13	Effect of $f(R)$ on the limiting mass of the Planck cluster sample	83
4.14	Effect of massive neutrinos and $f(R)$ on the Planck cluster redshift distribution	84

4.15	Posterior distribution for a $f(R)$ mock sample analysed assuming a w CDM cosmology	85
4.16	Richness distribution of an $f(R)$ mock sample compared to bestfit w CDM distribution	86
4.17	Halo Velocity Dispersions in $f(R)$	87

List of Tables

1.1	Cosmological density parameters	5
2.1	Planck cluster nuisance parameters	34
2.2	Dark energy constraints from CORE compared to other future experiments	43
4.1	Parameters of the DUSTGRAIN- <i>pathfinder</i> simulations	63
4.2	Fiducial values for the virial $f(R)$ mass function collapse barrier	69
4.3	Calibrated barrier parameters	75
4.4	Complementary mock data sets for $f(R)$ constraints	78
4.5	Expected $f(R)$ constraints from optical cluster surveys	82

“By convention there is sweetness, by convention bitterness, by convention color, in truth only atoms and the void.”

Democritus

Chapter 1

Introduction

Cosmology is nothing if not ambitious. Its goal is to understand the evolution of the whole Universe as a physical system spanning about 14 billion years. On this long journey, cosmology encounters a large variety of physical processes, from particle physics shaping the early universe briefly after the hot big bang, to gas collapsing under its own gravity to form galaxies, stars, planets and finally observers.

We live now in an era in which the big picture seems to be consolidated and cosmology has produced its own standard model, Λ CDM. This was made possible by unprecedented advances in observations: the revolutionary discovery of the accelerated expansion of the universe by supernovae measurements, the determination of the cosmic microwave background anisotropy to incredible precision, and the currently ongoing effort to map the large-scale structure. All of those datasets – from the very early times when the Universe was only 300000 years old, to the cosmic web we see in observations almost 14 billion years later; from smallest scales governing the primordial formation of elements, to filaments spanning many megaparsecs – are explained by a surprisingly simple framework.

However, the picture of the Universe implied by Λ CDM is astonishing. It predicts that its namesakes, a cosmological constant Λ and cold dark matter, account for 95% of its energy content. Neither of these components has ever been seen in a laboratory before. Their observation is at the moment the only manifestation of physics beyond the standard model of particle physics. This makes cosmology a crucial part of the search for a more fundamental theory of nature, and the Universe itself provides an environment to test theories beyond anything we can ever accomplish in earthbound experiments.

Even beyond the challenge to find a physical candidate for the measured dark components, nagging questions remain. The Λ CDM framework works very well in terms of a phenomenological description, but it is also plagued by several suspicious coincidences. Why are the densities of dark matter and dark energy so similar today? Why is the cosmological constant so small, contrary to our expectations? We do not have satisfying answers to these questions, but they lead us to develop modifications of the model. They can either take the form of new contributions to the Universe's energy budget, or it is possible that we are witnessing the breakdown of gravity as described by general relativity itself. How to confront theories of dark energy or modified gravity with observations will be a major topic of this thesis.

This chapter briefly introduces various underlying concepts of modern cosmology and we will develop various tools and notations that are used throughout this work. We start by providing an overview over homogeneous cosmology in Sec 1.1, with particular focus on the cosmological constant and fundamental theoretical problems associated with it. These problems will be the main motivation for large parts of this thesis. Sec. 1.2 contains a brief summary of the theory of cosmic density fields, and we

discuss their initial statistics and the linear evolution driven by an interplay of gravity, expanding space and the fluid equations. In Sec 1.3 we will move into the non-linear regime and introduce the spherical collapse framework. It allows us to describe how the highest peaks of the density field decouple from the background expansion and collapse under their own gravity to form clusters of galaxies, which are the largest observable structures in the Universe today. We will close the introduction with an overview over this thesis in Sec. 1.4

1.1 The homogeneous universe

Throughout this work, we will adapt the Copernican principle and assume that the Universe appears homogeneous and isotropic on scales larger than a few hundred megaparsecs to a freely-falling observer. The only interaction relevant on these scales is gravity. The gravitational field *is* spacetime, characterised by the metric $g_{\mu\nu}$ ¹, and its dynamics are governed by general relativity (GR) through the Einstein field equations²

$$G_{\mu\nu} - \Lambda g_{\mu\nu} = 8\pi G T_{\mu\nu}, \quad G_{\mu\nu} = R_{\mu\nu} - \frac{R}{2} g_{\mu\nu}, \quad (1.1)$$

that connect the geometry encoded in the Einstein tensor $G_{\mu\nu}$ to the matter content of spacetime given by the energy-momentum tensor $T_{\mu\nu}$. The cosmological constant term Λ is crucial for the evolution of the universe today, and can either be interpreted as part of the geometry of spacetime, or as contribution to the energy-momentum tensor where it is called *dark energy*. While both points of view are completely equivalent in Eq. 1.1, the physical interpretation is quite different. We will come back to this distinction in Sec. 1.1.1.

Under the symmetry assumptions implied by the Copernican principle, the solution to the field equations is given by the Friedmann-Lemaître-Robertson-Walker (FLRW) metric³. In spherical coordinates, we can write the line element as

$$ds^2 = -dt^2 + a^2(t) \left[\frac{dr^2}{1 - kr^2} + r^2 d\Omega^2 \right], \quad (1.2)$$

where the only possible dynamic in an isotropic and homogeneous spacetime is a uniform spatial expansion, given by the scale factor $a(t)$. This expression allows for constant spatial curvature characterised by the parameter k .

The only energy-momentum tensor compatible with homogeneity and isotropy is that of an ideal fluid with density ρ and pressure p

$$T_{\mu\nu} = (\rho + p)u_\mu u_\nu - g_{\mu\nu} p, \quad (1.3)$$

where we introduced the 4-velocity $u_\mu = a\delta_\mu^0$ and the density and pressure will generally consist of a sum from various species such as matter and photons. The Einstein tensor $G_{\mu\nu}$ fulfills the Bianchi identity

$$\nabla^\mu G_{\mu\nu} = 0, \quad (1.4)$$

¹Greek indices refer to the four spacetime components, while we denote spatial three-vectors with latin indices.

²We use natural units $c = \hbar = 1$ throughout this work.

³We adopt the $(-, +, +, +)$ signature of the metric.

and $\nabla^\mu g_{\mu\nu} = 0$, which implies that the energy-momentum tensor is covariantly conserved by the Einstein equations

$$\nabla^\mu T_{\mu\nu} = \partial^\mu T_{\mu\nu} + \Gamma_{\mu\alpha}^\mu T_\nu^\alpha - \Gamma_{\mu\nu}^\alpha T_\alpha^\mu = 0. \quad (1.5)$$

This expression differs from a regular conservation law in static space by the connection coefficients Γ , the Christoffel symbols

$$\Gamma_{\alpha\beta}^\mu = \frac{g^{\mu\sigma}}{2} (\partial_\beta g_{\sigma\alpha} + \partial_\alpha g_{\sigma\beta} - \partial_\sigma g_{\alpha\beta}), \quad (1.6)$$

which account for the geometry of spacetime. This expression only holds locally, in GR there are no globally conserved quantities mainly due to the problem of finding a unique definition of *global* in a dynamic spacetime.

The time evolution of the scale factor – and with that, of the entire Universe on large scales – can be derived by inserting the metric 1.2 into the field equations 1.1. From the 00-component, we get

$$\frac{\dot{a}^2 + k}{a^2} = \frac{8\pi G}{3} (\rho + \Lambda), \quad (1.7)$$

and we denote time derivatives with dots, $\dot{a} \equiv da/dt$. Using 1.7 together with the trace of the Einstein equations yields an expression for the second derivative of the scale factor, the acceleration equation

$$\frac{\ddot{a}}{a} = -\frac{4\pi G}{3} (\rho + 3p) + \frac{\Lambda}{3}. \quad (1.8)$$

These are the two Friedmann equations. They are often expressed in terms of the Hubble function $H \equiv \dot{a}/a$ instead of a . The line element 1.2 is invariant under the rescaling

$$a \rightarrow \alpha a, \quad r \rightarrow \frac{r}{\alpha}, \quad k \rightarrow \alpha^2 k, \quad (1.9)$$

and we can use this freedom to normalise $a(t_0) = 1$ at present time, with the corresponding Hubble constant $H_0 \equiv 100 \times h \text{ km s}^{-1} \text{ Mpc}^{-1}$ conventionally expressed by the parameter h , and current measurements give $h = 0.6774 \pm 0.0049$ (Planck Collaboration et al., 2016a). The scale factor a is therefore dimensionless, while r and $k^{-1/2}$ have units of length. Note that the Hubble distance $H_0^{-1} \approx 3 \text{ Gpc}/h$ sets a convenient scale that is of the order of the size of the observable Universe.

Since the gravitational field is constructed to obey the Bianchi identity, we can also recover the local energy-momentum conservation by combining both Friedmann equations to get

$$\frac{d}{dt} (a^3 \rho) + p \frac{d}{dt} (a^3) = 0, \quad (1.10)$$

in analogy to the first law of thermodynamics, $dU + pdV = 0$, expressing the change in internal energy of a fluid expanding with the Hubble flow. Any heat flux dQ has to vanish since it would violate the assumption of isotropy. We can express the same fact equivalently in the form of a continuity equation

$$\dot{\rho} + 3H(a)(\rho + p) = 0, \quad (1.11)$$

and use whichever relation is more convenient at the time. Noting that the Hubble parameter defines a critical density scale

$$\rho_{\text{crit}} = \frac{3H_0^2}{8\pi G}, \quad (1.12)$$

we can express the energy content of the Universe in terms of dimensionless density parameters

$$\Omega(a) \equiv \frac{\rho(a)}{\rho_{\text{crit}}} = \frac{8\pi G\rho}{3H_0^2}. \quad (1.13)$$

This allows us to write the first Friedmann equation 1.7 in the form

$$\frac{H^2}{H_0^2} = \Omega_\gamma a^{-4} + \Omega_m a^{-3} + \Omega_K a^{-2} + \Omega_\Lambda, \quad (1.14)$$

where all parameters are measured at present time, Ω_m is the non-relativistic matter content consisting of baryons and dark matter, Ω_γ the relativistic contribution made up of photons and neutrinos, and we defined the corresponding curvature- and Λ -parameters

$$\Omega_K \equiv -\frac{k}{H_0^2}, \quad \Omega_\Lambda \equiv \frac{\Lambda}{3H_0^2}. \quad (1.15)$$

Keep in mind that the fluid analogy should not be taken too seriously for these components, e.g. Ω_K is negative for positive curvature. Since we normalised $a(t_0) = 1$ and $H(t_0) = H_0$, all contributions on the right hand side of Eq. 1.14 add up to 1. Hence Ω_i can be thought of as the fraction of the Universe's energy content in the form of the respective contribution. All terms scale with different powers of the scale factor a , therefore they will be dominant throughout different eras of the Universe. The nature of this scaling lies within the equation of state

$$p_i = w_i \rho_i, \quad (1.16)$$

connecting density and pressure in the energy-momentum tensor for every species. This additional relation closes the system of Friedmann equations 1.7 and 1.8 and determines the evolution of the smooth background once the initial conditions Ω_i are specified. In general, the $\Omega(a)$ dependance can be written as

$$\Omega_i(a) = \Omega_i(a_0) a^{-3(1+w_i)}. \quad (1.17)$$

Thus we have $w_\gamma = 1/3$ for radiation and relativistic particles, $w_m = 0$ for non-relativistic matter and a cosmological constant requires $w_\Lambda = -1$. Its associated energy density is constant with time and does not dilute as the universe expands, which serves as a reminder of the fact that conservation laws in GR only hold locally.

Measurements suggest that we live in a spatially flat Universe (Planck Collaboration et al., 2016a; Alam et al., 2017) with a curvature scale large compared to the Hubble distance $k^{-1/2} \gg H_0^{-1}$, and we will set $k = 0$ from here on. At present time radiation ceased to be a major contribution to the energy budget, so the only relevant terms left in eq. 1.7 are proportional to Ω_m , largely consisting of dark matter, and Ω_Λ . Interestingly, we live in a time when both contributions are relevant, just before the cosmological constant will completely dominate the expansion of the Universe as matter is increasingly diluted. We show the most precise current measurements of the density parameters in Tab. 1.1.

TABLE 1.1: Current constraints on the density parameters from Planck Collaboration et al., 2016a. The radiation density was calculated from the measured temperature of the cosmic microwave background $T_{\text{CMB}} = 2.7255$ K. The contribution from curvature is constrained to be very small.

Ω_m	Ω_Λ	Ω_γ	Ω_k
0.3089 ± 0.0062	0.6911 ± 0.0062	$(5.39 \pm 0.07) \times 10^{-5}$	$0.8^{+4.0}_{+3.9} \times 10^{-3}$

The wavelength λ of radiation propagating through an expanding background is stretched and it loses energy on the way to the observer. This effect is observable as a *redshift* $z \equiv \Delta\lambda/\lambda$ for distant objects, connected to the scale factor by the relation

$$a = \frac{1}{1+z}, \quad (1.18)$$

which, together with a distance measurement, allows to reconstruct the expansion history of the universe (e.g. Riess et al., 1998; Perlmutter et al., 1999).

In a dynamic spacetime however, there is no unique notion of distance. The measure will ultimately depend on the quantity we are considering. Often it is convenient to define the *comoving distance* χ , which is constant for two objects moving with the Hubble flow

$$\chi \equiv \int \frac{dt}{a(t)} = \int_1^a \frac{da'}{a'^2 H(a')} = \int_0^z \frac{dz'}{H(z')}, \quad (1.19)$$

and we will mostly use it from now on even though it is worth to keep in mind that χ itself is not observable. It is related to the *physical distance* χ_{phys} measured by the light travel time between observers infinitesimally by the scale factor, $d\chi = ad\chi_{\text{phys}}$, so we get

$$\chi_{\text{phys}} \equiv \int_1^a \frac{da'}{a' H(a')} = \int_0^z \frac{dz'}{(1+z')H(z')}. \quad (1.20)$$

Another useful quantity is the distance inferred from the angular size of an object, the *angular diameter distance* (Hogg, 1999)

$$\chi_A \equiv \frac{\chi}{1+z}, \quad (1.21)$$

and the *luminosity distance* χ_L , which is defined in a way to preserve the Euclidian relation $F = L/(4\pi\chi_L^2)$ between observed flux F and intrinsic luminosity L . Since the flux drops off not only with distance, but also with an additional factor $(1+z)$ due to redshift, we get

$$\chi_L \equiv (1+z)\chi. \quad (1.22)$$

This is especially relevant for distance estimates using standardised candles with known intrinsic luminosity such as supernovae Ia (Astier et al., 2006).

We show the evolution of these different distance measures with redshift in Fig. 1.1. It is interesting to note that χ_A is not a monotonic function of a or z , therefore the angular diameter of an object with fixed physical size on the sky reaches a minimum with increasing physical distance before it starts growing again. This is a reflection of the non-trivial geometry of our universe. Another consequence is that only χ and χ_{phys} are additive, while χ_A and χ_L are not.

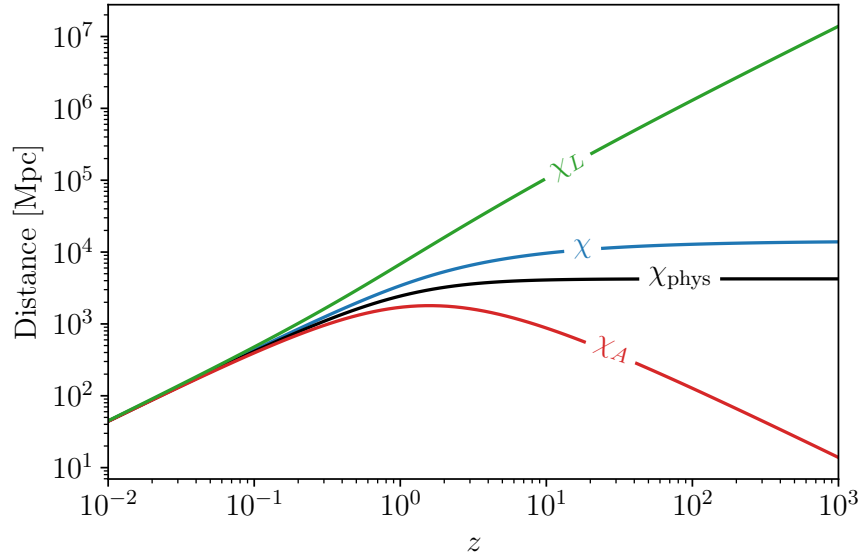


FIGURE 1.1: Evolution of the luminosity distance χ_L (green), the comoving distance χ (blue), the physical distance χ_{phys} (black) and the angular diameter distance χ_A (red) with redshift.

1.1.1 The cosmological constant problem

The cosmological constant term in Eq. 1.1 is of great interest since it currently dominates the effective energy budget of the universe. Historically, it was introduced by Einstein noting that the second Friedmann Eq. 1.8 without Λ requires $\ddot{a} \neq 0$ and prevents static solutions. This contradicted the state of astronomy at the time, and setting

$$\Lambda = 4\pi G(\rho + 3p) \quad (1.23)$$

fixes the dynamics to $\ddot{a} = 0$. Consequently, the cosmological constant can cause acceleration if it exceeds $4\pi G(\rho + 3p)$. However, Λ was mostly discarded after the discovery of the expansion of the Universe (Hubble, 1929), even though it always remained a possible addition to the field equations.

The situation is slightly complicated by a theorem of Lovelock, 1972, that proves under quite general assumptions that Λ is not a possible addition to the theory, but the *only* one. If the gravitational action can be written in terms of the metric $g_{\mu\nu}$ alone, coupled to some matter Lagrangian \mathcal{L}_m ,

$$S = \int dx^4 \sqrt{-g} (\mathcal{L}(g_{\mu\nu}) + \mathcal{L}_m) , \quad (1.24)$$

then the *unique* field equations of second order in four dimensions are given by

$$\alpha \left(R_{\mu\nu} - \frac{R}{2} g_{\mu\nu} \right) + \lambda g_{\mu\nu} = T_{\mu\nu} , \quad (1.25)$$

with the usual energy-momentum tensor $T_{\mu\nu} = \delta\mathcal{L}_m / \delta g_{\mu\nu} + g_{\mu\nu} \mathcal{L}_m$, and the equations of motion contain *two* coupling constants

$$\alpha \equiv \frac{1}{8\pi G} , \quad \lambda \equiv \frac{\Lambda}{8\pi G} , \quad (1.26)$$

where the units were chosen to match our notation in Eq. 1.1. General relativity is hence the unique theory of gravity in four dimensions with second-order equations of motion, and a cosmological constant term is a fundamental constituent. This implies that Λ should be considered as a constant of nature in the same way as the Newtonian constant G , and its absence, not its presence, would require explanation. Lovelock's theorem also has severe consequences for any modifications of gravity, and changing Einstein's theory is only possible in the following ways:

- Change the number of spacetime dimensions.
- Accept higher than second derivatives in the equations of motion. Note that in most cases, the resulting theory can dynamically decay to negative energy states and is therefore unstable (Ostrogradski, 1850; Woodard, 2007).
- Build the gravitational action from fields apart from the metric itself and therefore give up on the geometrical interpretation of gravity.
- Generate the equations of motion not from an action principle, but in some other way (e.g. emergent gravity by Verlinde, 2017).

It is also interesting to note that the cosmological constant is not a relativistic effect, as the same term is already present in Newtonian gravity. Starting from the Poisson equation for the potential ψ

$$\nabla^2 \psi = 4\pi G \rho, \quad (1.27)$$

we can find the corresponding Newtonian action

$$S = \int d^3\mathbf{x} \left(\frac{1}{2} (\nabla\psi)^2 + 4\pi G \rho \psi \right), \quad (1.28)$$

and it is perfectly allowed to add an additional scalar term

$$S = \int d^3\mathbf{x} \left(\frac{1}{2} (\nabla\psi)^2 + 4\pi G \rho \psi - \Lambda \psi \right). \quad (1.29)$$

Variation with respect to ψ yields the most general Newtonian equation of motion

$$\nabla^2 \psi = 4\pi G \rho - \Lambda, \quad (1.30)$$

which contains a cosmological constant term that can give rise to overall attractive or repulsive forces, so the vacuum is allowed to have gravitational interactions on its own even in Newtonian gravity. The term was not noticed because it is small and clearly not needed to describe planetary orbits.

Since our Universe is undergoing accelerated expansion (Riess et al., 1998; Perlmutter et al., 1999), in our Universe we have $\Lambda > 4\pi G(\rho + 3p)$ and as we can see in Tab. 1.1 it is the dominant component today.

This does raise the question: where is the problem? Why is a considerable amount of effort directed at discovering the nature of dark energy if we have a natural explanation in terms of the cosmological constant?

As it turns out, the problem is not the existence of Λ in GR, but its observed value. Today, $\Omega_\Lambda \approx 0.685$ (Planck Collaboration et al., 2016a). This corresponds to an energy scale

$$\rho_\Lambda = \Omega_\Lambda \rho_{\text{crit}} = \Omega_\Lambda \frac{3H_0^2}{8\pi G} \approx (3 \times 10^{-3} \text{ eV})^4, \quad (1.31)$$

in particle physics units. As mentioned before, formally we can also consider the cosmological constant as a contribution to the energy-momentum tensor by defining

$$T_{\mu\nu}^{\text{DE}} \equiv \frac{\Lambda}{8\pi G} g_{\mu\nu}, \quad (1.32)$$

and we call Λ dark energy (DE) when it is considered part of the energy-momentum tensor. As we have seen, $w_{\text{DE}} = -1$, so we get $\rho_{\text{DE}} = -p_{\text{DE}}$. Negative pressure seems like an exotic property, but as it turns out we have a good candidate for such behaviour. Consider the action for a scalar field ϕ with a potential $V(\phi)$

$$S = \int dx^4 \sqrt{-g} \left(\frac{1}{2} g_{\mu\nu} \partial^\mu \phi \partial^\nu \phi - V(\phi) \right), \quad (1.33)$$

from which we can derive the corresponding energy-momentum tensor

$$T_{\mu\nu} = \partial_\mu \phi \partial_\nu \phi - g_{\mu\nu} \left(\frac{1}{2} g^{\alpha\beta} \partial_\alpha \phi \partial_\beta \phi - V(\phi) \right), \quad (1.34)$$

and the symmetry assumptions of the FLRW metric imply that the field can depend on time only, $\phi(t)$. We then read off the effective density

$$\rho_\phi = -T_0^0 = \frac{1}{2} \dot{\phi}^2 + V(\phi), \quad (1.35)$$

and pressure

$$p_\phi \delta^i_j = T_j^i = \frac{1}{2} \dot{\phi}^2 - V(\phi). \quad (1.36)$$

The effective equation of state of such a field is therefore

$$w_\phi = \frac{\dot{\phi}^2/2 - V(\phi)}{\dot{\phi}^2/2 + V(\phi)}, \quad (1.37)$$

which can vary between 1 for $\dot{\phi} \gg V(\phi)$ and -1 for $V(\phi) \gg \dot{\phi}$. Dark energy thus behaves like a scalar field dominated by its potential energy, and in the stationary case of $\dot{\phi} = 0$ we recover exactly $w_\phi = -1$. This is the behaviour of a field resting at the minimum ϕ_0 of the potential, and there is no reason for $V(\phi_0)$ to vanish, so we expect effective contributions to dark energy from such fields. The problem is that we have discovered at least one scalar field of a similar type: the Higgs (Aad et al., 2015). We can estimate the resulting contribution at the potential minimum ϕ_0 as (Srednicki, 2007)

$$\rho_{\text{Higgs}} = V(\phi_0) \sim m_H^2 v^2 \sim (170 \text{ GeV})^4, \quad (1.38)$$

with the measured Higgs mass $m_H \approx 125 \text{ GeV}$ and vacuum expectation value $v \approx 246 \text{ GeV}$. This is clearly enormous compared to the measured value of ρ_Λ in Eq. 1.31.

However, the problem is even more severe. In quantum field theory (QFT), fields are constructed out of harmonic oscillators for each Fourier mode k . After quantisation, every field with mass m_i contributes a zero-point energy density for each mode (Weinberg, 1989)

$$\rho_{\text{vac}} \sim \sum_i \sigma_i \int_0^{k_{\text{max}}} \frac{4\pi k^2 dk}{(2\pi)^3} \frac{\sqrt{k^2 + m_i^2}}{2} \sim -\frac{k_{\text{max}}^4}{16\pi^2}. \quad (1.39)$$

The sum runs over all elemental particles in the standard model, with the sign varying depending on the spin,

$$\sigma_i \equiv \begin{cases} -1 & \text{for fermions} \\ +1 & \text{for bosons} \end{cases} \quad (1.40)$$

and we introduced a cut-off k_{\max} for the divergent integral. Even just calculating this integral up to scales where physics is well tested at accelerators, $k_{\max} \sim 100$ GeV, leads again to gigantic contributions. Note that there are more fermions than bosons in the standard model, so the net vacuum energy from ground states is large and negative.

We emphasize that the contributions in Eqs. 1.38 and 1.39 are quantities predicted by one of the most successful theories we have today, QFT. Their observed absence is therefore clearly a problem. There is one solution that works: suppose we get

$$\rho_{\text{Higgs}} + \rho_{\text{vac}} + \dots - \frac{\Lambda}{8\pi G} \approx (3 \times 10^{-3} \text{ eV})^4, \quad (1.41)$$

so the cosmological constant of general relativity *could* cancel all other terms to astonishing accuracy, while leaving a very small observed value. This conspiracy between quantum theory and GR is hard to believe, and no mechanism to enforce it has been found so far – and not for a lack of trying (see e.g. Weinberg, 1989 and Burgess, 2013 for excellent summaries of failed attempts). A common working assumption is to set the sum in Eq. 1.41 to zero, since it seems easier to imagine that any unknown mechanism could yield a perfect cancellation instead of leaving a small, observable net effect. We then have to find an independent mechanism to explain the accelerated expansion taking place in recent cosmic history.

1.1.2 Scalar fields as dark energy

As we have seen in the last section, there is indeed no shortage of ideas to cause accelerated expansion. The most straightforward way again relies on the scalar field ϕ defined by the action 1.33. At early times, such a field driving the accelerated expansion is called the *inflaton* (Starobinsky, 1980; Linde, 1982; Albrecht and Steinhardt, 1982), and at late times the *quintessence field* (Wetterich, 1988), but the underlying physics is the same. Usually one fixes a potential $V(\phi)$ and calculates the resulting cosmology, but a scalar field can actually give rise to any dynamic of the background expansion (Ratra and Peebles, 1988). To see this, we write the two Friedmann equations 1.7 and 1.8 for the energy density ρ_ϕ and pressure p_ϕ associated with the field ϕ

$$3H^2 = 8\pi G\rho_\phi = 8\pi G \left(\frac{1}{2}\dot{\phi}^2 + V(\phi) \right) \quad (1.42)$$

$$-2\dot{H} - 3H = 8\pi G p_\phi = 8\pi G \left(\frac{1}{2}\dot{\phi}^2 - V(\phi) \right), \quad (1.43)$$

and we assume a given expansion history $a(t)$. Adding Eqs. 1.42 and 1.43 yields

$$-2\dot{H} = 8\pi G\dot{\phi}^2, \quad (1.44)$$

and since $\dot{H} \leq 0$, we can solve for $\phi(t)$ by integrating

$$\phi(t) = \phi_{\text{ini}} \pm \int_{t_{\text{ini}}}^t dt' \sqrt{\frac{-\dot{H}(t')}{4\pi G}}. \quad (1.45)$$

The integrand in Eq. 1.45 is monotonic, so we can invert the function to get $t(\phi)$. Subtracting Eqs. 1.42 and 1.43 leads to the potential

$$\begin{aligned} V(\phi) &= \frac{1}{8\pi G} \left[\dot{H}(t) + 3H(t) \right] \\ &= \frac{1}{8\pi G} \left[\dot{H}(t(\phi)) + 3H(t(\phi)) \right], \end{aligned} \quad (1.46)$$

which can support any expansion history specified by $H(t)$. We assumed for simplicity that the energy budget is given by ϕ alone, but other contributions ρ_i and p_i can be added in the Friedmann equations and the construction proceeds in the same way.

It is therefore not difficult to come up with additional scalar fields that drive the accelerated expansion, but the problem of scale remains. By taking a time derivative of Eq. 1.42 and substituting the second Friedmann Eq. 1.43, we can also derive the Klein-Gordon equation for a scalar field in an expanding background

$$\ddot{\phi} + 3H\dot{\phi} - \frac{\partial}{\partial\phi}V(\phi) = 0, \quad (1.47)$$

where H plays the role of a damping term. If the field is supposed to resemble a cosmological constant as measurements suggest, we need the damping to be dominant, $H \sim \sqrt{\partial^2 V / \partial\phi^2}$, in order to keep the field static leading to an equation of state $w_\phi \approx -1$ from Eq. 1.37. But this is the associated mass scale of the field, thus

$$m_\phi = \sqrt{\frac{\partial^2 V(\phi)}{\partial\phi^2}} \sim H_0 \sim 10^{-33} \text{ eV}, \quad (1.48)$$

which is tiny. Note that the number appears here due to a circular argument: H_0 is responsible for setting the small energy scale associated with the effective Λ and the accelerated expansion today in Eq. 1.31 that seems to be in need of explanation. However, by demanding that the field is damped by the current expansion and behaves like a cosmological constant, we find that the mass scale has to be of order of the measured Hubble parameter. The problem is also apparent in the reconstructed potential in Eq. 1.46 – we can get any expansion history at the price of inserting H by hand, but then we might as well set the value of Λ to whatever is observed in the first place without introducing additional quantities.

So we made no progress in understanding *how* this scale arises from some fundamental process. If the scalar field also couples to other matter, the small mass translates to an attractive interaction with range of the Hubble distance $\sim H_0^{-1}$ (Carroll, 2001) that has not been detected. Scalar fields therefore provide a phenomenological framework to model the expansion history, but so far fail to explain it.

The discussion applies to the epoch of inflation as well, but the Hubble rate H_{inf} at early times is of order of the Planck scale, $m_\phi \sim H_{\text{inf}} \sim M_{\text{Pl}}$, and we have seen from the discussion in Sec. 1.1.1 that very large scales more easily arise from fundamental theory in particle physics, so the problem is less severe.

The third alternative, apart from a cosmological constant or scalar fields as drivers for the accelerated expansion, is modifying general relativity itself. We will return to this possibility in Chapter 3 and discuss a possible theory and its phenomenology in detail.

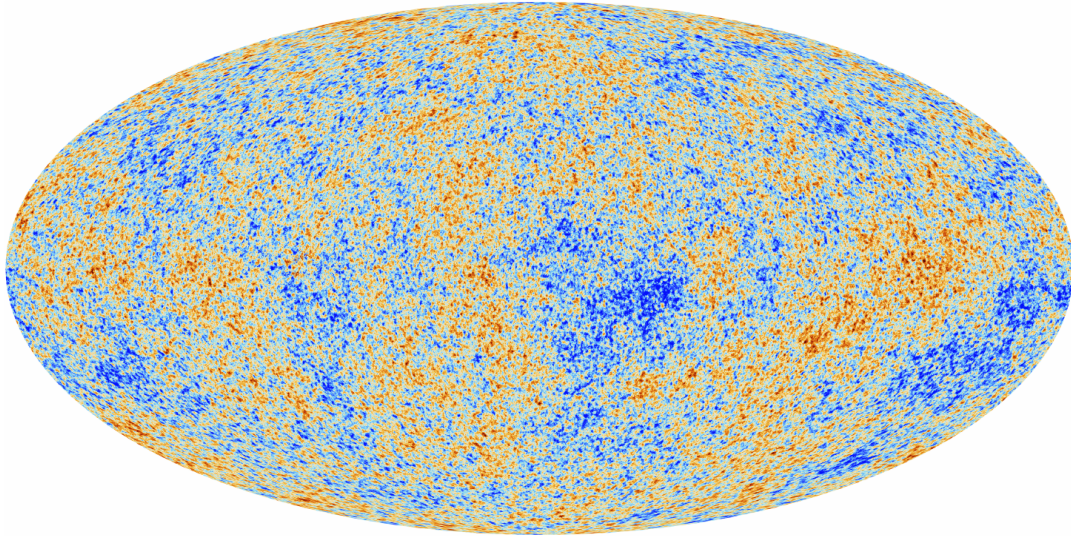


FIGURE 1.2: The temperature of the cosmic microwave background (CMB) as seen by the PLANCK satellite. The fluctuations shown here are of order $\Delta T/T \sim 10^{-5}$ and almost perfectly Gaussian. They form the initial seeds for all structures in the Universe today. Copyright: ESA, Planck collaboration

1.2 The cosmic density field

The Universe we observe clearly shows deviations from perfect homogeneity and isotropy, both assumptions only hold on average. The structures we find today are a consequence of the primordial density fluctuations $\Delta T/T \simeq 10^{-5}$ that we measure in the cosmic microwave background shown in Fig. 1.2. Since the initial deviations from the mean density are small, we define the density contrast δ as

$$\delta(\mathbf{x}) \equiv \frac{\rho(\mathbf{x}) - \bar{\rho}}{\bar{\rho}}, \quad (1.49)$$

by subtracting the average density $\bar{\rho}$. It is the main quantity of interest for understanding the growth of structures.

1.2.1 Gaussian random fields

The anisotropy in the CMB follows a Gaussian distribution to remarkable accuracy (Planck Collaboration et al., 2016b), and consequently we will adopt this statistical model for the density contrast. The probability to find the amplitudes $\delta(\mathbf{x}_1)$ and $\delta(\mathbf{x}_2)$ at two points \mathbf{x}_1 and \mathbf{x}_2 in space is therefore given by a bivariate Gaussian distribution

$$p(\delta(\mathbf{x}_1), \delta(\mathbf{x}_2)) = \frac{1}{\sqrt{(2\pi)^2 \det(C)}} \exp\left(-\frac{1}{2} \begin{pmatrix} \delta(\mathbf{x}_1) \\ \delta(\mathbf{x}_2) \end{pmatrix}^T C^{-1} \begin{pmatrix} \delta(\mathbf{x}_1) \\ \delta(\mathbf{x}_2) \end{pmatrix}\right), \quad (1.50)$$

with the covariance matrix

$$C = \begin{pmatrix} \langle \delta^2(\mathbf{x}_1) \rangle & \langle \delta(\mathbf{x}_1)\delta(\mathbf{x}_2) \rangle \\ \langle \delta(\mathbf{x}_2)\delta(\mathbf{x}_1) \rangle & \langle \delta^2(\mathbf{x}_2) \rangle \end{pmatrix}. \quad (1.51)$$

The mean $\langle \dots \rangle$ here indicates an average over an hypothetical *ensemble* of universes, which is clearly not observable. We will comment on this issue in Sec. 1.2.2. The off-diagonal elements of the covariance define the correlation function

$$\zeta(\mathbf{x}_1, \mathbf{x}_2) \equiv \langle \delta(\mathbf{x}_1) \delta(\mathbf{x}_2) \rangle, \quad (1.52)$$

between the two points. It describes how fast the field loses memory of its value at \mathbf{x}_1 with increasing distance $\mathbf{r} = |\mathbf{x}_2 - \mathbf{x}_1|$ and hence sets a typical scale for structures. Note that the Cauchy-Schwarz inequality

$$\langle \delta(\mathbf{x}_2) \delta(\mathbf{x}_1) \rangle^2 \leq \langle \delta^2(\mathbf{x}_1) \delta^2(\mathbf{x}_2) \rangle, \quad (1.53)$$

guarantees that the covariance C is positive definite. Statistical homogeneity ensures that the correlation function can only depend on the relative distance \mathbf{r} between points and the variance has to be the same everywhere, $\langle \delta^2(\mathbf{x}_1) \rangle = \langle \delta^2(\mathbf{x}_2) \rangle$. In addition, isotropy implies that the correlation has to be independent of the direction and can only depend on the magnitude of the separation r .

For purely Gaussian density fields, dealing with the variance is sufficient, since the mean is zero by construction and all even higher moments are related $\langle \delta^{2n} \rangle \propto \langle \delta^2 \rangle^n$, while odd moments $\langle \delta^{2n+1} \rangle \propto \langle \delta \rangle$ vanish. This is a consequence of Wick's theorem (Srednicki, 2007).

Homogeneous fields have independent modes in Fourier space. To see this, we transform the density field

$$\delta(\mathbf{k}) = \int d^3\mathbf{x} \delta(\mathbf{x}) e^{-i\mathbf{k}\cdot\mathbf{x}}. \quad (1.54)$$

and calculate the variance between two modes \mathbf{k}_1 and \mathbf{k}_2 , which yields

$$\langle \delta(\mathbf{k}_1) \delta^*(\mathbf{k}_2) \rangle \equiv (2\pi)^3 \delta_D(\mathbf{k}_1 - \mathbf{k}_2) P(k), \quad (1.55)$$

with the power spectrum $P(k)$, and the Dirac distribution δ_D ensures that the Fourier modes decouple. The covariance 1.51 then becomes diagonal in Fourier space, and the probability to find the joint amplitudes for modes \mathbf{k}_1 and \mathbf{k}_2 separates into

$$p(\delta(\mathbf{k}_1, \mathbf{k}_2)) = p(\delta(\mathbf{k}_1)) p(\delta(\mathbf{k}_2)). \quad (1.56)$$

Note that, because the correlation function is dimensionless, the power spectrum has the dimension of a volume. From the Fourier transform of $\delta(\mathbf{x})$, we find the relation between the correlation function $\zeta(r)$ and the power spectrum $P(k)$:

$$\begin{aligned} \zeta(r) &= \int \frac{d^3\mathbf{k}_1}{(2\pi)^3} \int \frac{d^3\mathbf{k}_2}{(2\pi)^3} \langle \delta(\mathbf{k}_1) \delta^*(\mathbf{k}_2) \rangle e^{-i\mathbf{k}_1\cdot\mathbf{x}_1} e^{i\mathbf{k}_2\cdot\mathbf{x}_2} \\ &= 2\pi \int \frac{k^2 dk}{(2\pi)^3} P(k) \int \sin \varphi d\varphi e^{ikr \cos \varphi} \\ &= 4\pi \int \frac{k^2 dk}{(2\pi)^3} P(k) j_0(kr), \end{aligned} \quad (1.57)$$

with the spherical Bessel function of the first kind, $j_0(x) = \sin(x)/x$, and we switched to spherical coordinates and introduced the angle φ between the two vectors $\mathbf{k} = \mathbf{k}_2 - \mathbf{k}_1$ and $\mathbf{r} = \mathbf{x}_2 - \mathbf{x}_1$ to perform the integration. The variance of the field can be

recovered by setting $r = 0$,

$$\zeta(0) = \langle \delta^2 \rangle = \sigma^2 = 4\pi \int \frac{k^2 dk}{(2\pi)^3} P(k), \quad (1.58)$$

which suggests to define the dimensionless quantity

$$\Delta^2(k) \equiv k^3 P(k) = \frac{d \ln k}{dk} \sigma^2, \quad (1.59)$$

measuring the relative fluctuations per logarithmic interval in k . We still have to fix the amplitude of the fluctuations, and this is commonly done by specifying the variance at one specific scale. To do so, we introduce the smoothed density contrast

$$\delta_R(\mathbf{x}) = \int d^3 \mathbf{y} \delta(\mathbf{x}) W_R(|\mathbf{x} - \mathbf{y}|), \quad (1.60)$$

with the top-hat filter of width R . This convolution turns into a product in Fourier space, so the smoothed variance is given by:

$$\sigma_R^2 = 4\pi \int \frac{k^2 dk}{(2\pi)^3} P(k) W_R^2(k). \quad (1.61)$$

By convention the variance of density fluctuations is then measured at a scale of $R = 8 h^{-1}$ Mpc, which makes the amplitude of the power spectrum proportional to σ_8^2 .

1.2.2 Ergodic principle and cosmic variance

In the last section, we introduced averages $\langle \dots \rangle$ over the density contrast δ , which is thought of as the outcome of a Gaussian random process. However, there is only one Universe, so instead of calculating the mean over an ensemble of realisations of the field, we average over causally disconnected volumes of space. The assumption that both prescriptions are equivalent is the *ergodic principle* in cosmology.

As we will see, there are fundamental limits to this approach since there is only a limited number of uncorrelated patches for every scale. If we want to determine the statistical properties of any quantity γ , it has to be expanded in spherical harmonics on the sky:

$$\gamma(\hat{\mathbf{n}}) = \sum_{\ell m} a_{\ell m} Y_{\ell m}(\hat{\mathbf{n}}), \quad (1.62)$$

and statistical isotropy again prevents any preferred direction and therefore angular dependence. Hence all information about the variance is encoded in the coefficients

$$\langle a_{\ell m} a_{\ell' m'}^* \rangle \equiv C_\ell \delta_{\ell \ell'} \delta_{m m'}. \quad (1.63)$$

With this expression, we get the general two-point function

$$\langle \gamma(\hat{\mathbf{n}}) \gamma^*(\hat{\mathbf{n}}') \rangle = \sum_{\ell m} C_\ell Y_{\ell m}(\hat{\mathbf{n}}) Y_{\ell m}^*(\hat{\mathbf{n}}') = \sum_{\ell} C_\ell \left(\frac{2\ell + 1}{4\pi} \right) P_\ell(\hat{\mathbf{n}} \cdot \hat{\mathbf{n}}'), \quad (1.64)$$

and by using the orthogonality of the Legendre polynomials P_ℓ , we can invert eq. 1.64 to get:

$$C_\ell = \frac{1}{4\pi} \int d^2 \hat{\mathbf{n}} \int d^2 \hat{\mathbf{n}}' P_\ell(\hat{\mathbf{n}} \cdot \hat{\mathbf{n}}') \langle \gamma(\hat{\mathbf{n}}) \gamma^*(\hat{\mathbf{n}}') \rangle. \quad (1.65)$$

However, we can see the sky from only one position. What is actually observed is an average over m for each fixed ℓ

$$C_\ell^{\text{obs}} = \frac{1}{2\ell+1} \sum_m a_{\ell m} a_{\ell m}^* = \frac{1}{4\pi} \int d^2\hat{\mathbf{n}} \int d^2\hat{\mathbf{n}}' P_\ell(\hat{\mathbf{n}} \cdot \hat{\mathbf{n}}') \gamma(\hat{\mathbf{n}}) \gamma^*(\hat{\mathbf{n}}'), \quad (1.66)$$

and the mean square difference between Eqs. 1.65 and 1.66 is then given by (Weinberg, 2008)

$$\left\langle \left(\frac{C_\ell - C_\ell^{\text{obs}}}{C_\ell} \right)^2 \right\rangle = 1 - 2 + \frac{1}{(2\ell+1)^2 C_\ell^2} \sum_{mm'} \langle a_{\ell m} a_{\ell m}^* a_{\ell m'} a_{\ell m'}^* \rangle. \quad (1.67)$$

If the individual coefficients $a_{\ell m}$ follow a Gaussian distribution, we can apply the Wick theorem to express the correlator as a product of two-point functions. Thus we arrive at the final result

$$\left\langle \left(\frac{C_\ell - C_\ell^{\text{obs}}}{C_\ell} \right)^2 \right\rangle = \frac{2}{2\ell+1} C_\ell. \quad (1.68)$$

The consequence is that there is an irreducible noise given by the fact that there is only one realisation of the sky to observe. This is known as the *cosmic variance* limit. If we observe only a fraction of the sky f_{sky} , for example because our telescope has a limited field of view, the variance is further enhanced by a factor $1/f_{\text{sky}}$.

1.2.3 Linear growth of structures

The evolution of structures can be understood in terms of the dynamics of fluids under the influence of their own gravity. We will discuss a proper relativistic treatment in Sec. 3.3, but for now let us assume a fluid with density ρ and velocity \mathbf{v} , evolving according to the continuity equation

$$\dot{\rho} - \nabla(\rho\mathbf{v}) = 0, \quad (1.69)$$

the Euler equation, which expresses momentum conservation in presence of forces from gravity and pressure gradients ∇p

$$\dot{\mathbf{v}} + (\mathbf{v}\nabla)\mathbf{v} = -\frac{1}{\rho}\nabla p - \nabla\psi, \quad (1.70)$$

and the Poisson equation for the Newtonian potential ψ .

$$\nabla^2\psi = 4\pi G\rho. \quad (1.71)$$

The fluid equations are non-linear and notoriously difficult to solve in general. Therefore we linearise the set of equations for small perturbations δ , $\mathbf{v} \ll 1$, δp and $\delta\psi$, and transform to comoving coordinates $\mathbf{x} \rightarrow \mathbf{x}/a$, to find the linearised continuity equation (Bernardeau et al., 2002)

$$\delta = -\frac{1}{a}\nabla\mathbf{v}, \quad (1.72)$$

and taking into account that the velocity transforms as $\mathbf{v} \rightarrow \mathbf{v} + H\mathbf{x}$ due to the contribution from the Hubble flow, we find the linearised Euler equation

$$\dot{\mathbf{v}} + H\mathbf{v} = -\frac{1}{a\bar{\rho}}\nabla\delta p - \frac{1}{a}\nabla\psi. \quad (1.73)$$

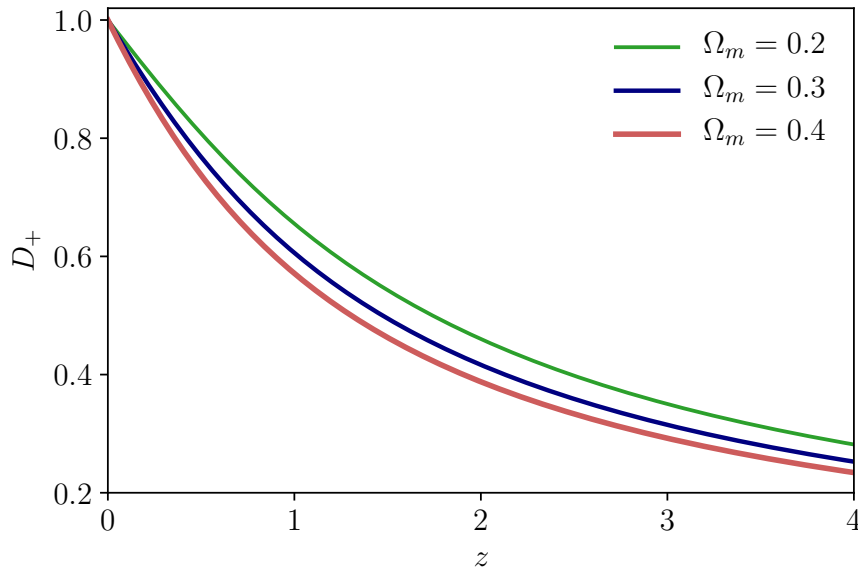


FIGURE 1.3: Numerical solutions $D_+(z)$ of the growth equation for different values of the matter density parameter Ω_m . Universes with higher matter content experience faster structure growth.

The Poisson equation is already linear in the potential, but in comoving coordinates it reads

$$\nabla^2 \psi = 4\pi G a^2 \bar{\rho} \delta. \quad (1.74)$$

Taking the time derivative of Eq. 1.72 and plugging in the divergence of Eq. 1.73, we arrive at the *linear growth equation*

$$\ddot{\delta} + 2H\dot{\delta} - \frac{w}{a^2} \nabla^2 \delta = 4\pi G \bar{\rho} \delta, \quad (1.75)$$

with the equation of state $w = \delta p / \delta \rho$. The solution gives the linear evolution of density perturbations, and we note that the last term on the left hand side vanishes for matter on cosmological scales since $w_m \approx 0$. The growing solution of Eq. 1.75 is called the *growth function* $D_+(a)$, and the linear density contrast evolves according to

$$\delta(a) = D_+(a) \delta_0, \quad (1.76)$$

where it is common to set $D_+(1) = 1$. The evolution of structures given by Eq. 1.75 depends on cosmology via the background evolution H and the source term $\bar{\rho} = \Omega_m \rho_{\text{crit}}$, so measuring the growth rate is an excellent method to constrain cosmological parameters. In Fig. 1.3 we show D_+ calculated for universes with various matter density parameters Ω_m and find as expected that structures grow faster in an universe with higher matter density due to the source term $\propto \bar{\rho} = \Omega_m \rho_{\text{crit}}$ in Eq. 1.75. By assuming a universe dominated by a single component and an ansatz $\delta \propto t^a$, one can easily derive the edge cases

$$\delta \propto \begin{cases} \ln a & \text{for } \Omega_\gamma = 1 \\ a & \text{for } \Omega_m = 1 \\ \text{const.} & \text{for } \Omega_\Lambda = 1 \end{cases}, \quad (1.77)$$

where we always chose the growing solution. Thus growth of structures proceeds only very slowly during the early universe and stops once Ω_Λ becomes dominant. For universes with several components, we have to rely on numerical solutions.

1.3 The non-linear Universe

The density contrast of structures today ranges from $\delta \approx 10^6$ for galaxies, to $\delta \approx 200$ for clusters, so clearly the linear approximations made in Sec. 1.2.3 break down. The amplitude of the density fluctuations δ is bounded from below $\delta > -1$ by construction, but not from above. As structures form and the amplitude of overdensities grows, the field therefore becomes skewed and develops non-Gaussian features. Then the information about the field is not contained in the variance (or equivalently the power spectrum) any more, and other statistical descriptions have to be employed, such as general N -point correlators and polyspectra (Bernardeau et al., 2002) or Minkowski functionals (Schmalzing, Kerscher, and Buchert, 1995; Hikage, Komatsu, and Matsubara, 2006).

The main cause for the breakdown of perturbation theory is that once overdensities form at a position, the gravitational pull in the vicinity increases and changes the local growth rate. Thus the growth function picks up a position dependence

$$\delta(\mathbf{x}, a) = D_+(a, \mathbf{x})\delta(\mathbf{x}), \quad (1.78)$$

and in Fourier space the product turns into a convolution, coupling different k -modes. Approaches that rely on a hierarchy of scales to separate them therefore fail, and the evolution has to be solved collectively. Despite considerable efforts (Bernardeau et al., 2002; Carrasco, Hertzberg, and Senatore, 2012), so far no analytic method to deal with this problem in generality has been found.

The large-scale structure today is mostly formed by dark matter halos, long lived semi-stable systems formed by gravitational collapse. Initially, they consist out of approximately spherical high peaks in the initial density field. The Birkhoff theorem guarantees that their evolution decouples from the background, and only depends on the matter inside the enclosed sphere. The proto-halos then evolve approximately as closed universes with $\Omega_m \approx 1$. The radial extend $r(t)$ of the system is given by (Weinberg, 2008)

$$\ddot{r} = -\frac{GM}{r^2}, \quad (1.79)$$

where M is the total enclosed mass. The equation is solved by

$$r = A(1 - \cos \theta) \quad (1.80)$$

$$t = B(\theta - \sin \theta), \quad (1.81)$$

with $A^3 = GMB^2$ and a phase θ to describe the state of collapse. The proto-halo initially co-expands with the background, reaches a maximum extend at the turnaround time $\theta = \pi$, $t_{\text{tr}} = B\pi$ and subsequently collapses to a point at $\theta = 2\pi$. In a real system, the evolution does not go quite as far: as the gravitational binding energy released by the collapse is converted to kinetic energy of the particles that form the halo, the system eventually reaches virial equilibrium.

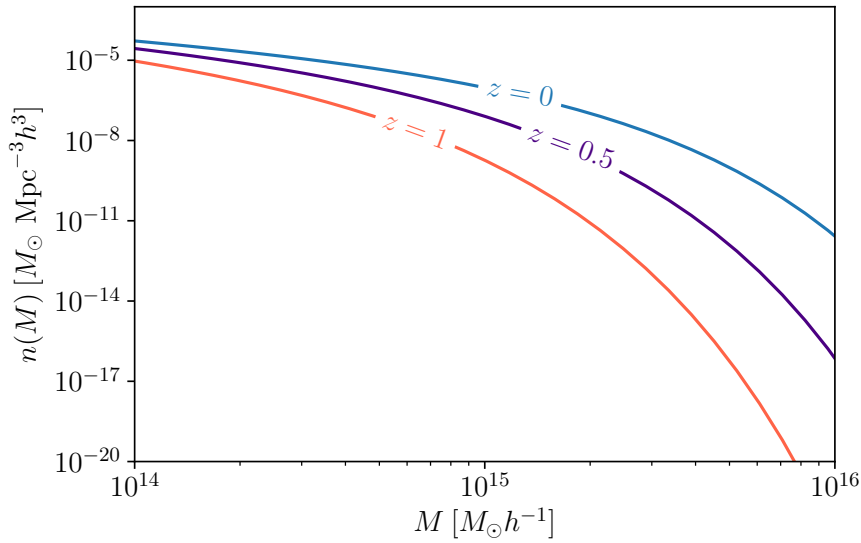


FIGURE 1.4: Press-Schechter mass function according to Eq. 1.86 for $z = 0$ (blue), $z = 0.5$ (purple) and $z = 1$ (red). The abundance of massive halos is an extremely sensitive probe of structure growth.

A very important parameter is the extrapolated *linear* density contrast to the end point of collapse, which yields the *critical collapse threshold*

$$\delta_c \equiv \delta(2t_{\text{tr}}) = \frac{3}{5} \left(\frac{3\pi}{4} \right)^{2/3} \approx 1.69, \quad (1.82)$$

for an $\Omega_m = 1$ universe, and it mildly depends on the background cosmology. The idea is that once linear theory predicts that the smoothed density field δ_R exceeds the threshold δ_c , the corresponding patch has collapsed to a halo with associated mass $M = 4\pi/3\Omega_m\rho_{\text{crit}}R^3$. The abundance of halos is therefore connected to the cumulative probability distribution of δ (Bardeen et al., 1986)

$$P_\delta(R) = \int_{\delta_c}^{\infty} d\delta_R p(\delta_R) \quad (1.83)$$

$$= \frac{1}{2} \text{erfc} \left(\frac{\delta_c}{\sqrt{2}\sigma_R} \right), \quad (1.84)$$

and we solved the integral by using that $p(\delta_R)$ is given by Eq. 1.50 for a Gaussian field

$$p(\delta_R) = \frac{1}{\sqrt{2\pi\sigma_R^2}} \exp \left(-\frac{\delta_R^2}{2\sigma_R^2} \right). \quad (1.85)$$

The number of halos per mass interval is then calculated by taking the derivative with respect to M

$$n(M) = \frac{\partial P}{\partial M} = \sqrt{\frac{2}{\pi}} \frac{\delta_c}{\sigma} \frac{d \ln \sigma_R}{dM} \exp \left(-\frac{\delta_c^2}{2\sigma_R^2} \right), \quad (1.86)$$

which is the mass function derived by Press and Schechter, 1974. We fixed the normalisation by hand since integrating over all mass M in the density field only gives back 1/2. We will return to the reason for this problem and more sophisticated mass function models in the context of a general theory of random walks of Gaussian fields

in Chapter 4.

For now, we note that while the result in Eq. 1.86 is not very accurate when compared to N -body simulations, it can give valuable insights that apply in general. The abundance of massive halos depends exponentially on δ_c^2/σ_R^2 , and from Eq. 1.76 we get $\sigma_R^2(z) \propto D_+^2(z)$. The number of halos is therefore an extremely sensitive probe of structure growth as shown in Fig. 1.4 and consequently of cosmological parameters. Massive dark matter halos are hosts of galaxy clusters, even though matching observed clusters and the suspected underlying dark matter halo is not easy. We will deal with this problem and the potential of cluster abundance to yield precise constraints on cosmology in Chap. 2.

The collapse criterion is stated in terms of the variance σ^2 of the field, which has to be calculated from the matter power spectrum for each individual cosmology. But as soon as the condition is met, the evolution of the spherical collapsing patch proceeds independent of the background Universe. Birkhoff's theorem therefore suggests that the mass function should be *universal*, i.e. independent of cosmological parameters, when written as a function of σ^2 . Real collapse however does not quite fulfil the necessary symmetry assumptions. The discussion about universality is still ongoing. Simulations suggest that it does not quite hold (Tinker et al., 2008) at least for fixed overdensity definitions to identify halos, but it appears to be possible to recover a universal behaviour independent of cosmology with the right definition of halos, and if the mass function is expressed in terms of the relative peak height $\nu \equiv \delta_c^2/\sigma^2$ (Sheth and Tormen, 1999; Despali et al., 2015).

Even though we assumed linear dynamics and Gaussian statistics in the derivation of the mass function, we emphasize that the result contains the full non-linear dynamic of the density field via the threshold δ_c . Linear dynamics are reversible, so we can consider the variance σ_R^2 as an initial fixed quantity that captures the state of the density field at early times when it is still Gaussian and calculate corrections to δ_c . We will return to this point in detail when calculating the mass function for non-standard cosmologies in Chapter 4. The halo abundance is thus a non-perturbative probe of δ and includes information beyond what is captured by other statistical quantities such as the power spectrum $P(k)$.

If we try to understand the non-linear evolution of the density field, in most cases we are not lucky enough to have analytical tools available as described above. For many applications we therefore have to rely on N -body simulations to solve the evolution given by the combination of fluid equations (Eqs. 1.69 and 1.70) and gravity (Eq. 1.71). Often the approaches are complementary, and precise semi-analytical mass functions can be found by measuring the effective collapse barrier in simulations (Sheth and Tormen, 1999).

1.4 Outline of this work

After this brief overview of the current state and open problems of cosmology, we will turn towards clusters of galaxies in a more realistic setting. In Chapter 2 we discuss the measured cluster abundance detected by the Planck satellite (Planck Collaboration et al., 2015) and their implications for cosmology. The difficulty to connect the observed cluster with the dark matter halo mentioned above, or equivalently the task to infer the total cluster mass, is crucial in the interpretation of the results. We will therefore spend some time to discuss the consequences of our current limited knowledge about cluster physics. We will then extend the framework used to model the Planck cluster abundance to CORE, a future CMB satellite mission recently proposed to ESA. Our

cosmological forecasts (CORE Collaboration et al., 2018a) indicate that the detected cluster sample would lead to precise constraints on Λ CDM parameters and yields complementary information to the primary CMB.

In Chapter 3 we discuss approaches to detect deviations from standard cosmology without assuming a specific model. We focus on a parametrisation to describe the growth of structures in the late universe, and extend it to a fully relativistic framework valid at all times. We implement the modified Einstein equations in CLASS (Blas, Lesgourgues, and Tram, 2011), and numerically calculate the perturbations in parametrised effective models. We also consider an example of modified gravity, $f(R)$ gravity, and show how the evolution of linear perturbations can be mapped onto the parametrised framework. This allows us to use the modified CLASS code to evaluate cosmological quantities in $f(R)$ cosmologies.

Then we return to galaxy clusters in order to constrain deviations from GR in the non-linear regime. In order to do so, in Chapter 4 we develop a halo mass function for $f(R)$ gravity. We work within a spherical collapse framework, and use a suite of N -body simulations to calibrate and test our model. We find that current constraints on modified gravity from the abundance of galaxy clusters suffer from a degeneracy with the currently ill-constrained neutrino mass, so we include them into our spherical collapse framework. This allows us to calculate halo number counts in $f(R)$ cosmologies with massive neutrinos, and we discuss the resulting degeneracy in the context of forecasts for future cluster surveys. Modified gravity can also influence the dynamics within a cluster, and therefore changes the mapping between observables and halo mass. We discuss a simplified model based on the change in the virial theorem to account for this effect.

We conclude and summarise the overall results in Chapter 5 and give an overview over several ongoing projects connected to the work presented here.

Chapter 2

Cosmology with Sunyaev-Zel'dovich cluster surveys – from Planck to CORE

As we have discussed in the previous chapter, clusters of galaxies are a powerful cosmological probe since their abundance depends exponentially on the variance of the density field. However, to fully utilise them, we have to find a way to connect the observed cluster with the underlying halo. In this chapter, we present constraints obtained from a sample detected by the Sunyaev Zel'dovich (SZ) effect by the Planck satellite. We start by a brief introduction to the underlying physics in Sec. 2.1, before we discuss the Planck cluster catalogue and the theoretical modelling of the expected cluster number counts in Sec. 2.2 and the connection between SZ observables and the underlying dark matter halo mass. We then turn to the likelihood function necessary to extract information about the cosmological model parameters out of the observed abundance. As large surveys resolve more and more clusters, we show that it becomes necessary to include the response of the cluster abundance to the large-scale structure in which they are embedded. This has implications for the likelihood function and for the derived cosmological parameters.

From there, we extend the cluster abundance model to forecasts for CORE, a planned CMB satellite successor to Planck in Sec. 2.3. The results presented there have been obtained in collaboration with Jean-Baptiste Melin and Anna Bonaldi, who provided the simulated CORE noise maps needed to calculate the expected cluster detections. Parts of the work have been published in CORE Collaboration et al., 2018a.

2.1 The Sunyaev Zel'dovich effect

While the CMB is the source of our best knowledge about the early universe, it also contains a wealth of information about the late-time evolution. On their way to us, the geodesics of primordial photons are disturbed by interactions with the intermediate large-scale structure. Since the density of the universe is very low, the major part of this influence is only gravitational: spatially varying potentials give rise to CMB lensing (for a review see e.g. Lewis and Challinor, 2006), while time-varying potentials change the temperature of the radiation via the integrated Sachs-Wolfe effect (Sachs and Wolfe, 1967).

If the CMB photons travel through a relatively dense environment however, such as the hot, ionised gas of a galaxy cluster, they will also undergo Compton scattering with the thermal electrons of the intra-cluster medium. This interaction leads to a typical energy boost of order $k_B T_e / m_e c^2$ from electrons of temperature T_e . The cold, thermal bath of the CMB is therefore coupled to the hot reservoir of the galaxy cluster.

The optical depth of clusters is small, so scattering is still a rare process. Consequently the relaxation time exceeds the Hubble time, and we can detect the deviation of the CMB from equilibrium. The additional energy input distorts the typical blackbody spectrum, leading to a temperature change

$$\frac{\Delta T}{T_{\text{CMB}}} = f(x) \int n_e \frac{k_B T_e}{m_e c^2} \sigma_T d\chi \equiv f(x)y, \quad (2.1)$$

with the Thomson cross-section σ_T , the electron density n_e and the dimensionless frequency $x \equiv hv/k_B T_{\text{CMB}}$ integrated along the line of sight χ . The amplitude is absorbed into the Compton y -parameter, while the spectral dependence is given by

$$f(x) = \left(x \frac{e^x + 1}{e^x - 1} - 4 \right) \left(1 + \delta_{\text{rel}}(x, T_e) \right) \quad (2.2)$$

where $\delta_{\text{rel}} \ll 1$ is a relativistic correction factor (Carlstrom, Holder, and Reese, 2002). The frequency signature is quite unique with a zero-crossing at $x \approx 3.83$ corresponding to ≈ 217 GHz, as shown on the right side of Fig. 2.1. Low-energy photons below this threshold are scattered to higher frequencies, creating a characteristic feature that cannot easily be mimicked by other effects.

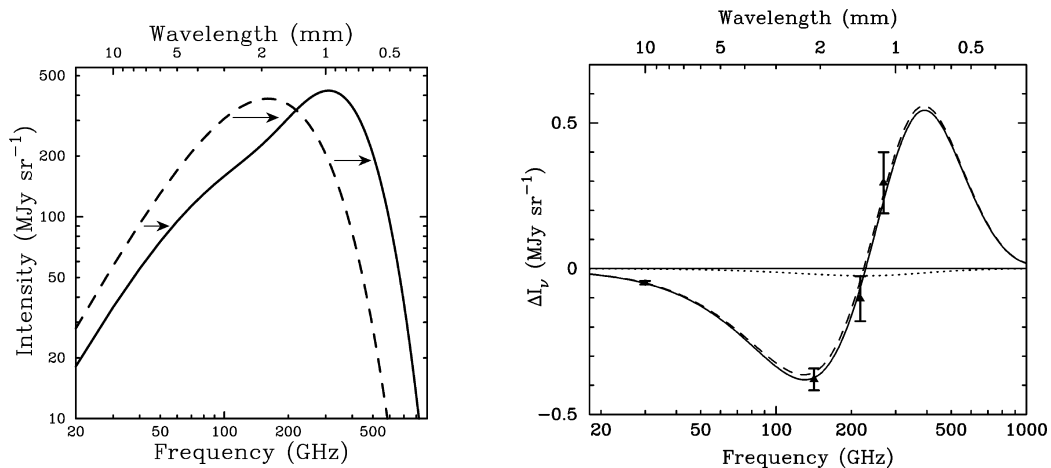


FIGURE 2.1: **Left:** CMB blackbody spectrum (dashed) distorted by the thermal SZ effect (solid). The curves cross for a frequency of ≈ 217 GHz, photons below this threshold are scattered to higher energies, leading to an intensity gain for higher frequencies (and subsequent intensity decrease below). The effect is strongly exaggerated. **Right:** Measured spectrum of Abell 2163 showing the characteristic dip below and peak above 217 GHz. Both plots from Carlstrom, Holder, and Reese, 2002.

Note that the signal in Eq. 2.1 itself is independent of redshift. But since a cluster is detected through the integrated Compton y -parameter over its angular size on the sky

$$\int \Delta T d\Omega \propto \frac{1}{\chi_A^2(z)}, \quad (2.3)$$

the detection depends on the angular diameter distance χ_A . However the evolution of χ_A becomes quite flat for large z , so it is possible to find clusters at high redshifts with SZ surveys. The matter density increases with $(1+z)^3$, thus a cluster of a given mass will be denser and subsequently hotter at earlier times – giving rise to a higher

signal. So in principle, SZ surveys can detect all clusters above a threshold mass almost independent of distance. Instrumental noise can slightly complicate this picture, introducing an additional z -dependence for SZ selection functions as will be discussed in Sec. 2.2.1.

For a virial system, some simple scaling relations can be very insightful. The total potential energy of the cluster is proportional to

$$\langle E_{\text{pot}} \rangle \propto -\frac{GM^2}{R}, \quad (2.4)$$

and with $R \propto M^{1/3}$, we get $\langle E_{\text{pot}} \rangle \propto M^{5/3}$. The kinetic energy scales with the temperature and the number of particles $\langle E_{\text{kin}} \rangle \propto NT \propto MT$, and the virial theorem requires $2\langle E_{\text{kin}} \rangle = -\langle E_{\text{pot}} \rangle$. Therefore

$$\langle T \rangle M \propto \langle E_{\text{pot}} \rangle \propto M^{5/3} \Rightarrow \langle T \rangle \propto M^{2/3}, \quad (2.5)$$

and consequently, the Compton y -parameter scales as

$$y \propto \int n_e T_e dl \propto M \langle T_e \rangle \propto M^{5/3} \propto \langle E_{\text{pot}} \rangle, \quad (2.6)$$

and is hence a direct probe of the gravitational potential.

In Fig. 2.2 we show a composite image of the Shapley supercluster imaged in the optical, X-ray or via the SZ effect. The much wider extent of the SZ emission probing the projected electron density becomes apparent compared to the peaked X-ray signal $\propto \rho^2$, which allows Planck to trace the full extend of the structure.

2.2 The Planck cluster sample

Currently, the largest SZ selected cluster sample was detected by the Planck satellite. We will describe the theoretical modelling of the expected abundance in Sec. 2.2.1 in detail as it will also form the foundation for the forecasts in Sec. 2.3. While the discussion presented here follows the spirit of the official cluster cosmology papers (Planck Collaboration et al., 2014a; Planck Collaboration et al., 2015) and shares notation wherever possible to make a connection to their approach easier, it simplifies various expressions and corrects several numerical implementations. The resulting likelihood code is also faster than the original implementation by a factor of ≈ 10 . Note however that the errors in the original Planck likelihood only have minor consequences and do not lead to any qualitative changes for the resulting cosmological parameters.

We also address the form of the cluster likelihood used to extract cosmological results from the sample in Sec. 2.2.2 and present the consequences for the derived cosmology in Sec. 2.2.3.

2.2.1 Modelling of number counts

The fundamental observable for Planck is the cluster redshift z and the signal-to-noise of the detection q . The expected average number counts per bin in z and q can then be written formally as

$$\mu_{ij} = \int_{\Delta z_i} dz \int_{\Delta q_j} dq \frac{dn}{dzdq}, \quad (2.7)$$

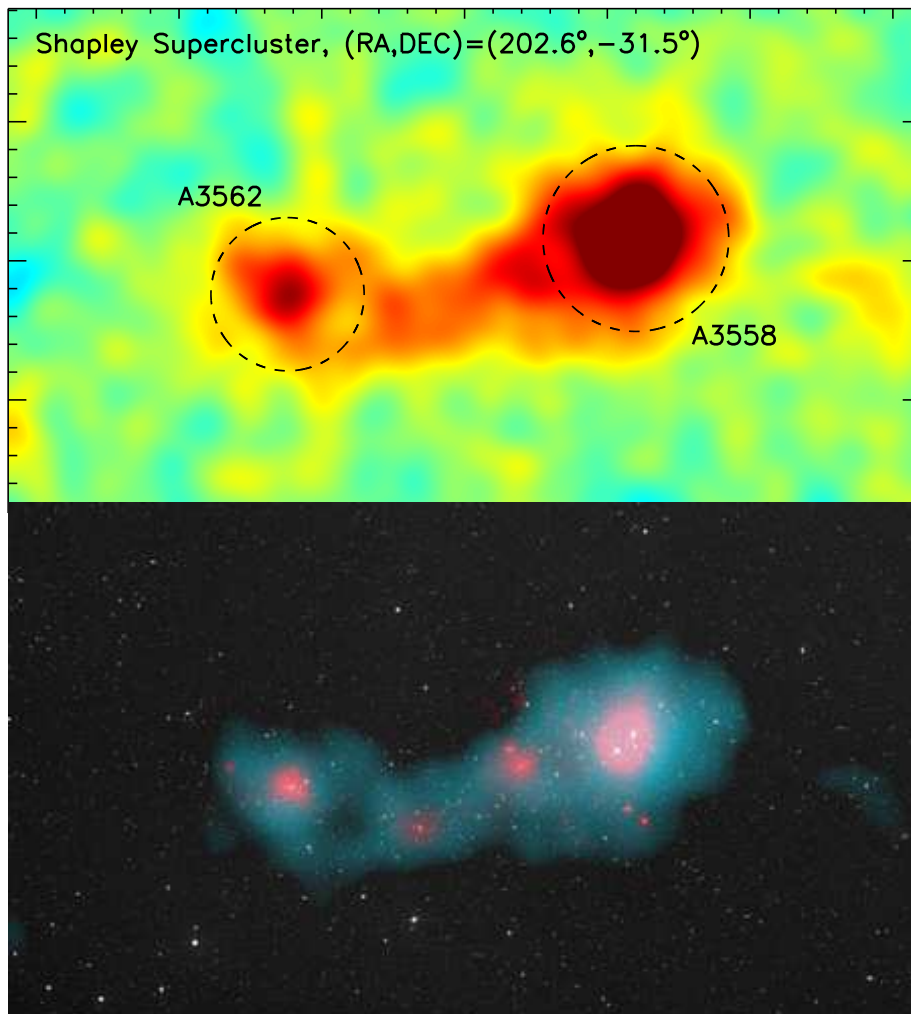


FIGURE 2.2: The Shapley supercluster as seen by Planck in the Compton y map (top) and on the bottom a composite image consisting of optical DSS data (white), X-ray emission from ROSAT (red) and Planck SZ (blue).
Plot from Planck Collaboration et al., [2014b](#)

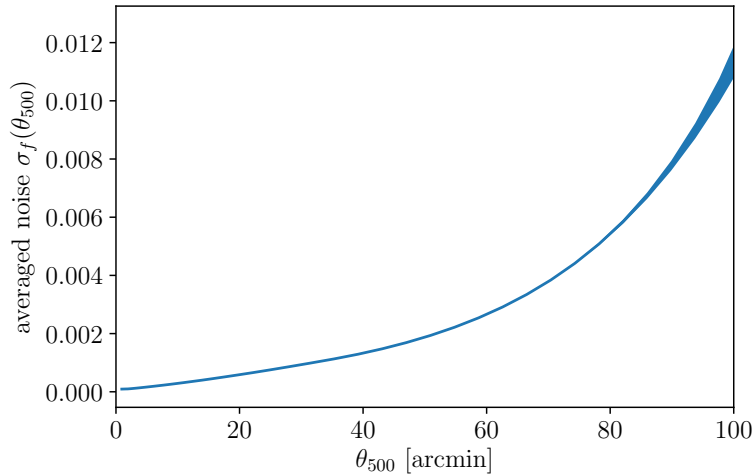


FIGURE 2.3: Planck sky-averaged noise as a function of the angular beam size θ_{500} . The line width indicates 1σ variance over the unmasked sky, so the Planck noise map is quite homogeneous.

with

$$\frac{dn}{dzdq} = \int d\Omega \int dM_{500} \frac{dn}{dVdM_{500}} \frac{dV}{dzd\Omega} P(q|\bar{q}_{\text{theo}}(M_{500}, z, \mathbf{n})), \quad (2.8)$$

given by the mass function, the cosmological volume element and a mass-observable-relation. Planck uses masses defined as

$$\frac{4}{3}\pi R_{500c}^3 \times 500 \times \rho_{\text{crit}} \equiv M_{500}, \quad (2.9)$$

and to stay consistent with the Planck publications in this chapter we will use the mass function by Tinker (Tinker et al., 2008) calibrated to this definition with a suite of N -body simulations.

The crucial component to connect the theoretical halo abundance given by the mass function with observed cluster counts is the probability $P(q|\bar{q}_{\text{theo}})$ to observe a cluster with signal-to-noise q , given a halo mass M_{500} and redshift z . The theoretical signal-to-noise value \bar{q}_{theo} is predicted from the ratio of the expected average Compton y -parameter \bar{Y}_{500} integrated over the area covered by a cluster with mass M_{500} at redshift z , and filter noise σ_f :

$$\bar{q}_{\text{theo}}(M_{500}, z, \mathbf{n}) \equiv \frac{\bar{Y}_{500}(M_{500}, z)}{\sigma_f(\theta_{500}(M_{500}, z), \mathbf{n})}. \quad (2.10)$$

The noise itself depends on the angular size of the cluster $\theta_{500}(M_{500}, z)$ and the position in the sky \mathbf{n} . We show the noise term for Planck as a function of the beam size in Fig. 2.3, together with its variance over the sky – the Planck beam noise is fairly uniform. For the integrated SZ flux Y_{500} and the corresponding angular size θ_{500} , we follow the relations derived in Planck Collaboration et al., 2014a; Planck Collaboration

et al., 2015 of the form

$$\bar{Y}_{500} = Y_* \left(\frac{h}{0.7} \right)^{-2+\alpha} \left(\frac{(1-b_M)M_{500}}{3 \times 10^{14} M_\odot} \right)^\alpha E^\beta(z) \left(\frac{500 \text{ Mpc}}{D_A(z)} \right)^2, \quad (2.11)$$

$$\theta_{500} = \theta_* \left(\frac{h}{0.7} \right)^{-2/3} \left(\frac{(1-b_M)M_{500}}{3 \times 10^{14} M_\odot} \right)^{1/3} E^{-2/3}(z) \left(\frac{500 \text{ Mpc}}{D_A(z)} \right), \quad (2.12)$$

where $\theta_* = 6.997$ arcmin and Y_* , α and β are nuisance parameters with priors given in Tab. 2.1. The relations are derived under the assumption of hydrostatic equilibrium, but this is not always fulfilled. Mergers and accretion of material cause turbulent flows (Shi and Komatsu, 2014), and non-thermal pressure is sourced by high-energy cosmic rays and magnetic field inside the cluster. The consequence is an offset between hydrostatic mass estimates and the true cluster mass expressed by the global mass bias parameter $(1 - b_M)$, which will be discussed in detail together with the main cosmological results in Sec. 2.2.3. The noise dependence on the angular cluster size introduces a mass- and redshift dependence of the selection function and spoils the idealized arguments outlined above in Sec. 2.1.

The probability distribution itself has two components

$$P(q|\bar{q}(M_{500}, z, \mathbf{n})) = \int dq_{\text{theo}} P(q|q_{\text{theo}}) P(q_{\text{theo}}|\bar{q}_{\text{theo}}), \quad (2.13)$$

where $P(q|q_{\text{theo}})$ is the probability to observe q given a predicted value q_{theo} . We assume Gaussian noise

$$P(q|q_{\text{theo}}) = \frac{1}{\sqrt{2\pi}} e^{-(q-q_{\text{theo}})^2/2}, \quad (2.14)$$

which follows a standard distribution with width 1 because the signal-to-noise is already expressed in units of σ_f . The second term includes a log-normal scatter between q_{theo} and the mean relation \bar{q}_{theo}

$$P(q_{\text{theo}}|\bar{q}_{\text{theo}}) = \frac{1}{\sqrt{2\pi}\sigma_{\ln Y}} \exp\left(-\frac{(\ln q_{\text{theo}} - \ln \bar{q}_{\text{theo}})^2}{2\sigma_{\ln Y}^2} \right), \quad (2.15)$$

given by the scatter around the mean \bar{Y}_{500} relation (Eq. 2.11) characterised by $\sigma_{\ln Y}$. It is convenient to split the contribution into observables (Y_{500}, θ_{500}) and underlying inferred cluster parameters (M_{500}, z). We do this by reconsidering the expected average number counts μ per bin

$$\mu_{ij} = \int_{\Delta z_i} dz \frac{dV}{dz} \int_{\Delta q_j} dq \int_0^\infty dM \int d\Omega \int d\bar{q}_{\text{theo}} \frac{dn}{dM}(z) P(q|q_{\text{theo}}) P(q_{\text{theo}}|\bar{q}_{\text{theo}}), \quad (2.16)$$

and re-ordering the integrations to arrive at

$$\mu_{ij} = \int_{\Delta z_i} dz \frac{dV}{dz} \int_0^\infty dM \frac{dn}{dM}(z) \underbrace{\int d\bar{q}_{\text{theo}} P(q_{\text{theo}}|\bar{q}_{\text{theo}}) \int d\Omega \int_{\Delta q_j} dq P(q|q_{\text{theo}})}_{\chi(\bar{Y}_{500}(M,z), \bar{\theta}_{500}(M,z), q_j)}, \quad (2.17)$$

where we introduced the survey completeness function χ that gives the detection probability of a cluster. The integration over q can be solved analytically using Eqs. 2.10

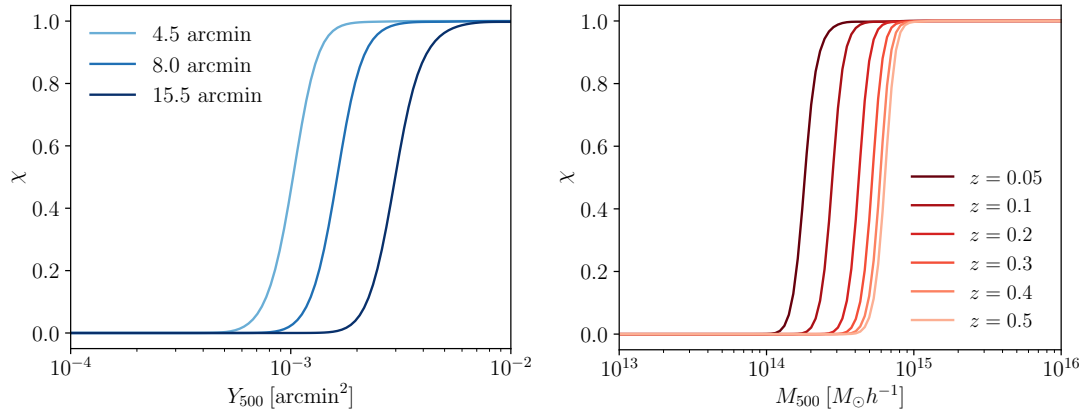


FIGURE 2.4: **Left:** Planck completeness χ for three fixed angular sizes corresponding to a cluster of mass $3 \times 10^{14} M_{\odot} h^{-1}$ observed at redshift $z = 0.2$, $z = 0.1$ and $z = 0.05$ (from left to right). **Right:** Completeness in terms of cluster mass using the scaling relation Eq. 2.11. The left-most line corresponds to redshift $z = 0.05$ and subsequent curves are shown for steps $\Delta z = 0.1$ assuming the fiducial cosmology.

and 2.14

$$\int_{q_j^{\min}}^{q_j^{\max}} dq \exp\left(-\frac{(q - q_{\text{theo}})^2}{2}\right) = \int_{q_j^{\min}}^{q_j^{\max}} dq \exp\left(-\frac{\left(q\sigma_f(\theta_{500}, \mathbf{n}) - Y_{500}(M, z)\right)^2}{2\sigma_f^2(\theta_{500}, \mathbf{n})}\right) \quad (2.18)$$

$$= \frac{1}{2} \left(\text{erfc}(x_j^{\min}) - \text{erfc}(x_j^{\max}) \right) \quad (2.19)$$

using standard Gaussian integrals, and we introduced the shorthand

$$x_j^{\min} \equiv \frac{q_j^{\min}\sigma_f - Y_{500}(M_{500}, z)}{2\sigma_f^2}, \quad (2.20)$$

$$x_j^{\max} \equiv \frac{q_j^{\max}\sigma_f - Y_{500}(M_{500}, z)}{2\sigma_f^2}. \quad (2.21)$$

The survey completeness χ expressed as function of Y_{500} and θ_{500} is then independent of cosmology and can be tabulated beforehand to speed up the evaluations of the likelihood function dramatically. χ is shown in Fig. 2.4 for various angular sizes corresponding to a typical cluster at various redshifts (left), and converted to a function of mass in the fiducial cosmology (right).

The model for the cosmological Planck cluster catalogue is defined as discussed in the previous section together with a signal-to-noise cut $q > 6$. This can be equivalently expressed as a limiting mass $M_{\text{lim}}(z)$ for the survey by the condition

$$\chi(Y_{500}(M_{\text{lim}}), \theta_{500}(M_{\text{lim}}), q > 6) = \frac{1}{2}, \quad (2.22)$$

which gives the redshift-dependent mass limit for a cluster to be detected with probability 1/2. It depends weakly on cosmology via the angular diameter distance in Eq. 2.11, but it is mainly set by the cluster mass scale $(1 - b_M)$ and the amplitude of

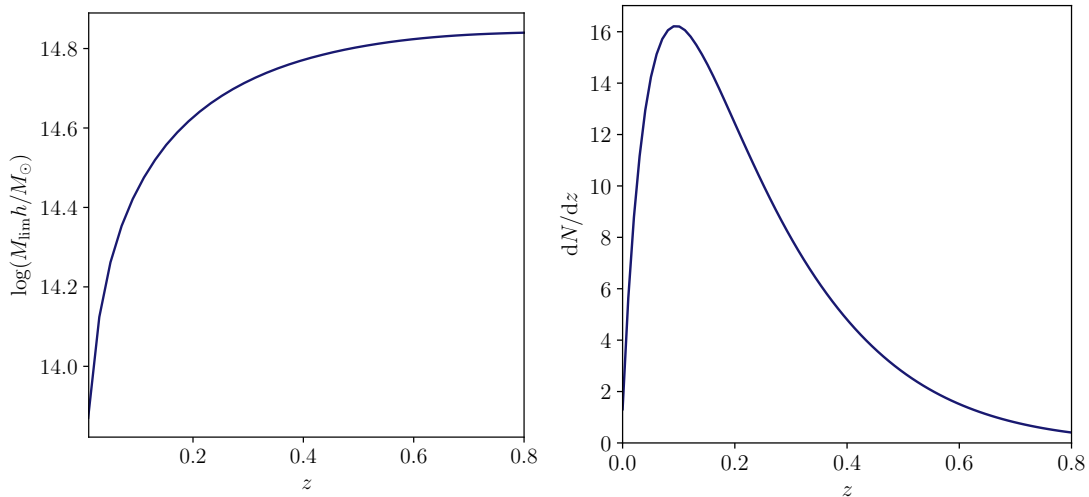


FIGURE 2.5: **Left:** Limiting mass for the Planck SZ cluster sample assuming the fiducial cosmology and $(1 - b_M) = 0.8$. **Right:** Resulting theoretical redshift distribution of the Planck SZ cluster sample. Most clusters are very massive and nearby, very few objects at $z > 0.5$ surpass the detection threshold.

the scaling relation Y_* . The redshift dependence of M_{lim} is shown in Fig. 2.5 (left) for the fiducial cosmology, which demonstrates that the Planck noise properties lead to a considerable evolution of the selection function at lower redshifts. At high redshift the angular diameter distance flattens, so there is less evolution in the limiting mass. The resulting cluster redshift distribution in Fig. 2.5 (right) is peaked at low redshifts $z \approx 0.1$ and quickly drops off because at high redshifts very few objects are massive enough to surpass the detection threshold.

2.2.2 Likelihood and correlated cluster abundance

We now have the complete theoretical model in place to predict the observed cluster abundance. The last piece missing to connect the observed sample to the underlying cosmology is the likelihood $\mathcal{L}(N | (\Omega_m, \sigma_8, \dots))$ to observe N clusters given an underlying cosmology. We note from Fig. 2.5 that the Planck clusters are extremely massive and therefore rare objects, so we start by assuming that they follow a Poisson distribution within each bin in redshift Δz_i and signal-to-noise Δq_j

$$\mathcal{L}(N_{ij} | \mu_{ij}) = \frac{\mu_{ij}^{N_{ij}}}{N_{ij}!} e^{-\mu_{ij}}, \quad (2.23)$$

with the observed cluster counts N_{ij} , and the predicted mean abundances $\mu_{ij}(\Omega_m, \sigma_8, \dots)$ calculated given the cosmological parameters. If the abundance in each bin is uncorrelated, the total probability is simply a product of the individual probabilities, and the resulting log-likelihood takes the form

$$\ln \mathcal{L}(N_1, N_2, \dots | \mu_1, \mu_2, \dots) = \ln \prod_{ij} \mathcal{L}_{ij}(N_{ij} | \mu_{ij}) = \sum_{ij} N_{ij} \ln \mu_{ij} - \mu_{ij} - \ln(N_{ij}!). \quad (2.24)$$

This was also assumed by the original cosmological analysis of the Planck cluster sample. However, as surveys resolve the clusters tracing the underlying density field

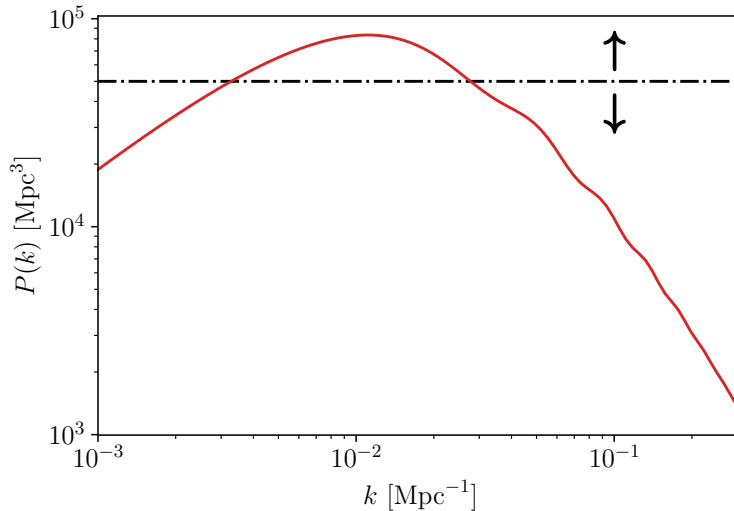


FIGURE 2.6: Halo power spectrum $b^2 P(k)$ (red) and a white shot-noise spectrum $1/\bar{n}$ (dot-dashed) as expected from tracers with density \bar{n} corresponding to the observed Planck clusters up to $z = 0.1$. For a sample with very low density, the white noise dominates and the clusters are uncorrelated – they follow a Poisson distribution.

in higher and higher numbers, their abundance will start to show an imprint of the large scale structure they are embedded in. Halos form in dense regions, so they are biased tracers of the density field. Their power spectrum P_{hh} is to linear order given by

$$P_{hh} = b^2 P(k) + \frac{1}{\bar{n}}, \quad (2.25)$$

with the linear clustering bias b and the matter power spectrum $P(k)$. Discrete tracers have an additional white noise contribution $1/\bar{n}$ that is proportional to the tracer density \bar{n} (Baldauf et al., 2013). If the correlation structure is buried under white noise, i.e. $b^2 P(k) \ll 1/\bar{n}$, individual halos are uncorrelated and follow a Poisson distribution. We will come back to this point in more detail later.

In Fig. 2.6 we compare the halo power spectrum for a linear bias $b \approx 4$ with the shot noise contribution from Planck SZ clusters up to $z = 0.1$. As we can see, no term is clearly dominant. Physically, this means long-wavelength perturbations might introduce correlations between different mass bins and lead to deviations from Eq. 2.23.

To estimate the impact of these large-scale modes of the density field, we consider the average density fluctuation inside the survey volume V_s (Hu and Kravtsov, 2003; Hu and Cohn, 2006; Takada and Spergel, 2014):

$$\bar{\delta}_s(V_s) \equiv \int d\mathbf{x}^3 \delta(\mathbf{x}) W(\mathbf{x}, V_s), \quad (2.26)$$

with the window function $W(\mathbf{x}) = 1$ inside the survey volume. For now we neglect bins in redshift and assume the complete survey volume, but we will return to the problem of different redshift bins later. Since the halo bias is the linear response of the halo field to fluctuations in the density field, the average number of clusters in the survey $\tilde{\mu}$ differs from the global (universe-wide) average μ for $\bar{\delta}_m \neq 0$ by

$$\tilde{\mu}(V_s) = \mu(V_s) (1 + b \bar{\delta}_s). \quad (2.27)$$

As long as the survey volume is sufficiently large, small scale fluctuations average out and the mean deviation $\bar{\delta}_s$ from the background density is only caused by coherent long-wavelength perturbations comparable or larger than the survey volume. Therefore these modes are not observable by the survey itself and they contribute to an additional error budget in the same way as cosmic variance. The large scales are still in the linear regime, and their density contrast follows a Gaussian distribution

$$p(\bar{\delta}_s) = \frac{1}{\sqrt{2\pi}\sigma_s} \exp\left(-\frac{\bar{\delta}_s^2}{2\sigma_s^2}\right), \quad (2.28)$$

with the variance of the density field inside the survey volume

$$\sigma_s^2 \equiv \int \frac{d\mathbf{k}^3}{(2\pi)^3} P(k) \tilde{W}^2(\mathbf{k}, V_s), \quad (2.29)$$

calculated from the linear matter power spectrum $P(k)$ and the Fourier-transformed survey window function $\tilde{W}(\mathbf{k}, V_s)$. Using Eq. 2.27, the likelihood for a single mass bin now reads

$$\tilde{\mathcal{L}}(N|\tilde{\mu}) = \frac{\tilde{\mu}^N}{N!} \exp(-\tilde{\mu}) = \frac{\mu^N (1 + b\bar{\delta}_s)^N}{N!} \exp\left(-\mu(1 + b\bar{\delta}_s)\right), \quad (2.30)$$

and we expand it to second order in $\bar{\delta}_s$ using

$$(1 + b\bar{\delta}_s)^N \approx 1 + Nb\bar{\delta}_s + \frac{N(N-1)}{2} (b\bar{\delta}_s)^2, \quad (2.31)$$

$$\exp(-\mu b\bar{\delta}_s) \approx 1 - \mu b\bar{\delta}_s + \frac{1}{2} (\mu b\bar{\delta}_s)^2, \quad (2.32)$$

to arrive at

$$\tilde{\mathcal{L}}(N|\tilde{\mu}) \approx \mathcal{L}\left(1 + Nb\bar{\delta}_s + \frac{N(N-1)}{2} (b\bar{\delta}_s)^2\right) \left(1 - \mu b\bar{\delta}_s + \frac{1}{2} (\mu b\bar{\delta}_s)^2\right), \quad (2.33)$$

with the unperturbed Poisson-likelihood $\mathcal{L} \equiv \mathcal{L}(N|\mu)$. The joint likelihood for multiple mass bins with the observed abundance N_1, N_2, \dots is still given by the product

$$\begin{aligned} \mathcal{L}^{\text{tot}}(N_1, \dots; \bar{\delta}_s) &= \prod_i \tilde{\mathcal{L}}_i(N_i|\tilde{\mu}_i) \\ &\approx \prod_i \mathcal{L}_i \left(1 + \sum_i N_i b_i \bar{\delta}_s + \sum_{i \neq j} b_i N_i b_j N_j \bar{\delta}_s^2 + \sum_i \frac{N_i(N_i-1)}{2} (b_i \bar{\delta}_s)^2\right) \\ &\quad \times \left(1 - \sum_i \mu_i b_i \bar{\delta}_s + \sum_{i \neq j} b_i \mu_i b_j \mu_j \bar{\delta}_s^2 + \frac{1}{2} \sum_i (\mu_i b_i \bar{\delta}_s)^2\right), \end{aligned} \quad (2.34)$$

where we dropped terms beyond second order in $\bar{\delta}_s$, and the total likelihood receives additional contributions from cross-terms $i \neq j$. After ordering all contributions in

powers of $\bar{\delta}_s$, we arrive at

$$\begin{aligned} \mathcal{L}^{\text{tot}}(N_1, \dots; \bar{\delta}_s) &\approx \prod_i \mathcal{L}_i \left(1 + \sum_i (b_i N_i - b_i \mu_i) \bar{\delta}_s + \left[\sum_{i \neq j} b_i N_i b_j N_j + \sum_{i \neq j} b_i \mu_i b_j \mu_j \right. \right. \\ &\quad \left. \left. - \sum_{ij} b_i N_i b_j \mu_j + \sum_i \frac{N_i(N_i - 1)}{2} b_i^2 + \frac{1}{2} \sum_i b_i^2 \mu_i^2 \right] \bar{\delta}_s^2 \right) \\ &= \prod_i \mathcal{L}_i \left(1 + \sum_i (b_i N_i - b_i \mu_i) \bar{\delta}_s + \frac{1}{2} \left[\left(\sum_i b_i (N_i - \mu_i) \right)^2 - \sum_i b_i^2 N_i \right] \bar{\delta}_s^2 \right). \end{aligned} \quad (2.35)$$

Since the mean density deviation inside the survey volume $\bar{\delta}_s$ can not be known, we integrate over it using the probability distribution in Eq. 2.28. All terms $\sim \bar{\delta}_s$ vanish as integrals over odd-parity functions, while for the contribution $\sim \bar{\delta}_s^2$ we can rewrite the integral using

$$\int x^2 \exp(-ax^2) = - \int \frac{\partial}{\partial a} \exp(-ax^2) = - \frac{\partial}{\partial a} \sqrt{\frac{\pi}{a}} = \frac{\sqrt{\pi}}{2a^{3/2}}, \quad (2.36)$$

and thus the integration yields

$$\frac{1}{\sqrt{2\pi\sigma_s}} \int \bar{\delta}_s^2 \exp\left(\frac{\bar{\delta}_s^2}{2\sigma_s^2}\right) d\bar{\delta}_s = \sigma_s^2. \quad (2.37)$$

We therefore arrive at the final result, the joint likelihood to observe (N_1, N_2, \dots) clusters in bins $(\Delta M_1, \Delta M_2, \dots)$ after marginalizing over the super-survey modes (Hu and Cohn, 2006; Takada and Spergel, 2014)

$$\mathcal{L}^{\text{tot}} = \prod_i \mathcal{L}_i \left(1 + \frac{1}{2} \left[\left(\sum_i b_i (N_i - \mu_i) \right)^2 - \sum_i b_i^2 N_i \right] \sigma_s^2 \right). \quad (2.38)$$

Note that this is still a normalized probability distribution,

$$\sum_{N_1=0}^{\infty} \sum_{N_2=0}^{\infty} \dots \mathcal{L}^{\text{tot}}(N_1, N_2, \dots) = 1, \quad (2.39)$$

and therefore we can derive the moments of the cluster distribution with Eq. 2.38. To do this, we start from a single mass bin and use the moments of the unperturbed Poisson distribution (as a shorthand we write $\langle \dots \rangle_P$ for corresponding Poisson-averages using Eq. 2.23)

$$\langle N \rangle_P \equiv \sum_{N=0}^{\infty} N \mathcal{L} = \mu \quad (2.40)$$

$$\langle N^2 \rangle_P = \mu^2 + \mu \quad (2.41)$$

$$\langle N^3 \rangle_P = \mu^3 + 3\mu^2 + \mu, \quad (2.42)$$

to write

$$\begin{aligned}
\langle N \rangle &\equiv \sum_{N=0}^{\infty} N \tilde{\mathcal{L}}(N) \\
&= \sum_{N=0}^{\infty} N \left(\frac{\mu^N}{N!} e^{-\mu} \right) \left(1 + \frac{1}{2} \left[(b(N-\mu))^2 - b^2 N \right] \bar{\sigma}_s^2 \right) \\
&= \langle N \rangle_P + \frac{1}{2} b^2 \sigma_s^2 \left(\langle N(N-\mu)^2 \rangle_P - \langle N^2 \rangle_P \right) \\
&= \underbrace{\langle N \rangle_P}_{\mu} + \frac{1}{2} b^2 \sigma_s^2 \left(\underbrace{\langle N^3 \rangle_P}_{\mu^3 + 3\mu^2 + \mu} - 2\mu \underbrace{\langle N^2 \rangle_P}_{\mu^2 + \mu} + \mu^2 \underbrace{\langle N \rangle_P}_{\mu} - \underbrace{\langle N^2 \rangle_P}_{\mu^2 + \mu} \right) \\
&= \mu,
\end{aligned} \tag{2.43}$$

so as expected the mean of the distribution is not affected by the Gaussian fluctuations in the density field. In similar fashion, we can derive

$$\langle N^2 \rangle = \sum_{N=0}^{\infty} N^2 \mathcal{L}(N) = \mu + \mu^2 + b^2 \mu^2 \sigma_s^2, \tag{2.44}$$

and therefore the variance reads

$$\langle N^2 \rangle - \langle N \rangle^2 = \mu + b^2 \mu^2 \sigma_s^2, \tag{2.45}$$

which now has a Poisson-like contribution from the limited number of objects and a sample variance term that includes the effect of correlated large-scale structure modes via σ_s^2 . Note that, as the volume grows large $V_s \rightarrow \infty$, the mean density in the survey $\bar{\delta}_s$ will approach the mean density of the universe, $\bar{\delta} = 0$ and we get $\sigma_s^2 \rightarrow 0$.

The generalization to more mass bins is lengthy but straightforward, so we just briefly summarize the results. For the joint distribution of two bins, from Eq. 2.38 we get

$$\langle N_i N_j \rangle \equiv \sum_{N_i=0}^{\infty} \sum_{N_j=0}^{\infty} N_i N_j \mathcal{L}(N_i, N_j) = \mu_i \mu_j + b_i \mu_i b_j \mu_j \sigma_s^2, \tag{2.46}$$

and consequently the covariance between bins is

$$\langle N_i N_j \rangle - \langle N_i \rangle \langle N_j \rangle = b_i \mu_i b_j \mu_j \sigma_s^2, \tag{2.47}$$

so mass bins inside the same volume are positively correlated due to the coherent, large scale modes: if a survey is on average overdense $\bar{\delta}_s > 0$, number counts in all mass bins will be shifted upwards proportional to their respective bias (and vice versa for underdense regions).

Finally, we consider bins not only in mass, but also in redshift. The discussion above remains unchanged, except that now we have to consider the window functions of different redshift bins when calculating σ_s^2 . The straightforward generalization of Eq. 2.29 is

$$\sigma_s^2(z_l, z_m) \equiv \int \frac{d\mathbf{k}^3}{(2\pi)^3} P(k, z_{\text{med}}) \tilde{W}(\mathbf{k}, V_l) \tilde{W}(\mathbf{k}, V_m), \tag{2.48}$$

with the window functions of the volume associated to redshift bins z_l and z_m . The power spectrum is evaluated at the median redshift z_{med} for simplicity. The redshift evolution of $P(k)$ is only a minor effect: either the bins are large and σ_s^2 small due to averaging over a large volume, or the bins are narrow $\Delta z \leq 0.1$ and the growth

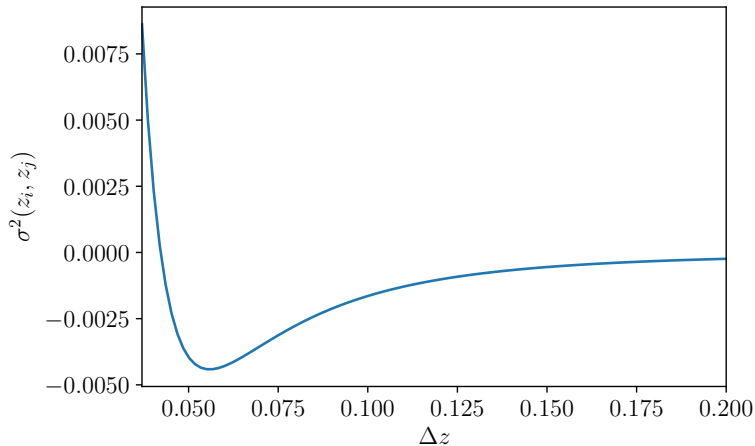


FIGURE 2.7: Cross-correlation coefficient of neighbouring redshift bins from Eq. 2.48 for spherical shells with width Δz . The inner shell is centred at $z = 0$. The transition from positive to negative correlation is set by the wavelength of modes around the peak of the power spectrum corresponding to a physical size of ≈ 150 Mpc or $\Delta z \approx 0.04$ for our fiducial cosmology.

function does not change significantly over the bin. For a real survey the bin geometry, observational completeness and masking affect the window function $\tilde{W}(\mathbf{k})$, and can be important sources of systematic uncertainty, but for now we consider full-sky spherical shells around the observer with equal width Δz to demonstrate the qualitative behavior.

We show $\sigma_s^2(z_l, z_m)$ calculated for our fiducial cosmology in Fig. 2.7. The typical correlation length is set by the wavelength of modes around the peak of the matter power spectrum, corresponding to a physical size ≈ 150 Mpc (or $z \approx 0.04$). Therefore, for Δz smaller than this scale, long wavelength modes couple the neighboring bins leading to a positive correlation. If the width is larger, bins are anticorrelated due to homogeneity – any departure from the mean density has to be compensated.

For a full-sky survey such as Planck and $\Delta z = 0.1$, we get $\sigma_s^2(\Delta z) \approx 10^{-4}$ for the first bin. We can then use Eq. 2.45 to estimate when the sample variance contribution to the statistical error becomes comparable to the Poisson noise

$$\mu \approx b^2 \mu^2 \sigma_s^2. \quad (2.49)$$

The massive Planck clusters have a mean bias of $b \approx 4$ and thus we get $\mu \approx 60$. This is a rough estimate, but as soon as there are more expected clusters per bin, sample variance contributes to the statistical error budget of the survey on the same level as Poissonian shot noise. For future surveys with very large cluster samples, this effect dominates the statistical error budget at low redshifts.

We also want to point out that the derived covariance from the perturbed Poisson statistics is still valid if one extends the likelihood to the Gaussian limit $\mu \gg 1$ (Hu and Cohn, 2006). The cluster abundance likelihood is then given by a multivariate Gaussian

$$\mathcal{L} = \frac{1}{\sqrt{2\pi \det \mathbf{C}^{-1}}} \exp\left(-\frac{1}{2}(\mathbf{N} - \boldsymbol{\mu})^T \mathbf{C}^{-1}(\mathbf{N} - \boldsymbol{\mu})\right) \quad (2.50)$$

with the measured cluster abundance vector \mathbf{N} , the prediction vector $\boldsymbol{\mu}$ and the covariance matrix from Eqs. 2.45 and 2.47

$$\mathbf{C}^{-1} = \begin{pmatrix} \mathcal{A}^1 & \mathcal{A}^{1 \times 2} & \dots \\ \mathcal{A}^{2 \times 1} & \mathcal{A}^2 & \\ \vdots & & \ddots \end{pmatrix} \quad (2.51)$$

which has a block structure with matrices along the diagonal for each redshift bin Δz_l

$$\mathcal{A}_{ij}^l = \delta_{ij} \mu_i + b_i \mu_i b_j \mu_j \sigma_s^2(\Delta z_l) \quad (2.52)$$

and the off-diagonal matrices coupling different redshift bins Δz_l and Δz_m

$$\mathcal{A}_{ij}^{l \times m} = b_i(z_l) \mu_i(z_l) b_j(z_m) \mu_j(z_m) \sigma_s^2(z_l, z_m). \quad (2.53)$$

2.2.3 Planck cluster cosmology

After the discussion of the cluster abundance model in Sec. 2.2.1 and the likelihood in Sec. 2.2.2, we now move towards cosmological results. We choose the width of the likelihood bins as $\Delta z = 0.1$ to ensure that photometric uncertainties in determining the cluster distance are negligible, and $\Delta \log q = 0.25$ (together with the signal-to-noise cut $q > 6$) as in the primary Planck cluster papers. The exact binning scheme does not change the results, apart from the fact that having a two-dimensional likelihood at all, with bins in redshift z and signal-to-noise q , helps to break degeneracies between cosmological- and nuisance parameters.

TABLE 2.1: Nuisance parameters for the scaling relations 2.11 and 2.12 used in the cosmological Planck cluster analysis. During the cosmological analysis, all of them are varied with Gaussian priors. For the mass bias $(1 - b_M)$ we choose between two priors provided by the CCCP collaboration (Hoekstra et al., 2015) or CMB lensing (Melin and Bartlett, 2015) as explained in the main text.

Parameter	Value
$\log Y_\star$	-0.19 ± 0.02
α	1.79 ± 0.08
β	0.66 (fixed)
$\sigma_{\ln Y}$	0.173 ± 0.023
$(1 - b_M)$ (CCCP)	0.78 ± 0.09
$1/(1 - b_M)$ (CMBlens)	0.99 ± 0.19

The nuisance parameters used for the scaling relations 2.11 and 2.12 are summarised in Tab. 2.1. Note that the fiducial value for the scaling of Y_{500} with mass $\alpha = 1.79 \pm 0.08$ is compatible with the value $5/3$ in Eq. 2.6 derived from virial scaling arguments. For the analysis, all nuisance parameters are varied with Gaussian priors together with the cosmological parameters. The only exception is the redshift evolution of the scaling relation β . It has only minor impact on the results because the clusters are mostly at low z , so we keep it fixed. For a detailed discussion we refer to Planck Collaboration et al., 2015, but we do want to point out that by far the most important parameter is the mass bias $(1 - b_M)$ which accounts for the difference between hydrostatic masses determined by X-ray or SZ measurements and the true

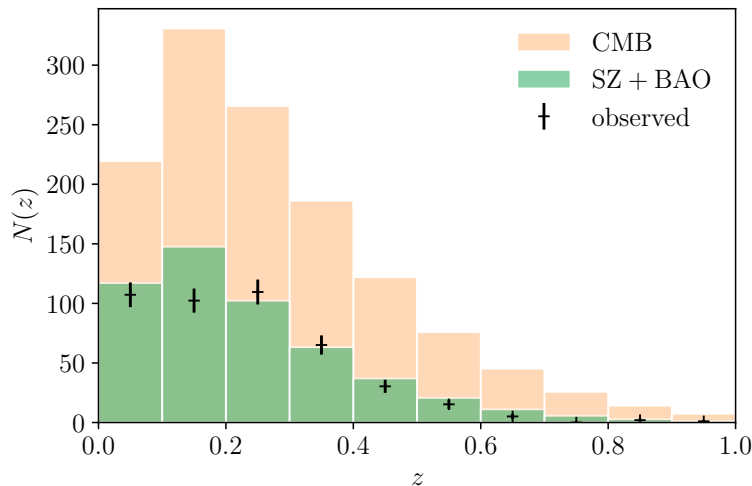


FIGURE 2.8: Binned redshift distribution of cluster number counts calculated for the Planck CMB cosmology and a mass bias $(1 - b_M) = 0.8$ (orange), and for the best fit cosmology for the SZ cluster catalogue combined with BAO data and the CCCP mass bias prior (green). Data points show the 438 observed clusters in the sample. The large discrepancy between CMB and cluster data in terms of the amplitude can mostly be expressed by the mass bias parameter, but the remaining mismatch is very difficult to explain by varying the standard model parameters.

cluster mass. Hydrodynamical N -body simulations suggest a value $(1 - b_M) \approx 0.8$ (Planck Collaboration et al., 2014a), roughly in agreement with measurements used here from either the Canadian Cluster Comparison Project (CCCP, Hoekstra et al., 2015) of 0.78 ± 0.09 using weak lensing follow-up observations of massive X-ray clusters, or an internal Planck mass calibration through CMB lensing by stacked clusters which yields a measurement of the inverse mass bias $1/(1 - b_M) = 0.99 \pm 0.19$ (Melin and Bartlett, 2015).

Concerning the underlying cosmological model, the cluster abundance is mostly sensitive to Ω_m and A_s , and it is customary to parametrize the latter in terms of σ_8 for late-time probes, even though we note that for our analysis this is a purely derived parameter. Cluster number counts have little to say about the remaining cosmological parameters, so we combine the Planck SZ catalogue with complementary data sets.

Baryon acoustic oscillation (BAO) measurements in the galaxy distribution provide a measurement of the distance scale $D_V(z)$, and we adopt a prior provided by the latest BOSS data release (Alam et al., 2017) at $z = 0.38, 0.51$ and 0.61 . The background geometry at low redshifts is governed by Ω_m and the Hubble constant, and because clusters constrain Ω_m , the BAO data effectively provide a measurement of H_0 . In addition, we add Big Bang nucleosynthesis constraints from Cooke et al., 2014 on the baryon density $\Omega_b h^2 = (2.224 \pm 0.046) \times 10^{-2}$. We will refer to the full combination of the cluster abundance and these data sets as SZ + BAO.

In Fig. 2.8 we show the binned redshift distribution of the cluster sample. The observed sample includes 438 objects centred at low redshifts $z < 0.3$. However, the cluster counts implied by the primary CMB cosmology together with a mass bias $(1 - b_M) = 0.8$ (orange) are by almost a factor of 3 higher than the measured abundance. The most obvious cure is the mass bias itself: a lower value implies that the Planck clusters are very massive, and the abundance of such halos is exponentially suppressed in the mass function. The determination of the Planck mass scale thus is

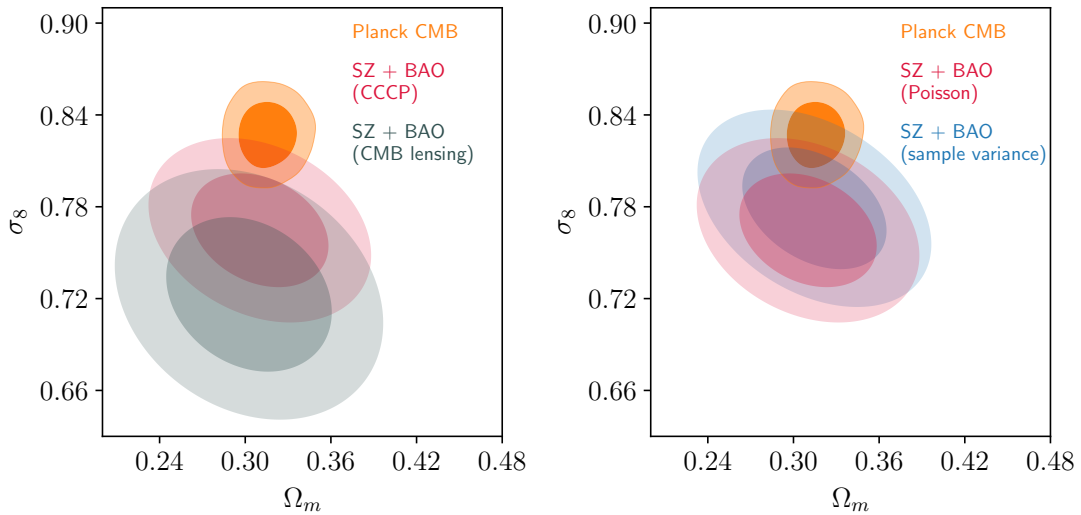


FIGURE 2.9: **Left:** Influence of the mass bias on the 68% and 95% constraints in the $\Omega_m - \sigma_8$ plane from the primary CMB (orange) and the SZ cluster sample combined with BAO data using the Poisson likelihood (Eq. 2.23). Red contours show the resulting posterior if the CCCP mass bias prior is adopted, while the CMB lensing mass bias prior leads to the grey contour. The degree of tension with the primary CMB depends strongly on the prior on $(1 - b_M)$. **Right:** Effect of the likelihood model on the SZ + BAO constraints using the CCCP mass bias prior. We compare results from the Poisson likelihood (Eq. 2.23, red) and including sample variance contributions (Eq. 2.38, blue). The modified likelihood slightly eases the tension with the primary CMB but is a small correction compared to uncertainty in the cluster masses.

crucial for the cosmological interpretation of the results. Note that also with a free mass bias disagreements between model and data remain. Especially the low counts in the second bin are very difficult to explain by varying any of the parameters. Again, we refer to Planck Collaboration et al., 2015 for a detailed discussion, but note that no obvious solutions exist so far.

However, if we take the expected value of $(1 - b_M) \approx 0.8$ at face value, we are left with a cosmological explanation. The clusters then imply lower values of σ_8 and Ω_m compared to the ones inferred from the CMB. To put this in more quantitative terms, we perform a full MCMC¹ analysis and present the resulting posterior in the $\Omega_m - \sigma_8$ plane in Fig. 2.9. On the left panel we demonstrate the large influence of the mass bias: the cluster abundance does prefer lower values of Ω_m and σ_8 as expected from Fig. 2.8, but the degree of tension is strongly dependent on the adopted value of $(1 - b_M)$. While the posterior is only in minor disagreement with the primary CMB if the CCCP mass bias prior is adopted, the high $(1 - b_M)$ from CMB lensing leads to significant discrepancy.

We also explore the effect of the extended likelihood model derived in the previous section and compare the resulting posterior for a Poisson likelihood Eq. 2.23 as used for the Planck cluster papers, and our modified Eq. 2.38 (Fig. 2.9, right panel). We find that the effect of sample variance on cluster abundance leads to slightly broader contours as expected from the additional contribution to the error budget, but the correlation between bins also shifts the posterior towards higher values of Ω_m and σ_8 ,

¹The likelihood is sampled using the MontePython code (Brinckmann and Lesgourgues, 2018)

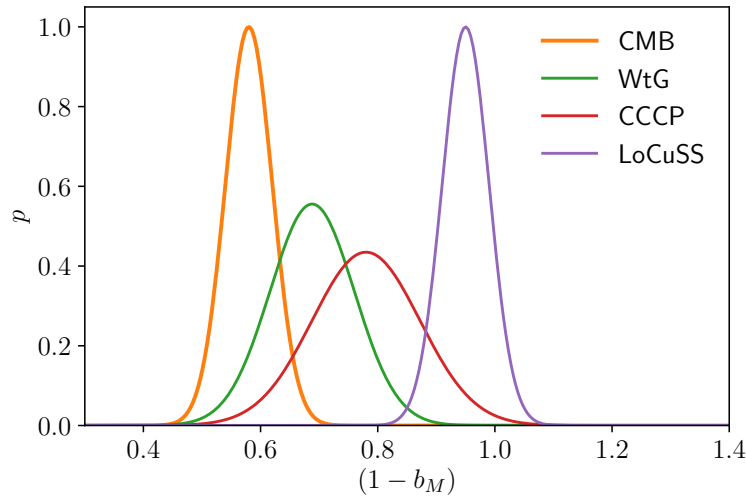


FIGURE 2.10: Various measurements of the bias $(1 - b_M)$ from comparisons of X-ray and weak lensing mass estimates. Also shown is the value inferred from a fit to SZ + CMB (orange). The reason for the conflicting measurements is currently unclear, but it seems safe to assume that systematic effects are not sufficiently under control.

easing the tension with the CMB. The cosmological analysis is however dominated by systematic uncertainty in the mass bias which remains the clearly dominant effect.

Much has been written about tension between the cosmology implied by the CMB and by low-redshift measurements (see e.g. MacCrann et al., 2015; Grandis et al., 2016; Efstathiou and Lemos, 2017), especially because there are tentative hints that other large-scale structure probes such as cosmic shear also prefer lower values of Ω_m and σ_8 (Hildebrandt et al., 2017; Abbott et al., 2017), even though not at significant levels for any single survey. Establishing a firm disagreement between cosmologies inferred from CMB and LSS is an enticing thought, because a physical explanation for the discrepancy seems hard to come by. But for the Planck cluster sample the degree of discordance crucially depends on the determination of the cluster mass scale. A joint fit of SZ + CMB with free mass bias leads to $(1 - b_M) = 0.58 \pm 0.04$ needed to bring the cluster abundance in agreement with the CMB results. The situation is complicated by conflicting measurements reported by various collaborations, ranging from $(1 - b_M) = 0.688 \pm 0.072$ found by the Weighing the Giants project (WtG, von der Linden et al., 2014) to $(1 - b_M) = 0.95 \pm 0.04$ (LoCuSS, Smith et al., 2016). We summarise these different results in Fig. 2.10. For now we conclude that the understanding of non-thermal pressure in clusters is lacking, and this is a major factor preventing us from fully exploiting the SZ or X-ray cluster abundance for cosmology.

2.3 From Planck to CORE

We now move towards forecasts for the Cosmic Origins Explorer² (CORE), a satellite mission recently proposed to ESA that would launch in the late 2020s. Its primary science goal is the detailed mapping of the primary CMB polarisation anisotropies (CORE Collaboration et al., 2018b) to potentially detect the imprint of primordial gravitational waves produced by inflation (CORE Collaboration et al., 2018d) on the B-mode power spectrum and to perform precise measurements of the gravitational

²<http://www.core-mission.org/>

lensing imprint on the CMB (CORE Collaboration et al., 2018c). In addition, similar to Planck, CORE would also be able to detect a multitude of galaxy clusters via the SZ effect. The analysis here builds upon the improved Planck cluster framework discussed in Sec. 2.2.1, but differs in the instrumental characteristics that we will address in Sec. 2.3.1. The cosmological forecasts are presented in Sec. 2.3.2.

The fiducial cosmology adopted in this section assumes $\Omega_m = 0.272$ and $\sigma_8 = 0.815$, slightly different from values used before. This was done to stay consistent with CORE sky simulations, but does not affect the results.

2.3.1 CORE cluster abundance

To predict the detected CORE clusters we apply the same underlying model as for Planck, but the larger telescope, improved detectors and the use of 15 instead of Planck’s nine frequency channels for better background subtraction lead to substantially lower effective instrumental noise, shown in Fig. 2.11. For smaller angular scales relevant to resolve clusters at high redshift, the overall noise is lower by an order of magnitude.

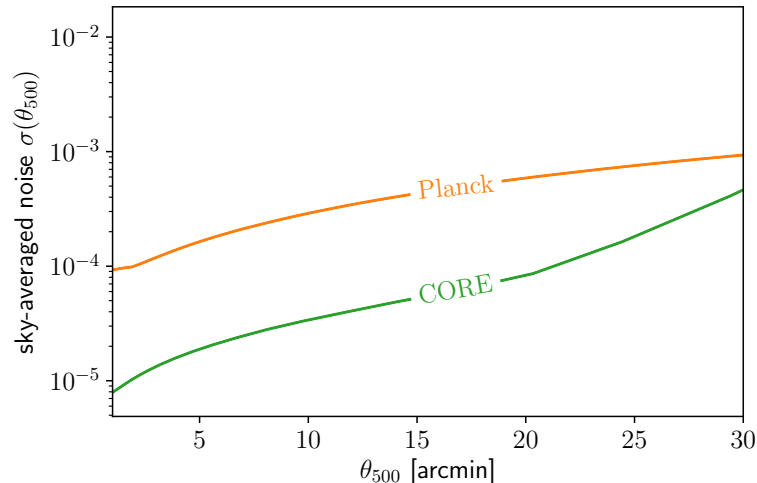


FIGURE 2.11: Sky-averaged noise as a function of the angular beam size θ_{500} for CORE compared to Planck. Note the logarithmic scale: for small angular sizes relevant to detect high-redshift clusters, CORE improves upon Planck by almost an order of magnitude.

This improves the signal-to-noise of sources in Eq. 2.10 and dramatically lowers the limiting mass of the CORE sample shown in Fig. 2.12 (left) compared to Planck. Again, we can see a strong evolution in the selection function for low redshifts and an almost constant M_{lim} for redshifts $z > 0.5$. The result is that CORE can detect all clusters in the universe with $M \gtrsim 10^{14} M_{\odot} h^{-1}$ over the unmasked fraction $f = 0.81$ of the sky. While this is also true for the Planck cluster sample, due to the higher threshold $M_{\text{lim}}(z > 0.5) \approx 10^{14.8} M_{\odot} h^{-1}$ at high redshifts barely any such objects exist.

The predicted redshift distribution in Fig. 2.12 (right) consists of ca. 10^5 clusters in total with a considerable amount of ca. 10^4 objects expected at $z > 1$ and still ≈ 1000 clusters at $z > 1.5$. The high-redshift samples are very valuable for breaking cosmological degeneracies: at high z the universe becomes increasingly matter dominated,

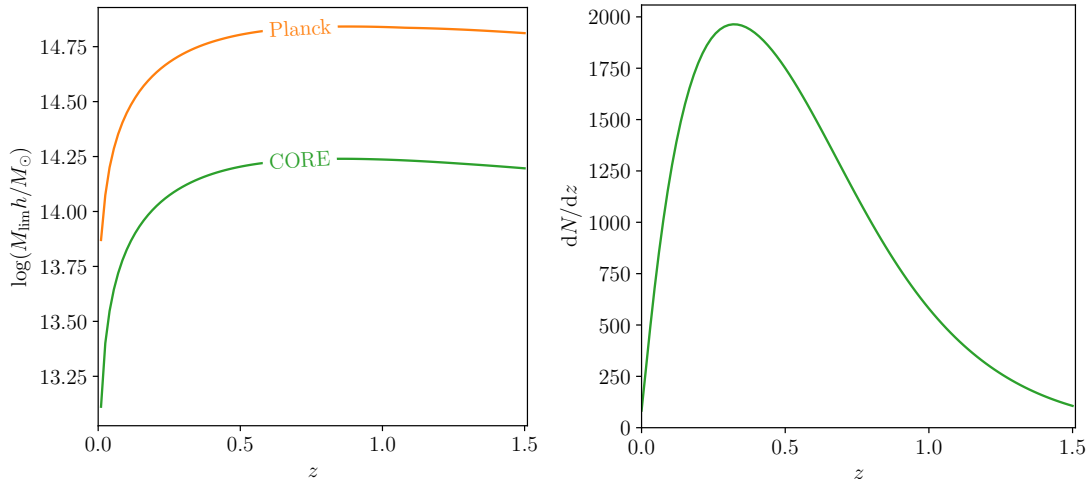


FIGURE 2.12: **Left:** Limiting mass of Planck (orange) compared to CORE (green) for the fiducial cosmology and $(1 - b_M) = 0.8$. **Right:** Resulting expected redshift distribution of the CORE sample with ca. 10^5 clusters. The sample peaks at $z \approx 0.35$ and is very deep, with a considerable number of objects detected at $z > 1$.

$\Omega_m(z) \rightarrow 1$, so the abundance there becomes insensitive to the exact value of Ω_m today and is mostly set by the amplitude of initial fluctuations A_s . This allows us to constrain both parameters separately.

2.3.2 Cosmological constraints from CORE

To compute the cosmological forecasts we adopt a signal-to-noise cut $q > 5$. CORE would start taking data around 2030 after other large-scale structure surveys such as Euclid³ and LSST⁴, so we assume that at least photometric redshift estimates for all clusters in the sample are available. We then choose bins in redshift with conservative width $\Delta z = 0.1$ to ensure that photometric errors are negligible. This leads to well-populated bins, each containing at least several hundred objects, so the cluster likelihood is well approximated by the Gaussian likelihood (Eq. 2.50) including the correlation and sample variance contribution unless stated otherwise.

For the nuisance parameters of the scaling relations we adopt a conservative default case and use the same priors as given in Tab. 2.1. Since for this deep sample the redshift evolution β of the scaling relations becomes important, we also vary it within a Gaussian prior $\beta = 0.66 \pm 0.5$ (Planck Collaboration et al., 2015). Concerning the mass bias, we assume a fiducial value of $(1 - b_M) = 0.8$ and distinguish between a calibration accurate to either 5% as a default case, or an optimistic determination of the cluster mass scale to 1% if indicated.

In Fig. 2.13 we present the constraints from CORE cluster counts in the $\Omega_m - \sigma_8$ plane. For the default case we vary all cosmological- and nuisance parameters supposing only current knowledge about the scaling relations. We also adopt a constrained case where we keep everything except Ω_m , σ_8 and $(1 - b_M)$ fixed, thus assuming that the nuisance parameters are known to high precision from independent observations. Since we can expect major improvements provided by upcoming X-ray surveys such

³<http://sci.esa.int/euclid/>

⁴<https://lsst.org/>

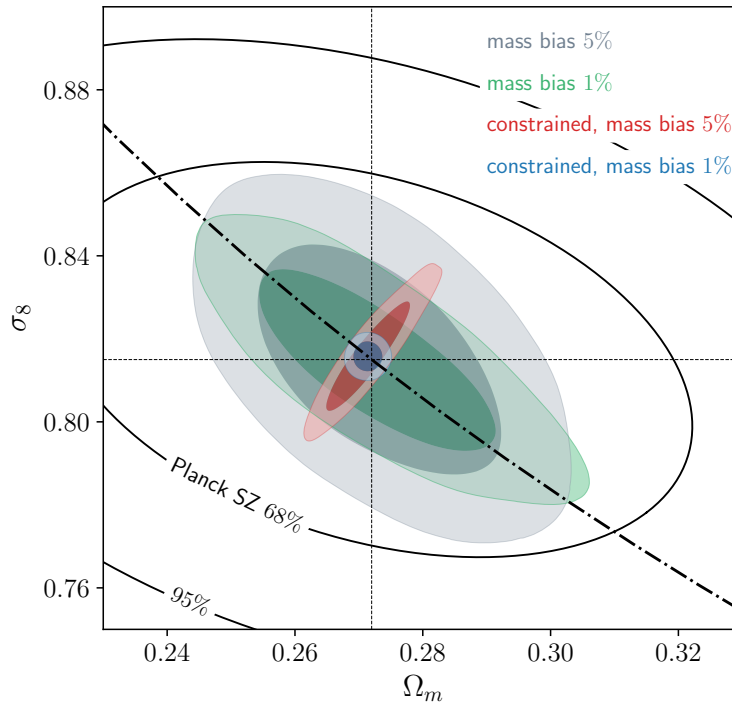


FIGURE 2.13: Expected constraints in the $\Omega_m - \sigma_8$ plane from CORE cluster number counts with different assumptions on the scaling relations. For the constrained case, all parameters except Ω_m , σ_8 and $(1 - b_M)$ are fixed. The dot-dashed line indicates the main degeneracy direction $\sim \sigma_8 \Omega_m^{0.4}$ of the unconstrained case with 5% uncertainty on the mass bias. For comparison we also show the Planck SZ + BAO cluster contours shifted to the fiducial CORE cosmology (solid black).

as eRosita⁵ and ground-based CMB observations by the Atacama Cosmology Telescope⁶ and the South Pole Telescope⁷, the real case should fall somewhere in between the two. To put the forecast into context, we also show the Planck SZ + BAO contours from the previous section shifted to the fiducial CORE cosmology. The improvement is quite significant, and the area covered by constraints in the $\Omega_m - \sigma_8$ plane shrinks by at least a factor of ≈ 4 . Note that the extension of the constraints perpendicular to the main degeneracy direction $\sim \sigma_8 \Omega_m^q$ with $q \approx 0.4$ is mostly governed by the mass bias as discussed in Sec. 2.2.3, while the other scaling relation parameters are more important for the extend along the dot-dashed line in Fig. 2.13.

We also investigate the role of sample variance by comparing the marginalized posteriors in the $\Omega_m - \sigma_8$ plane obtained from the correlated Gaussian likelihood (Eq. 2.50) with a Poisson likelihood (Eq. 2.23) in Fig. 2.14. For the default case with all cosmological and nuisance parameters varied (left) we find only a minor broadening of the contours when sample variance effects are included in the analysis. This has several reasons: The error budget of the CORE cluster analysis is strongly dominated by systematic effects, that is to say by the uncertainty in the scaling relations as demonstrated by the large difference between the cases shown in Fig. 2.13. In addition, the survey covers a large fraction $f = 0.81$ of the sky up to large z and therefore vast volumes, so the variance of the density field inside each bin σ_s^2 becomes small very

⁵<http://www.mpe.mpg.de/eROSITA>

⁶<https://act.princeton.edu/>

⁷<https://pole.uchicago.edu/>

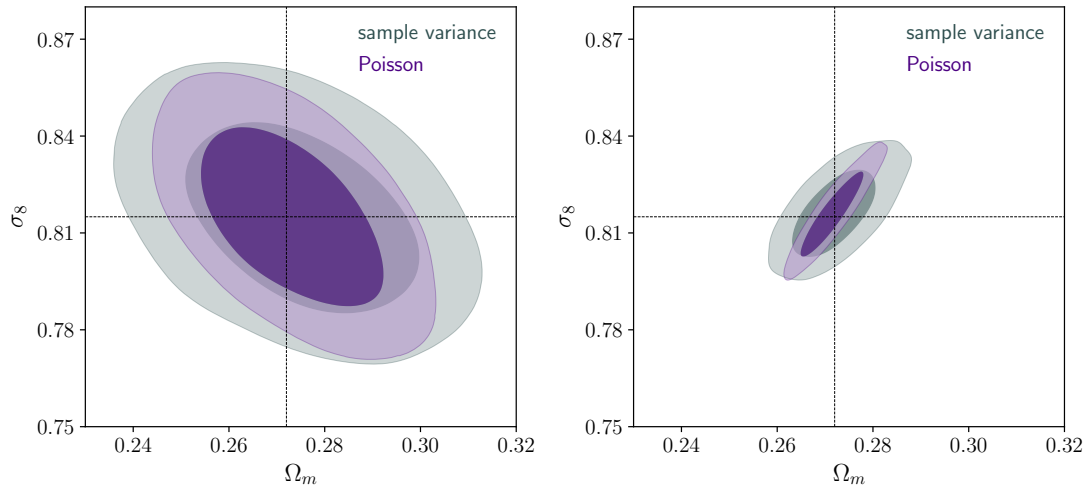


FIGURE 2.14: **Left:** Expected constraints from CORE cluster number counts varying all cosmological and nuisance parameters for either a Poisson likelihood with non-correlated bins (purple) or including sample variance and correlation in the likelihood (grey). **Right:** Same comparison within the constrained parameter space varying only Ω_m , σ_8 and $(1 - b_M)$. When systematic uncertainty in the scaling relations is smaller, the statistical contribution to the error budget becomes more important.

quickly for higher redshifts, as we discussed in Sec. 2.2.2 – the bins are so large that it becomes increasingly unlikely that they deviate from the mean density of the universe. But contrary to Planck, these high- z bins contain the large majority of objects, and consequently a large part of the statistical constraining power. For the constrained case (right) the influence of systematic uncertainties is small, and the relative importance of the statistical error is more significant, leading to a doubling of the posterior width due to sample variance corrections.

To summarize, in the pessimistic case of only assuming current knowledge about the scaling relation, the CORE cluster constraints are limited by these systematic uncertainties and the modified likelihood is only a minor correction. But if the scaling relations are better determined by external probes, the statistical contribution to the error budget becomes subsequently more important.

The late-time evolution of the large-scale structure is sensitive to the growth function, and therefore can be used to probe the effective dark energy equation of state parametrised as $w = w_0 + w_a(1 - a)$. In Fig. 2.15 we show the expected posteriors for w_0 and w_a obtained from the primary CORE CMB and the SZ cluster sample. Since the CMB and cluster degeneracy directions in this plane are almost orthogonal, the SZ sample is an excellent complementary probe. Constraints from the cluster abundance are mainly driven by the evolution of the sample, so knowledge of the redshift scaling $E^\beta(z)$ of the $\bar{Y}_{500} - M$ relation is crucial since it can mimic the behaviour of a time-evolving dark energy component. The overall amplitude of cluster number counts however is not very relevant for the dark energy constraints, therefore uncertainty in the mass bias plays only a minor role as long as it does not evolve with redshift.

While CORE is not designed to be primarily a dark energy survey, the combination of high precision CMB measurements providing information about the early universe and sensitivity to the large-scale structure evolution at late times through cluster abundance and CMB lensing gives a huge lever arm in redshift and allows it to

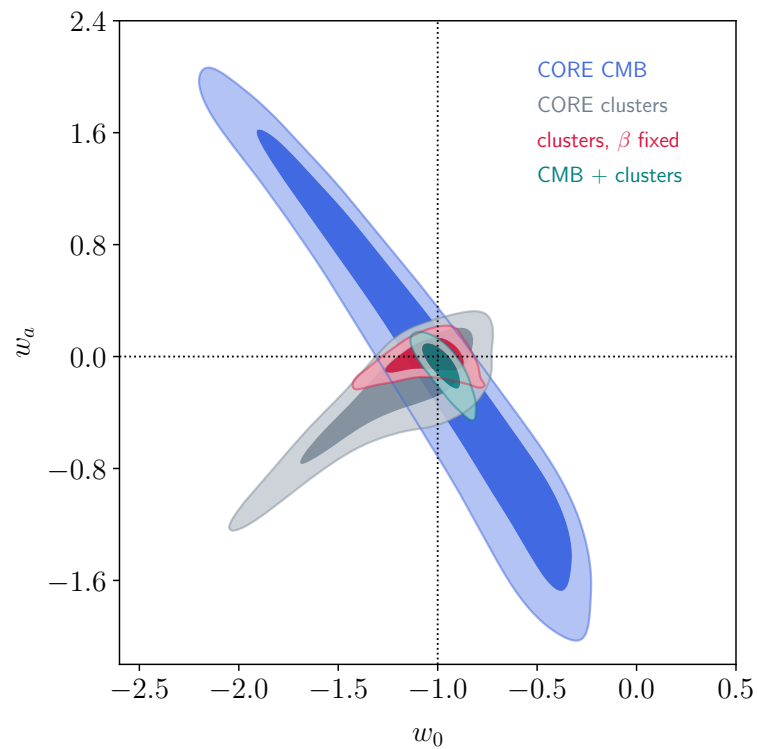


FIGURE 2.15: Expected constraints on the dark energy equation of state w_0 and its time evolution w_a from the primary CORE CMB and the CORE SZ cluster abundance. The main degeneracies are almost orthogonal, so a joint analysis yields large improvements. The cluster constraints are primarily driven by the redshift evolution of the abundance, therefore the slope β of the scaling relation has a large effect on the resulting limits.

TABLE 2.2: CORE constraints on the equation of state compared to the Stage IV dark energy large-scale structure surveys LSST (Ivezic et al., 2008) and Euclid (Amendola et al., 2012).

Survey	$\sigma(w_0)$	$\sigma(w_a)$
LSST	0.05	0.15
Euclid	0.015	0.15
CORE clusters	0.28	0.31
CORE CMB + SZ	0.05	0.1

be competitive with other experiments that try to constrain the dark energy equation of state, such as LSST and Euclid. It is difficult to compare our forecasts exploring the full non-Gaussian shape of the likelihood with Fisher predictions made for the other experiments on equal footing, so we derive an effective parameter width $\sigma(w)$ from our posterior $p(w)$ by calculating

$$\int_{\mu_w - \sigma_w}^{\mu_w + \sigma_w} p(w) dw = 0.68, \quad (2.54)$$

the symmetric range around the best-fit value μ_w containing 68% of the posterior volume. The results are presented in Tab. 2.2 and we note that CORE is not only competitive, but even gives the tightest constraints on the time evolution parameter $\sigma(w_a)$, despite assuming the default case with conservative priors on the cluster scaling parameters.

2.4 Conclusion

The abundance of galaxy clusters is an excellent probe of the growth of cosmological structures. SZ selected samples provide several appealing features: a direct physical connection of the detected Compton y -amplitude to the underlying gravitational potential, a nearly flat selection function at high redshifts and the subsequent possibility to extend cluster catalogues to large z . This allows future surveys to probe the evolution of structure growth over a considerable fraction of the age of the universe as demonstrated with the CORE forecasts in Sec. 2.3.

Clusters can also be detected in the galaxy distribution itself (e.g. Rozo et al., 2010) using the number of member galaxies as a mass proxy, or by their X-ray emission (see e.g. Ebeling et al., 1998; Vikhlinin et al., 2009; von der Linden et al., 2014). But no matter how the samples are selected, the resulting constraints are dominated by the uncertainty in relating the observable to the underlying halo mass. This makes the different approaches complementary: both X-ray and SZ surveys require a calibration of the mass bias usually acquired through weak lensing measurements on at least a subset of the sample, and they require optical surveys to determine the redshift of the clusters. Purely optical surveys on the other hand suffer from the fact that richness is a very noisy tracer of the underlying halo mass consisting mostly of dark matter.

The cosmological constraints derived from the currently largest SZ selected sample detected by Planck discussed in Sec. 2.2 suffer from exactly this problem. Independent mass bias measurements from weak lensing observations exist, but they are in conflict with each other and can either lead to a tension with the cosmology independently derived from the CMB, or not – it entirely rests on the determination of the cluster

mass scale. However it should be noted that the very low value of $(1 - b_M)$ required by the CMB is surprising given our current understanding of cluster astrophysics.

We also pointed out that as the density of detected clusters becomes higher and higher, one can start to see correlations in their abundance. This has consequences for the likelihood used to infer cosmological parameters, and we demonstrated how to incorporate the imprint of the large-scale modes of the density field onto the structure of the cluster distribution. This leads primarily to an increase of the statistical error analogous to cosmic variance effects, but the covariance can also introduce shifts in the posterior parameter distribution. The cluster density for current surveys starts to reach a level for which the modifications are noticeable. For the future there is a trade-off: large cosmological volumes suppress the sample variance term, but there is more information to be gained by dividing the samples in fine redshift bins to get a detailed view on the evolution of cosmic structures. An optimal scheme for cluster science still has to be developed.

However, since the limiting factor is currently not statistics, future cluster surveys will not primarily help to move cluster cosmology forward by detecting more objects, but by providing better measurements of the mass-observable relations. Especially the large optical surveys such as DES, LSST and Euclid allow precise weak lensing measurements to determine the cluster mass scale. But as we demonstrated with the CORE sample, even with only a rough estimate of the cluster mass we can get excellent complementary information to the CMB, and the redshift evolution of the sample alone can provide tight constraints on some parameters such as a time evolving dark energy component.

The next big challenge is therefore less a mere increase in area covered and number of objects detected, but a combination of all available information to make a statistical connection between the set of observables and the underlying halo mass. Massive clusters are exponentially rare objects, so we do not need to detect many of them to get competitive constraints.

Combining all the available information can be taken a step further: the next generation of experiments such as LSST and Euclid will map a major fraction of the sky, and provide measurements of various tracers of the density field such as the cosmic shear power spectrum $P_{\kappa\kappa}$ and galaxy distribution P_{gg} . More can then be learned from cross-correlations between individual probes since they each suffer from different systematic and observational errors, but all trace the same underlying density (Nicola, Refregier, and Amara, 2016). The abundance of clusters complements these other two-point statistics very well because they add information about the non-Gaussian high-density tail of the matter distribution. In other words, the cluster abundance $\propto e^{-\delta_c^2/2\sigma^2}$ is a non-perturbative probe of the density variance σ^2 and therefore contains information about the full hierarchy of density N -point correlation functions not captured by any other cosmological probe.

Chapter 3

Structure growth in parametrised modified gravity

One problem cosmologists face today is that there is no real theoretical contender for the cosmological standard model, Λ CDM. The framework is at the same time impressively successful and disappointing: it reproduces observations throughout cosmic history, but the components that make up $\approx 96\%$ of the universe's energy budget, dark matter and a cosmological constant Λ , are closer to a parametrisation of ignorance than to fundamental physical theory. We have neither detected particle dark matter (even though evidence for its existence is overwhelming) nor do we understand the lack of an enormous vacuum energy term.

There is for sure no shortage of other cosmological theories, but none seem to be theoretically well motivated and able to solve the underlying problems of the standard paradigm.

Λ CDM is a framework and not a specific theory, and observations have to be checked within the (at least) six-parameter model that this framework implies. However, in many cases models can prove flexible enough to provide a good fit to the data even though they are wrong (see Sec. 4.4.3 in the next chapter for an example).

Since the space of alternative theories is enormous, going through all of them one by one is a tedious task. Instead, we want to be able to test (or constrain) whole classes of models, or to check for deviations from the standard model in ways as model-independent as possible. One example is the popular parametrisation of the dark energy equation of state (Chevallier and Polarski, 2001; Linder, 2003)

$$w(a) = w_0 + w_a(1 - a), \quad (3.1)$$

which does not correspond to a physical theory of dark energy, but serves as a way to detect any deviation from the standard expansion history, as could for example be caused by a slowly evolving scalar field as discussed in Sec. 1.1.2. Firmly establishing $w_0 \neq -1$ would be a clear detection of physics beyond Λ CDM, even though we do not necessarily know what the true theory looks like. We can therefore think of these effective parametrisations as *trigger* signals. Note that establishing the trigger is a very difficult task, as usually both Λ CDM and w CDM can fit the data to a degree, and the question becomes which model fits *better*.

Since the background expansion itself is well constrained today (Planck Collaboration et al., 2016a), we want to go one step further and find a way to check for deviations in the linear growth of perturbations on the background. In order to do that, we first deal with general metric perturbations in a FLRW universe in Sec. 3.1, before presenting a way to parametrise deviations from GR in terms of the growth function applicable to the large-scale structure in Sec. 3.2. This simplified approach has several shortcomings when applied to the early universe, and we solve them in

Sec. 3.3 to derive general expressions for parametrised modifications of the Einstein equations valid at all times. In Sec. 3.4 we discuss $f(R)$ gravity as an example how this parametrisation can capture a theory of modified gravity.

3.1 Relativistic perturbations

Before we can address the growth of structures, we have to set the scene. In this section we will not assume any specific theory of gravity, but we will take for granted that the central object is the metric tensor $g_{\mu\nu}$ and its perturbations, which also will make it necessary to discuss the issue of gauge. Note that the Einstein equations or any possible modifications only enter once we want to connect the metric with the energy-momentum tensor later on. The presentation here is based on the excellent review by Ma and Bertschinger, 1995 and notes by Daniel Baumann¹.

3.1.1 Metric decomposition

We want to focus on deviations in the perturbations while assuming the standard background, so we start from the most general perturbed FLRW metric defined by the line element (Bardeen, 1980)

$$ds^2 = a^2(\tau) \left(-(1 + 2A)d\tau^2 + 2B_i dx^i d\tau - (\delta_{ij} + h_{ij}) dx^i dx^j \right), \quad (3.2)$$

where we switched to conformal time defined by $d\tau \equiv dt/a$ and assume all perturbations to be small. This form has 10 degrees of freedom in total: one for the scalar A , three for the vector B_i , and the tensor h_{ij} has six components because any perturbation to the metric has to be symmetric $h_{ij} = h_{ji}$. Using the Helmholtz decomposition, we can write B_i as a superposition

$$\mathbf{B} = \underbrace{\mathbf{B}^{\parallel}}_{\equiv \nabla B} + \mathbf{B}^{\perp}, \quad (3.3)$$

with the divergence-free field $\nabla \cdot \mathbf{B}^{\perp} = 0$ and a curl-free part $\nabla \times \mathbf{B}^{\parallel} = 0$ generated from a scalar potential B . In Fourier space, these correspond to the component perpendicular and parallel to the wave vector respectively, and consequently \mathbf{B}^{\perp} only has two independent components. In a similar fashion, the tensor h_{ij} can be written as

$$h_{ij} = 2C\delta_{ij} + 2 \left(\partial_i \partial_j - \frac{1}{3} \delta_{ij} \nabla^2 \right) E + \left(\partial_i E_j^{\perp} + \partial_j E_i^{\perp} \right) + 2E_{ij}^{\perp}, \quad (3.4)$$

where again all perpendicular quantities have vanishing divergence $\partial^i E_i^{\perp} = 0$, $\partial^i E_{ij}^{\perp} = 0$ and the remaining tensor is trace-free. After reorganising the perturbations in this way, we are left with:

- Four scalars: A, B, C, E
- Four components of two divergence-free vectors: $\mathbf{B}^{\perp}, \mathbf{E}^{\perp}$
- Two components of a trace-free, divergenceless tensor E_{ij}^{\perp}

The big advantage of this restructuring is that the perturbations decouple to linear order in the Einstein equations so they can be solved separately. Vector perturbations decay quickly on an expanding background (Ma and Bertschinger, 1995) and

¹available at <http://www.damtp.cam.ac.uk/user/db275/>

can therefore be neglected. The two tensor degrees of freedom correspond to the two possible polarizations of gravitational waves and for the following discussion they are not relevant. Thus we will focus on the remaining scalar modes only. But first, we have to address the distinction between physical degrees of freedom and gauge modes which only reflect a particular choice of the coordinate system.

3.1.2 Gauge freedom

Physical theories are usually defined on some coordinate system that appears natural for the theory, for example flat Minkowski space for quantum field theory. Even though any relativistic physical theory has to be invariant under coordinate transformations, general relativity makes the issue more complicated: the metric implying a natural coordinate system is itself a solution to the field equations – there is no prior spacetime. This requires great care when choosing particular coordinates to formulate the equations to distinguish mere coordinate effects from real physical quantities.

In an homogeneous and isotropic universe, there is no ambiguity and the FLRW-form of the metric uniquely defines a coordinate system – the frame in which the universe obeys the symmetry assumptions. This is not true any more once we allow for perturbations on the smooth background. There is an infinite choice of valid coordinate systems corresponding to different time-slicings to the perturbations. This is what we refer to as gauge freedom in general relativity. To illustrate the effect, we start from a general coordinate transformation

$$x^\mu \rightarrow \tilde{x}^\mu = x^\mu + \zeta^\mu(\tau, \mathbf{x}), \quad (3.5)$$

where we shift the original coordinate frame by a 4-vector ζ^μ . We only require $\zeta^\mu \ll 1$ for every component to ensure that the perturbations remain small compared to the background. Even in a perfectly homogeneous universe, this then leads to

$$\rho(\tau) \rightarrow \rho(\tau + \zeta^0(\tau, \mathbf{x})) \approx \bar{\rho} + \frac{\partial \bar{\rho}}{\partial \tau} \zeta^0, \quad (3.6)$$

therefore we introduced a density perturbation which is purely an artefact of our time slicing. The reverse is also possible, we can pick a coordinate frame of equal density at every point in time even in an universe with real perturbations. These examples emphasizes the need to keep gauge effects apart from physical quantities. To do this, we make use of the invariance of the line element under the coordinate transformations defined in Eq. 3.5 to get

$$ds^2 = g_{\mu\nu} dx^\mu dx^\nu = \tilde{g}_{\alpha\beta} d\tilde{x}^\alpha d\tilde{x}^\beta, \quad (3.7)$$

which implies that the metric itself transforms as

$$g_{\mu\nu}(x) = \frac{\partial \tilde{x}^\alpha}{\partial x^\mu} \frac{\partial \tilde{x}^\beta}{\partial x^\nu} \tilde{g}_{\alpha\beta}(\tilde{x}). \quad (3.8)$$

We then abbreviate $\zeta^0 \equiv T$ and decompose the spatial part of the shift field ζ^μ as we did before

$$\boldsymbol{\zeta} = \nabla S + \mathbf{S}^\perp, \quad (3.9)$$

to work out the transformation explicitly for the perturbed metric 3.2. The time-time part reads

$$g_{00}(x) = \frac{\partial \tilde{x}^\alpha}{\partial \tau} \frac{\partial \tilde{x}^\beta}{\partial \tau} \tilde{g}_{\alpha\beta}(\tilde{x}) \quad (3.10)$$

$$\approx \left(\frac{\partial \tilde{\tau}}{\partial \tau} \right)^2 \tilde{g}_{00}(\tilde{x}), \quad (3.11)$$

and we made use of the fact that both the perturbations and the components of ζ^μ are small, so we drop any second-order contributions. The only remaining term is then $\alpha = \beta = 0$. Plugging in the metric components, we get

$$-a^2(\tau)(1 + 2A) = -a^2(\tau + T)(1 + T')^2(1 + 2\tilde{A}) \quad (3.12)$$

$$\approx - (a(\tau) + a'T)^2 (1 + 2T')(1 + 2\tilde{A}) \quad (3.13)$$

$$\approx -a^2(\tau)(1 + 2\mathcal{H}T + 2T' + 2\tilde{A}), \quad (3.14)$$

where we denote derivatives with respect to τ with primes and introduced the Hubble function in conformal time, $\mathcal{H} \equiv a'/a$. For small shifts, the perturbation A therefore transforms as

$$\tilde{A} = A - T' - \mathcal{H}T. \quad (3.15)$$

Applying the same procedure to all scalar perturbations, we find the transformation rules

$$A \rightarrow A - T' - \mathcal{H}T, \quad (3.16)$$

$$B \rightarrow B + T - S', \quad (3.17)$$

$$C \rightarrow C - \mathcal{H}T - \frac{1}{3}\nabla^2 S, \quad (3.18)$$

$$E \rightarrow E - S. \quad (3.19)$$

Scalar perturbations are hence invariant under shifts caused by the divergence free component \mathbf{S}^\perp . We then have two scalar gauge fields T and S remaining, which leaves $4 - 2 = 2$ physical degrees of freedom.

The transformation rules allow us to define the two gauge-invariant perturbations (Bardeen, 1980)

$$\Psi \equiv A + \mathcal{H}(B - E') + (B - E')', \quad (3.20)$$

$$\Phi \equiv -C - \mathcal{H}(B - E') + \frac{1}{3}\nabla^2 E, \quad (3.21)$$

which always correspond to physical degrees of freedom of the metric. The alternative is to choose a coordinate frame and therefore fix the gauge, for example using T and S to eliminate two of the scalar perturbations. We use this freedom to set the off-diagonal contributions to zero

$$B = E = 0 \quad (3.22)$$

and therefore arrive at the metric in *Newtonian gauge*

$$ds^2 = a^2(\tau) \left(- (1 + 2\psi)d\tau^2 + (1 - 2\phi)dx^2 \right). \quad (3.23)$$

with the two potentials $A = \psi$ and $C = -\phi$ which are directly connected to the invariant Bardeen variables. We can then compare the form with the perturbed weak-field Minkowski limit of GR and identify ψ with the potential of Newtonian gravity. Unless stated otherwise, this is the gauge we will adopt from now on.

3.2 Parametrised growth equation

In the late universe after emission of the CMB, scales relevant for the large-scale structure today are well within the horizon and structure formation is governed by the Newtonian potential ψ , which obeys the Poisson equation. After relativistic particles are no longer an important contribution to the energy-momentum tensor, as we will see in Sec. 3.3 the Einstein equations also require $\phi = \psi$. Both conditions are well valid when the universe becomes matter dominated at $z \gtrsim 100$. Between then and today, the overwhelming part of linear structure formation takes place. To test deviations from these predictions by standard gravity, we therefore modify the relations (Zhao et al., 2009)

$$\nabla^2 \psi = 4\pi G \mu \bar{\rho} \delta \quad (3.24)$$

$$\frac{\phi}{\psi} = \gamma, \quad (3.25)$$

with two effective parameters μ and γ . For $\mu = \gamma = 1$, we recover the standard behaviour. Many (but not all) modified gravity theories can then be mapped to the expressions above with a specific form $\mu(k, a)$ and $\gamma(k, a)$ which are in general time- and scale-dependent functions. But even without assuming a specific theory, we can test if structures grow faster ($\mu > 1$) or slower ($\mu < 1$) than expected in Λ CDM. The modified Poisson equation together with continuity- and Euler equations translates directly to the growth equation for density perturbations 1.75 as derived in Sec. 1.2.3

$$\ddot{\delta} + 2H\dot{\delta} = 4\pi G \mu \bar{\rho} \delta, \quad (3.26)$$

where μ leads to a modification of the source term. The change in the other potential can be probed by lensing, since the gravitational deflection angle α is susceptible to the total projected metric perturbation (Bartelmann, 2010)

$$\alpha = - \int_0^{\chi_s} d\chi \frac{\chi_s - \chi}{\chi_s} \nabla(\psi + \phi), \quad (3.27)$$

along the line of sight χ for a source at χ_s . Gravitational lensing is therefore a probe of $(\psi + \phi) \propto \psi \mu (1 + \gamma)$, while the growth of structures probes $\psi \propto \mu$. Combining both of them can then give constraints on a difference between the two potentials (Joudaki et al., 2017).

Note that a constant μ is clearly not a feasible physical theory, because it causes an effective rescaling of the gravitational constant G and thus would predict gravity to be different in the solar system as well. The modification should therefore just be considered as an effective description on linear scales that has to be replaced at some level. The same is true for high redshifts: the growth of anisotropies observed in the CMB is well constrained, so only small deviations are possible. Viable modified gravity theories achieve this by screening mechanisms, $\mu, \gamma \rightarrow 1$ in high density regions and in the early universe, as will be discussed in Sec. 3.4.

We therefore restrict the applicability of the parametrisation to later times and numerically solve the growth equation Eq. 3.26 starting at $z_{\text{ini}} = 100$, which is usually

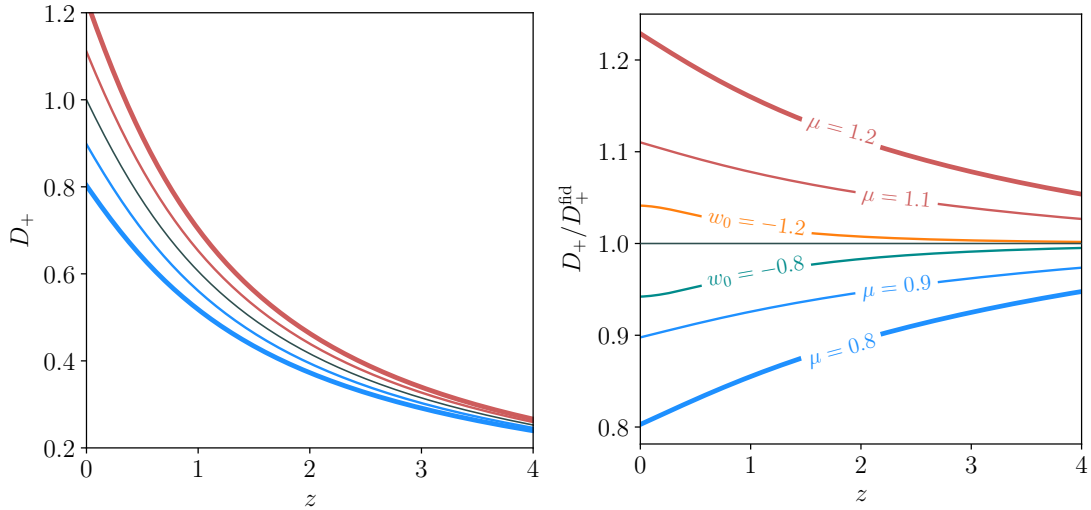


FIGURE 3.1: **Left:** Numerical solutions $D_+(z, \mu)$ of the growth equation starting from $z = 100$ for constant $\mu = 0.8, 0.9$ (blue) and $1.1, 1.2$ (red) compared to the fiducial solution (black) **Right:** Relative change of the growth function due the constant $\mu \neq 1$. At $z = 0$ the relative changes $\delta\mu/\mu$ roughly correspond to the resulting changes in the linear growth function $\delta D_+/D_+$. For comparison, we also show the effect of the dark energy equation of state w_0 on the linear growth.

also used as a starting point for cosmological N -body simulations. We need initial conditions to fix the time evolution, and since the universe is matter dominated at these early times we set $D_+(a_{\text{ini}}) = a_{\text{ini}}$, thus assuming the standard GR behaviour to begin with. Examples for the resulting linear growth function $D_+(z, \mu)$ are shown in Fig. 3.1 (left) for $\mu = 0.8, 0.9$ (blue) and $1.1, 1.2$ (red). For comparison, we also show the relative effect of changing the equation of state parameter w_0 (right), which affects linear growth via the background drag term $\propto H(w)\dot{\delta}$ and the changed evolution of the mean matter density $\rho_m(a(w))$.

This approach works fine for purposes of structure formation, i.e. the modelling of the linear matter power spectrum via

$$P(k, z) = D_+^2(z, z_{\text{ini}}, \mu) P(k, z_{\text{ini}}), \quad (3.28)$$

with the initial power spectrum computed at $z_{\text{ini}} \approx 100$ which we assume to follow a standard form. However, if we want to include information from the CMB and understand the shape of $P(k, z_{\text{ini}})$, we have to go beyond this simple picture.

3.3 Parametrised Einstein equations

At early times, scales forming the large-scale structure today were comparable to the size of the horizon, and the simplified Newtonian treatment outlined above breaks down. We therefore have to translate the μ, γ parametrisation into a fully relativistic setting. To do this, we start from the linearly perturbed Einstein equations

$$\delta G_{\mu\nu} = 8\pi G \delta T_{\mu\nu}, \quad (3.29)$$

before finding the proper self-consistent modifications that reduce to Eqs. 3.24 and 3.25 in the non-relativistic limit. For now however, we deal only with standard GR.

The only energy-momentum tensor compatible with the symmetry assumptions of the FLRW metric is that of a perfect fluid of the form

$$T_{\nu}^{\mu} = (\bar{\rho} + \bar{p})u^{\mu}u_{\nu} + \bar{p}\delta_{\nu}^{\mu}, \quad (3.30)$$

with the mean density $\bar{\rho}$, the pressure \bar{p} and the four-velocity $u_{\mu} = a\delta_{\mu}^0$ of a comoving observer. The perturbations are then to linear order

$$\delta T_0^0 = -\delta\rho, \quad (3.31)$$

$$\delta T_0^i = (\bar{\rho} + \bar{p})v^i, \quad (3.32)$$

$$\delta T_j^i = \delta P\delta_j^i + \Pi_j^i, \quad (3.33)$$

with the velocity v^i , the anisotropic stress tensor Π_j^i and we can absorb its trace into redefining the pressure and always set $\Pi_i^i = 0$. It is helpful to define the (scalar) anisotropic stress potential σ

$$\sigma \equiv (\partial_i\partial_j + \frac{1}{3}\delta_{ij})\Pi_j^i, \quad (3.34)$$

and the velocity potential v via

$$v_i \equiv \partial_i v, \quad (3.35)$$

since vorticity in the velocity field is only generated by vector perturbations at first order, and therefore the curl contribution to v_i vanishes. The energy-momentum tensor is again gauge-dependant and all quantities have to be evaluated in the Newtonian frame fixed by Eq. 3.22. It is also possible (and sometimes convenient) to use the available gauge freedom to set certain perturbations of T_{ν}^{μ} to zero, but this has to be done at the cost of more degrees of freedom in the metric.

Now we can start to gather the available equations of motion. The Bianchi identities ensure *local* energy-momentum conservation

$$\nabla_{\mu}T_{\nu}^{\mu} = \partial_{\mu}T_{\nu}^{\mu} + \Gamma_{\mu\alpha}^{\mu}T_{\nu}^{\alpha} - \Gamma_{\mu\nu}^{\alpha}T_{\alpha}^{\mu} = 0, \quad (3.36)$$

and we insert the perturbed metric 3.2 to calculate the connection coefficients

$$\Gamma_{\alpha\beta}^{\mu} = \frac{g^{\mu\sigma}}{2} (\partial_{\beta}g_{\sigma\alpha} + \partial_{\alpha}g_{\sigma\beta} - \partial_{\sigma}g_{\alpha\beta}). \quad (3.37)$$

We then project the relation 3.36 onto the 4-velocity, $u^{\nu}\nabla_{\mu}T_{\nu}^{\mu} = 0$, to arrive at the generalisation of the continuity equation

$$\delta' + \left(1 + \frac{\bar{p}}{\bar{\rho}}\right) (\nabla \cdot \mathbf{v} - 3\phi') + 3\mathcal{H} \left(\frac{\delta P}{\delta\rho} - \frac{\bar{p}}{\bar{\rho}}\right) \delta = 0, \quad (3.38)$$

where we define the overdensity $\delta \equiv (\rho - \bar{\rho})/\bar{\rho}$. The perpendicular component ($u^{\nu}u_{\alpha} - g_{\alpha}^{\nu}$) $\nabla_{\mu}T_{\nu}^{\mu} = 0$ leads to the Euler equation

$$\mathbf{v}' + \mathcal{H}\mathbf{v} - 3\mathcal{H}\frac{\bar{p}'}{\bar{\rho}'}\mathbf{v} = -\frac{\nabla\delta P}{\bar{\rho} + \bar{p}} - \nabla\psi, \quad (3.39)$$

on a perturbed FLRW background. The perturbed connection also allows us to calculate the Ricci tensor $R_{\mu\nu}$

$$R_{\mu\nu} = \partial_\alpha \Gamma_{\mu\nu}^\alpha - \partial_\nu \Gamma_{\alpha\mu}^\alpha + \Gamma_{\alpha\beta}^\alpha \Gamma_{\mu\nu}^\beta + \Gamma_{\beta\mu}^\alpha \Gamma_{\alpha\nu}^\beta, \quad (3.40)$$

to derive the linearised Einstein equations. A lengthy calculation then leads to the trace-free component

$$\nabla^2(\phi - \psi) = -8\pi G a^2 \sigma, \quad (3.41)$$

where we have anisotropic stress $\sigma \neq 0$ only if particles have different macroscopic velocities at a single point, i.e. large velocity dispersions or crossing streams. The only species with non-negligible velocity dispersions are neutrinos, and they cease to contribute to the energy budget after neutrinos decouple in the early universe. Thus the Einstein equations predict $\phi = \psi$ except in the early universe. The remaining independent equations are the time-time component

$$\nabla^2\phi - 3\mathcal{H}(\phi' + \mathcal{H}\psi) = 4\pi G a^2 \bar{\rho}\delta, \quad (3.42)$$

the time-space part $0i$

$$\phi' + \mathcal{H}\psi = -4\pi G a^2 (\bar{\rho} + \bar{p})v, \quad (3.43)$$

and the trace

$$\phi'' + \mathcal{H}(\psi' + 2\phi') + (2\mathcal{H}' - \mathcal{H}^2)\psi = 4\pi G a^2 \delta P. \quad (3.44)$$

Inserting the $0i$ equation 3.43 into the 00 component 3.42, we get the general relativistic form of the Poisson equation

$$\nabla^2\phi = 4\pi G a^2 (\bar{\rho}\delta - 3\mathcal{H}(\bar{\rho} + \bar{p})v) \quad (3.45)$$

$$= 4\pi G a^2 \bar{\rho}\Delta, \quad (3.46)$$

where we defined the gauge-invariant density perturbation Δ as a source (Bardeen, 1980)

$$\bar{\rho}\Delta \equiv \delta\rho + \bar{\rho}'v. \quad (3.47)$$

For any component in thermal equilibrium, we also have the equations of state

$$\delta P = w\delta\rho, \quad \sigma = 0, \quad (3.48)$$

given by the sound speed $w = c_s^2$ with $w = 1/3$ for relativistic particles (photons and neutrinos) and $w \approx 0$ for dark matter and baryons. If the different species are interacting or out of equilibrium, we have to replace the equations of state with the generalised phase-space conservation expressed by the Boltzmann equation (Ma and Bertschinger, 1995), which couples the pressure perturbation and the anisotropic stress to the density and velocity potential.

Counting the degrees of freedom, we have the two metric perturbations (ψ, ϕ) and four perturbations to the energy-momentum tensor $(\delta, \delta P, v, \sigma)$. The Bianchi identities give us two constraints, continuity- and Euler equation, and we have two equations of state for fluids (or equivalently the Boltzmann hierarchy to establish two relations among the perturbation variables), and a total of four independent Einstein equations at linear order, resulting in eight constraints overall. This forms a redundant, but

consistent system of equations.

Before we modify the equations of motions in any way, it is worth to pause and think about what to preserve:

- The local conservation of T^{μ}_{ν} is not only ensured by the Bianchi identities, but also by Noether's theorem. As long as we assume that the modification of gravity is caused by *any* Lagrangian $\mathcal{L}(\zeta, \partial^{\mu}\zeta\partial_{\mu}\zeta)$ that only depends on *any* field ζ and its derivatives and not explicitly on the coordinate x^{μ} , the tensor T^{μ}_{ν} is the corresponding conserved Noether current and Eqs. 3.38 and 3.39 will still hold.
- The relations between the energy-momentum perturbations either expressed via equations of state or the Boltzmann hierarchy follow from kinetic theory on a given background defined by the metric. While new physics can certainly lead to new scattering terms in the Boltzmann equation (for example decaying dark matter), these modifications are quite far from the parametrisation we started with in Eqs. 3.24 and 3.25. The Boltzmann equation itself is a consequence of phase space conservation expressed by Liouville's theorem and holds for any system obeying Hamiltonian dynamics.

Consequently, we have to keep the four resulting equations, which leaves us free to choose two among the Einstein equations. In our effective parametrisation, they should be generalisations of the non-relativistic parametrisation 3.24 and 3.25.

First we note that the relativistic Poisson equation 3.45 contains the spatial metric perturbation ϕ , but the dynamics of non-relativistic matter is only governed by the temporal perturbation ψ . Therefore we use Eq. 3.41 to find

$$\nabla^2\psi = 4\pi Ga^2(\bar{\rho}\Delta - 2\sigma), \quad (3.49)$$

which captures the modification of the Poisson equation we started with, after we modify it as

$$\nabla^2\psi = 4\pi Ga^2\mu(k, a)(\bar{\rho}\Delta - 2\sigma), \quad (3.50)$$

so we see that both the density perturbation and the anisotropic stress have to be scaled by μ . Thus, the relativistic version of Eq. 3.25 follows from the trace-free part of the Einstein equation 3.41 as (Hojjati, Pogosian, and Zhao, 2011)

$$\nabla^2(\phi - \gamma(k, a)\psi) = -8\pi Ga^2\mu(k, a)\sigma, \quad (3.51)$$

which reduces to the desired non-relativistic limit. These two equations close the system and allow us to evolve the density perturbations in a self-consistent way if the functions $\mu(k, a)$ and $\gamma(k, a)$ are specified. This can either happen in a full theory of modified gravity that allows to derive a specific form (as we will see in Sec. 3.4) or in a parametric way.

We then implement the modified Equations 3.50 and 3.51 into the public Einstein-Boltzmann code CLASS² (Blas, Lesgourgues, and Tram, 2011) to solve the coupled system of equations. We do explicitly have to assume $\mu, \gamma \approx 1$ at times before the CMB decouples, because significant deviations of order 1 from standard gravity break various numerical schemes to solve the Boltzmann hierarchy for the interacting species in the early universe. In application to data this is not a serious limitation, because the physics of the CMB is tightly constrained today (e.g. by Planck Collaboration et al., 2016a).

²<http://class-code.net/>

3.4 $f(R)$ gravity

To apply the parametrisation to an example, we take a specific $f(R)$ modified gravity theory. It is generated by adding a function of the Ricci scalar R to the gravitational Lagrangian (hence the name). As we will see, the theory can support an expansion history matching observations, but makes additional predictions deviating from GR for the growth of perturbations. We start from the modified Einstein-Hilbert action

$$S = \int dx^4 \sqrt{-g} \left(\frac{R + f(R)}{16\pi G} + \mathcal{L}_m \right), \quad (3.52)$$

with the Lagrangian of the matter fields \mathcal{L}_m . We adopt the functional form proposed by Hu and Sawicki, 2007

$$f(R) = -2\Lambda \frac{R}{R + m^2}, \quad (3.53)$$

with a constant Λ and the curvature scale m^2 . Note that $f(R) \rightarrow 0$ for $R \rightarrow 0$, so in that sense the model does not contain a cosmological constant. For $m^2 \ll R$, the function can be expanded to get

$$f(R) \approx -2\Lambda - f_{R0} \frac{\bar{R}_0^2}{R}, \quad (3.54)$$

where \bar{R}_0 is the Ricci scalar today, overbars denote background quantities and we introduced the dimensionless parameter $f_{R0} \equiv -2\Lambda m^2 / \bar{R}_0^2$. To recover the well-measured Λ CDM expansion history, we fix the first term to the cosmological constant in GR $\Lambda = \Lambda_{\text{GR}}$ and $f_{R0} \ll 1$ is the only remaining free parameter of the model. This implies that the theory can support an accelerated expansion, and background quantities are indistinguishable from Λ CDM.

This is reminiscent of the discussion about scalar fields in Sec. 1.1.2, where we had to tune the potential of the field to recover the current H_0 . Something very similar is happening here, and apart from the measured effective value of Λ , there is no fundamental reason to assume the form Eq. 3.54. However, adding new terms to the Einstein-Hilbert action has also other phenomenological consequences beyond the background dynamics.

To see this, we obtain the modified Einstein equations by variation of Eq. 3.52 with respect to the metric $g_{\mu\nu}$

$$G_{\mu\nu} - f_R R_{\mu\nu} - \left(\frac{f}{2} - \square f_R \right) g_{\mu\nu} - \nabla_\mu \nabla_\nu f_R = 8\pi G T_{\mu\nu}, \quad (3.55)$$

with the new scalar degree of freedom $f_R \equiv df/dR$. This equation contains higher than second derivatives of the metric in the f_R terms, and therefore breaks the assumptions leading to Lovelock's theorem discussed in Sec. 1.1.1. However, $f(R)$ theories with algebraic functions f are the *only* way prevent the dynamical instability from higher derivative terms as long as the gravitational action is constructed from the metric alone (Woodard, 2007).

The trace of Eq. 3.55 leads to an equation of motion for the scalar field f_R

$$\nabla^2 \delta f_R = \frac{a^2}{3} (\delta R(f_R) - 8\pi G \delta \rho_m), \quad (3.56)$$

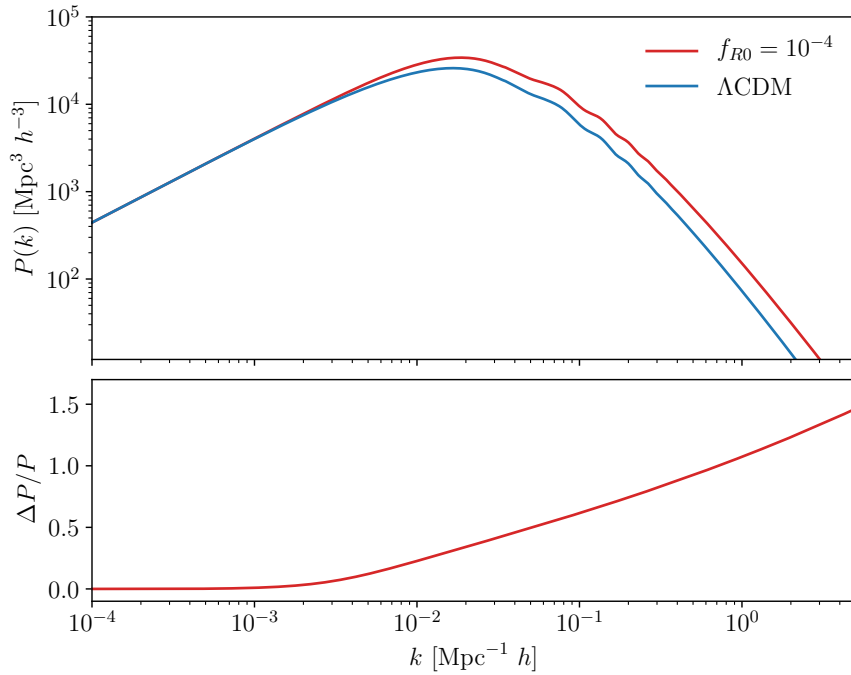


FIGURE 3.2: Linear matter power spectrum at $z = 0$ calculated using the modified Einstein equations for $f_{R0} = 10^{-4}$. Large scales exceeding the Compton wavelength of the f_R field $k < a\lambda$ evolve as in Λ CDM. On smaller scales, the additional gravitational force boosts the power spectrum.

where we adopted the quasi-static approximation and again consider small perturbations on a smooth background, i.e. the quantities $\delta x \equiv x - \bar{x}$. The time-time component of the modified Einstein equations gives a Poisson-like equation for the scalar metric perturbation $2\psi = \delta g_{00}/g_{00}$

$$\nabla^2 \psi = \frac{16\pi G}{3} a^2 \rho_m - \frac{a^2}{6} \delta R(f_R), \quad (3.57)$$

which can still be identified with the Newtonian potential but has contributions from both the matter density ρ_m and the scalar field via $\delta R(f_R)$. Eqs. 3.56 and 3.57 are non-linear and thus we will later resort to N -body simulations to solve them in general, but two limiting cases are insightful:

For large field values $|f_{R0}| \gg |\psi|$, we can linearise

$$\delta R \simeq \left. \frac{dR}{df_R} \right|_{R=\bar{R}} \delta f_R, \quad (3.58)$$

and the Fourier-space solution of Eqs. 3.56 and 3.57 becomes

$$k^2 \psi(k) = -4\pi G \left(\frac{4}{3} - \frac{1}{3} \frac{\lambda^2 a^2}{k^2 + \lambda^2 a^2} \right) a^2 \delta \rho_m(k), \quad (3.59)$$

with the Compton wavelength of the scalar field $\lambda^{-1} = (3df_R/dR)^{1/2}$, which corresponds to the range of the additional force. On small scales $k > a\lambda$, we arrive at a Poisson equation with an extra factor $4/3$. For scales larger than the Compton wavelength, the additional contribution vanishes, and we recover the same behaviour as in general relativity. Translated to the parametrisation discussed in Sec. 3.3, the function

$\mu(k, a)$ thus becomes

$$\mu(k, a) \equiv \frac{4}{3} - \frac{1}{3} \frac{\lambda^2 a^2}{k^2 + \lambda^2 a^2}, \quad (3.60)$$

and from the trace-free part of Eq. 3.55 we can derive in similar fashion (Hojjati et al., 2016)

$$\gamma(k, a) = \frac{1 - \mu(k, a)}{1 + \mu(k, a)}, \quad (3.61)$$

which allows this particular $f(R)$ theory to be mapped onto the parametrised Einstein equations 3.50 and 3.51 in the large field limit. We show an example for the linear matter power spectrum for $f_{R0} = 10^{-4}$ calculated by our modified CLASS code in Fig. 3.2. The additional gravitational force leads to faster growth on scales within the interaction range set by λ^{-1} .

In the opposite limit of small field values $|f_{R0}| \ll |\psi|$, the two contributions in Eq. 3.56 approximately cancel, therefore

$$\delta R \approx 8\pi G \delta \rho_m, \quad (3.62)$$

and Eq. 3.57 turns into the usual Poisson equation. This is the *screened regime*.

To estimate where the transition occurs, we can formally solve Eq. 3.56 using the Greens's function of the Laplacian

$$\delta f_R(r) = \frac{1}{4\pi r} \frac{1}{3} \int_0^r d^3 \mathbf{r}' 8\pi G \left(\delta \rho_m - \frac{\delta R}{8\pi G} \right) \quad (3.63)$$

$$= \frac{2}{3} \frac{GM_{\text{eff}}(r)}{r}, \quad (3.64)$$

with an effective mass M_{eff} as the source for field fluctuations δf_R (Schmidt, 2010). Note that $M_{\text{eff}}(r) \leq M(r)$ and equality holds in the unscreened regime where we get $\delta f_R = \frac{2}{3} \psi_N$ with the Newtonian potential of a spherical overdensity $\psi_N = GM/r$. Because the fluctuation in f_R is by definition smaller than its background value $\delta f_R \leq \bar{f}_R$, this translates to

$$|f_R| \leq \frac{2}{3} \psi_N(r), \quad (3.65)$$

thus the additional force is only sourced by mass outside of the radius where this condition is met.

In Fig. 3.3 we show an example of the CMB temperature anisotropy spectrum C_ℓ^{TT} calculated for $f_{R0} = 10^{-4}$. In this case any change in the primary CMB is negligible and so deviations are only introduced via secondary effects that perturb the radiation on the way to the observer. Photons follow geodesics $ds^2 = 0$, which is equivalently expressed by the geodesic equation

$$\frac{d^2 x^\nu}{ds^2} = -\Gamma_{\alpha\beta}^\nu \frac{dx^\alpha}{ds} \frac{dx^\beta}{ds}, \quad (3.66)$$

where s is an affine parameter increasing along the path. The spatial component $\nu = i$ gives rise to gravitational lensing 3.27, which we neglected for this comparison since we already know that the late-time lensing potential $\propto \nabla(\psi + \psi)$ differs. The remaining secondary contribution shown in Fig. 3.3 (bottom) is caused by the time component $\nu = 0$ that gives rise to the integrated Sachs-Wolfe effect (Sachs and Wolfe, 1967)

$$\frac{\Delta T}{T_{\text{CMB}}} = - \int d\chi (\psi' + \phi'), \quad (3.67)$$

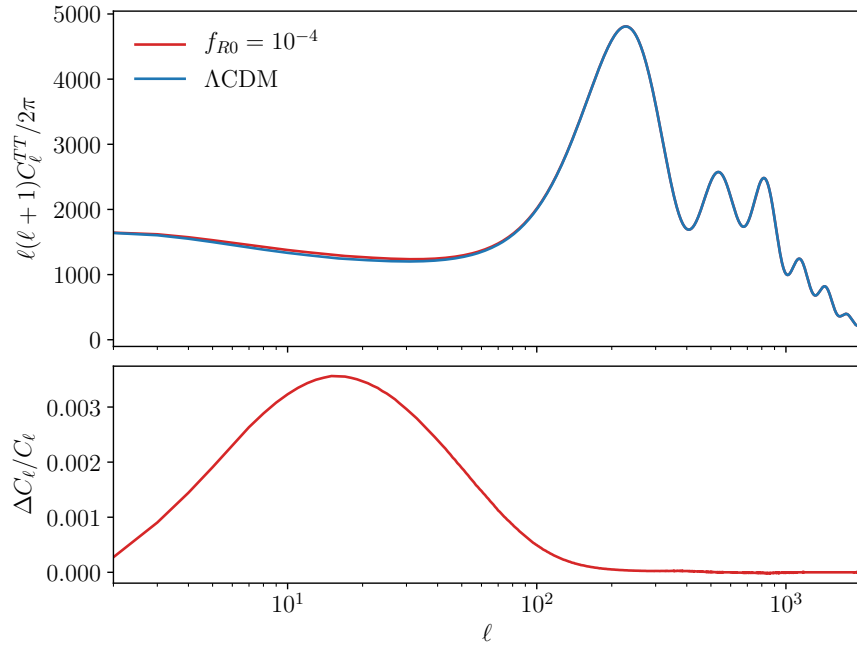


FIGURE 3.3: Angular temperature power spectrum C_ℓ^{TT} of the CMB calculated using the modified Einstein equations for $f_{R0} = 10^{-4}$. At times relevant for the primary CMB, the theory behaves like Λ CDM. The only difference is caused by the integrated Sachs-Wolfe effect at late times, leading to a small boost of anisotropies on large scales. Lensing is not included, but would lead to a damping of the peaks due to the higher amplitude of matter fluctuations in the late universe.

and leads to a small boost in the temperature anisotropy as soon as $f(R)$ effects start to become noticeable and change the time evolution of the potentials. This also occurs in Λ CDM when the cosmological constant dominates the energy budget and potentials start to decay. As we can see from Fig. 3.3

$$\left. \frac{\Delta T}{T_{\text{CMB}}} \right|_{f(R)} > \left. \frac{\Delta T}{T_{\text{CMB}}} \right|_{\Lambda\text{CDM}}, \quad (3.68)$$

so contrary to naive expectations, large-scale potentials decay faster at late times in $f(R)$ than in Λ CDM, even though the growth of density perturbations is boosted due to the fifth force.

To summarise, the theory is identical to Λ CDM on the background level, but perturbatively yields a maximum enhancement of gravity by $1/3$ on scales smaller than the Compton wavelength λ^{-1} . It also includes a screening mechanism that restores GR in regions of high density and its onset is given by the typical depth of cosmological potential wells $\psi \sim 10^{-5} \dots 10^{-6}$, so that $|f_{R0}| \sim 10^{-5} \dots 10^{-6}$ is the relevant parameter space where this mechanism can function. Values of f_{R0} below this threshold are always screened, and therefore phenomenologically uninteresting.

3.5 Conclusion

A lot of effort has been made to map the *expansion history* of the universe in terms of the Hubble function $H(z)$ and check for consistency with the expected evolution of a

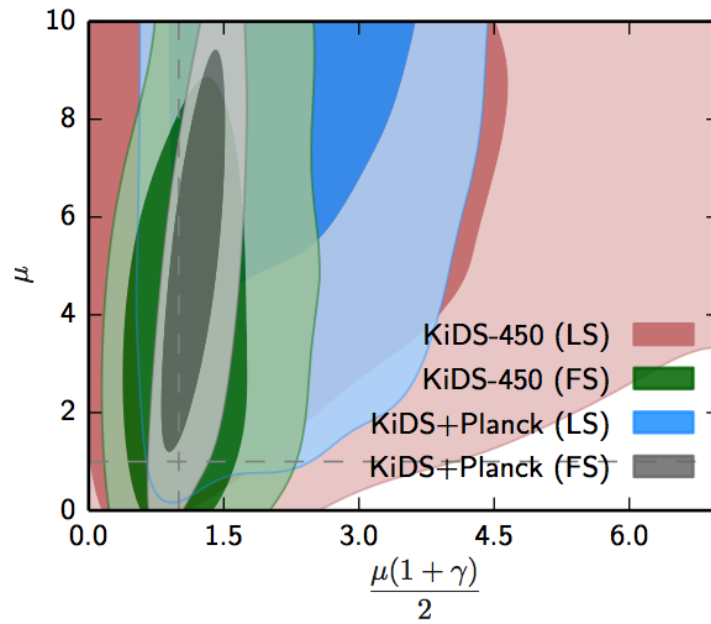


FIGURE 3.4: Constraints on the constant μ, γ parameters in the growth function Eq. 3.26 from the KiDS survey. The analysis is based on the angular lensing shear power spectrum and uses either all fiducial scales (FS) used in the main analysis or only large scales (LS) roughly corresponding to $k > 0.05 \text{ Mpc}^{-1}h$. Lensing only probes the combination $\mu(1 + \gamma)$ and is not sensitive to potentials individually. Plot from Joudaki et al., 2017

Λ CDM universe. By now, the background is tightly constrained by various measurements (Astier et al., 2006; Alam et al., 2017; Planck Collaboration et al., 2016a) even though tensions between different measurements of the normalisation H_0 currently remain (Riess et al., 2016).

The next logical step is to move to linear perturbations and check for consistency in the *growth* of structures. In the same way as deviations from the Hubble function are parametrised by the effective equation of state formalism w_0, w_a in lack of an appealing theory of dark energy, we can probe the evolution of density perturbations characterised by a set of simple parameters μ, γ . Hopefully the parametrisation can then capture any deviation we might expect in a real theory. The approach using the late-time growth function presented in Sec. 3.2 can be used to calculate linear large-scale structure observables rather easily.

However, the most powerful data set available to cosmology today comes from the CMB. Combining it with late time data with the simplified growth function approach however leads to inconsistency: even if the parametrisation is assumed to revert to GR at high redshifts, secondary effects such as lensing and the integrated Sachs-Wolfe effect on the temperature anisotropy have to be taken into account.

For modelling the CMB itself, dynamics on scales comparable to the horizon become important and the Newtonian theory breaks down. We derived a fully relativistic framework in Sec. 3.3 that extends the late-time μ, γ parametrisation to all redshifts and makes it possible to calculate CMB observables once the functional form $\mu(k, a)$ and $\gamma(k, a)$ is specified.

The limitation to strictly linear theory however limits the approach considerably.

While it is appealing to be free of a specific model, most of the information in the large-scale structure actually is contained in mildly non-linear scales. This is demonstrated by results from the lensing shear power spectrum measured by the Kilo Degree Survey (KiDS) in Fig. 3.4 (Joudaki et al., 2017). Lensing alone can only constrain $\mu(1 + \gamma)$ via Eq. 3.27, but restricting the analysis to linear scales gives very weak limits on the parameter. The situation is slightly improved when Planck CMB information is added to constrain the remaining cosmological parameters, but the analysis is based on the growth function approach in Eq. 3.26 and does not consistently model the CMB according to a relativistic generalisation of the parametrisation. As a practical matter, it is very difficult to keep a measurement of structure growth limited to purely linear scales. Lensing observables are angular shear correlation functions $\xi(\theta)$ on the sky, and they receive contributions from a wide range of k -modes in the density field. Other measurements trace luminous matter such as galaxies instead of the (mostly dark) matter fluctuations, and need assumptions for the biasing to extract cosmological information.

In the non-linear regime, any viable modified gravity theory requires a screening mechanism to restore GR in the solar system. Therefore continuing the functions $\mu(k, a)$ and $\gamma(k, a)$ to smaller scales requires assuming a specific theory in order to model screening effects. The screening phenomenology differs between theories, so we are again faced with the task of testing models individually. However, as long as we assume that a modified gravity theory reproduces the well-measured Λ CDM background, we can make some generic predictions: Any physically distinct modification to the Einstein-Hilbert action in Eq. 3.52 adds additional degrees of freedom. Because gravity couples universally to the energy-momentum tensor $T_{\mu\nu}$, these new degrees of freedom generically lead to attractive fifth forces as in the case of $f(R)$ that we discussed in Sec. 3.4. Consequently, modifications of gravity generically predict $\mu \gtrsim 1$, even though there is no inherent scale to the enhancement. It has to be evaluated from case to case.

If we want to test a specific modified gravity theory, the large-scale structure is the most promising place to look for deviations from GR. Any viable theory of modified gravity have to be screened in the solar system, where gravity is well measured. Models that achieve this by suppressing the additional degree of freedom in high-density regions such as $f(R)$ also automatically also revert to the GR limit at high redshifts when the mean density was high. So while the physics of the early universe leading to BBN and CMB is tightly constrained by highly accurate measurements, this does not necessarily translate into tight bounds on various modifications of GR such as $f(R)$ or other models that introduce additional scalar fields like Galileon, Symmetron or Dilaton gravity (Hojjati et al., 2016).

Chapter 4

Halo Mass Function for $f(R)$ Gravity and Massive Neutrinos

As we have seen in the previous chapter, the possibility to constrain modified gravity purely in the linear regime is quite limited with current data. Due to the practical problems associated with an analysis that is constrained to large scales only, it is not clear if the situation will improve drastically. Most cosmological measurements of structure growth are somewhat contaminated by non-linearities.

Instead of shying away from the non-linear regime, we therefore embrace it and develop a model for the halo mass function in $f(R)$ cosmologies. We work in a generalised spherical collapse framework, and the crucial parameter of interest turns out to be the critical collapse threshold $\delta_c(f_{R0})$ in modified gravity. Following the discussion in Sec. 3.4, we expect that the force enhancement will cause a boost in the cluster abundance that can be used to constrain deviations from GR. Then it becomes important to account for *known unknowns*: all constraints on $f(R)$ from the mass function so far have been obtained within a one-parameter extension of Λ CDM.

However, we know that neutrinos in our universe behave like a hot dark matter component and dampen the growth of structures. This counteracts the signature enhancement we are looking for in a modified gravity theory. Since the neutrino mass scale is still unknown, we have to take the resulting uncertainty associated with the damping effect into account when we constrain deviations from GR. The interplay and degeneracy between these two effects is the main motivation for the work presented here. We restrict ourselves to simulations and survey forecasts for now, but an application of the resulting joint mass function to data is currently ongoing.

This chapter is based on work in collaboration with Matteo Costanzi, Jochen Weller and Marco Baldi, who was responsible for running various N -body simulations we used to calibrate our model. It has been published in Hagstotz et al., 2018.

4.1 Introduction

One of the goals in modern cosmology is to understand the underlying dynamics and statistics of the cosmic density field. Clusters of galaxies trace the highest of its peaks, and theory predicts their abundance to depend exponentially on the amplitude of the matter power spectrum (Press and Schechter, 1974; Bond et al., 1991; Sheth and Tormen, 2002) which turns them into a formidable probe of cosmological parameters (Allen, Evrard, and Mantz, 2011; Kravtsov and Borgani, 2012).

Studying the cosmic density field is especially of interest because it might reveal the mechanism for the observed accelerated expansion of the Universe. It can either be explained by introducing a smooth dark energy component to the universe's energy budget, or by modifying gravity itself. Both scenarios can potentially be tested via

their imprint on the abundance of clusters (Battye and Weller, 2003; Mohr et al., 2003), but in this paper we will focus on the latter.

Because general relativity (GR) is the unique theory of gravity in $1 + 3$ dimensions under very general assumptions (Lovelock, 1972), any modifications introduce new physical degrees of freedom. While these can give rise to accelerated expansion, they also tend to enhance gravity at the perturbative level. One example discussed in this paper are the $f(R)$ scalar-tensor theories, which generalise the Einstein-Hilbert action by adding a non-linear function of the Ricci scalar R .

The enhancement of gravity tends to result in an increased abundance of clusters, and several approaches to model the halo mass function in modified gravity exist (Kopp et al., 2013; Cataneo et al., 2016; von Braun-Bates et al., 2017). But all of these studies were performed within a one-parameter extension of the minimal Λ CDM standard model, and a natural extension is the inclusion of massive neutrinos which form a small, but unknown fraction of cosmological dark matter. The detection of a non-zero neutrino mass is firmly established by particle physics as a consequence of neutrino flavour oscillations (Araki et al., 2005) and in cosmology the neutrino background can be measured in both the cosmic microwave background (Sellentin and Durrer, 2015) and the large scale structure (Baumann et al., 2018). Even though the mass scale is still uncertain, neutrinos lead to a suppression of structure growth below their free-streaming scale (Lesgourgues and Pastor, 2006). This then leads to the question: Can neutrinos mask modified gravity effects in the large scale structure? Are constraints obtained on $f(R)$ theories from cluster number counts (Schmidt, Vikhlinin, and Hu, 2009; Lombriser et al., 2012; Cataneo et al., 2015) then still valid when including massive neutrinos into the analysis? And on a more fundamental level, how can the joint effects of neutrinos and modified gravity be included in the theoretical prediction of cluster abundance?

Early investigations of these issues have been presented by Baldi et al. (2014), who performed the first N -body simulations of $f(R)$ gravity in the presence of massive neutrinos, clearly demonstrating a strong degeneracy between their effects on the abundance of gravitationally bound systems. More recently, Giocoli, Baldi, and Moscardini (2018) and Peel et al. (2018) explored the same degeneracies based on a combination of cluster counts and weak lensing statistics along the past light cone. In this work, we continue investigating the combined effects of $f(R)$ and massive neutrinos by developing a theoretical model of the joint halo mass function, calibrated to a suite of specifically designed N -body simulations.

We start with a brief summary of $f(R)$ gravity in Sec. 3.4 and present the simulation suite used to explore joint effects of modified gravity and neutrinos in Sec. 4.2. In Sec. 4.3 we introduce the joint mass function and apply our framework to forecast the ability of current and future surveys to constrain $f(R)$ theories in Sec. 4.4. We summarise our results in Sec. 4.6.

4.2 The DUSTGRAIN-*pathfinder* simulations

For our analysis we make use of the halo catalogues extracted from the DUSTGRAIN-*pathfinder* simulations (see Giocoli, Baldi, and Moscardini, 2018, for a detailed description), a suite of cosmological N -body simulations designed to investigate the possible observational degeneracies between $f(R)$ gravity and massive neutrinos by sampling their joint parameter space. The simulations have a periodic box size of $750 \text{ Mpc}/h$ per side filled with 768^3 dark matter particles of mass $m_{\text{cdm}}^p = 8.1 \times 10^{10} M_{\odot}/h$ (for the case of $m_{\nu} = 0$) and with as many neutrino particles (for the case of $m_{\nu} > 0$). The

Name	Gravity	$ f_{R0} $	$\sum m_\nu$ [eV]	Ω_{cdm}	$m_{\text{cdm}}^p [M_\odot/h]$	$m_\nu^p [M_\odot/h]$
Λ CDM	GR	–	–	0.31345	8.1×10^{10}	–
fR4	$f(R)$	10^{-4}	–	0.31345	8.1×10^{10}	–
fR5	$f(R)$	10^{-5}	–	0.31345	8.1×10^{10}	–
fR6	$f(R)$	10^{-6}	–	0.31345	8.1×10^{10}	–
fR4-0.3eV	$f(R)$	10^{-4}	0.3	0.30630	7.92×10^{10}	1.85×10^9
fR5-0.15eV	$f(R)$	10^{-5}	0.15	0.30987	8.01×10^{10}	9.25×10^8
fR5-0.1eV	$f(R)$	10^{-5}	0.1	0.31107	8.04×10^{10}	6.16×10^8
fR6-0.1eV	$f(R)$	10^{-6}	0.1	0.31107	8.04×10^{10}	6.16×10^8
fR6-0.06eV	$f(R)$	10^{-6}	0.06	0.31202	8.07×10^{10}	3.7×10^8

TABLE 4.1: The subset of the DUSTGRAIN-*pathfinder* simulations considered in this work with their specific parameters.

particles are moving under the effect of an $f(R)$ gravitational interaction mediated by the scalar potential ψ satisfying Eq. 3.57.

The DUSTGRAIN-*pathfinder* runs have been performed with the MG-Gadget code (Puchwein, Baldi, and Springel, 2013) – a modified version of the GADGET code (Springel, 2005) for $f(R)$ gravity theories – combined with the particle-based implementation of massive neutrinos developed by Viel, Haehnelt, and Springel (2010), and already employed in Baldi et al. (2014). The MG-Gadget $f(R)$ solver has been thoroughly tested (see e.g. Winther et al., 2015) and already used for several applications in cosmology ranging from pure collisionless simulations (Baldi and Villaescusa-Navarro, 2018; Arnold et al., 2018) to hydrodynamical simulations (Arnold, Puchwein, and Springel, 2015; Roncarelli, Baldi, and Villaescusa-Navarro, 2018), to zoomed simulations of Milky Way-sized objects (Arnold, Springel, and Puchwein, 2016; Naik et al., 2018).

Initial conditions have been produced by generating two separate but fully correlated random realisations of the linear density power spectrum for CDM and massive neutrino particles as computed by the Einstein-Boltzmann code CAMB (Lewis, Challinor, and Lasenby, 2000) at the starting redshift of the simulation $z_i = 99$. Following the approach of e.g. Zennaro et al. (2017) and Villaescusa-Navarro et al. (2017), neutrino gravitational velocities are calculated based on the scale-dependent growth rate $D(z_i, k)$ for the neutrino component. On top of these, neutrino particles also receive an additional thermal velocity extracted from the neutrino momentum distribution for each value of neutrino mass under consideration.

In the present work – which is the third in a series of papers making use of the DUSTGRAIN-*pathfinder* simulations after Giocoli, Baldi, and Moscardini (2018) and Peel et al. (2018) – we restrict our focus on a subset of the full simulations suite consisting of nine runs whose parameters are summarised in Table 4.1. All simulations share the same standard cosmological parameters which are set in accordance with the Planck 2015 constraints (Planck Collaboration et al., 2016a), namely $\Omega_m = \Omega_{\text{cdm}} + \Omega_b + \Omega_\nu = 0.31345$, $\Omega_b = 0.0481$, $\Omega_\Lambda = 0.68655$, $H_0 = 67.31 \text{ km s}^{-1} \text{ Mpc}^{-1}$, $\mathcal{A}_s = 2.199 \times 10^{-9}$, $n_s = 0.9658$.

For all simulations we have identified collapsed CDM structures in each comoving snapshot by means of a Friends-of-Friends algorithm (FoF hereafter, see Davis et al., 1985) on the CDM particles with linking length $\lambda = 0.16 \times d$ where d is the mean inter-particle separation, retaining only structures with more than 32 particles. On top of such FoF catalogue we have run the SUBFIND algorithm (Springel et al., 2001)

to identify gravitationally bound structures and to associate standard quantities such as the mass and the radius to the main substructure of each FoF group. The latter quantities are computed in the usual way by growing spheres of radius R around the most-bound particle of each main substructure enclosing a total mass M until the condition

$$\frac{4}{3}\pi R_{200m}^3 \times 200 \times \Omega_m \rho_{\text{crit}} = M_{200m} \quad (4.1)$$

is fulfilled for $R = R_{200m}$ and $M = M_{200m}$, where $\rho_{\text{crit}} \equiv 3H^2/8\pi G$ is the critical density of the universe.

4.3 Joint mass function

Dark matter halos form from collapsing regions that decouple from the background expansion. Their abundance can be related to the volume fraction of the Gaussian density field δ_R smoothed on a radius R above a critical collapse threshold δ_c (Press and Schechter, 1974). This yields the number density of halos within a mass interval $[M, M + dM]$, the halo mass function:

$$\frac{dn}{dM} = f(\sigma) \frac{\rho_m}{M^2} \frac{d \ln \sigma^{-1}}{d \ln M} \quad (4.2)$$

where $\rho_m = \Omega_m \rho_{\text{crit}}$ is the mean density of the Universe and $f(\sigma)$ is the multiplicity function related to the collapsed volume fraction $F(M)$ occupied by halos over mass M by

$$f(\sigma) = 2\sigma^2 \partial F / \partial \sigma^2. \quad (4.3)$$

It depends on the variance of the linear density field

$$S \equiv \sigma^2(R(M), z) = \int \frac{dk}{k} \frac{k^3 P(k, z)}{2\pi^2} W^2(kR(M)) \quad (4.4)$$

within a filter containing the mass $M = 4/3\pi R^3 \rho_m$. The variables M , R and σ^2 are monotonous functions of each other and can therefore be used interchangeably.

Note that even though σ is often thought of as growing with cosmic time $\sigma(z) = D(z)\sigma_0$, in the framework of spherical collapse it is instructive to consider the threshold $\delta_c(z) = \delta_c/D(z)$ as the dynamical quantity. At early times, the density field is Gaussian and completely characterised by its variance alone. The collapse criterion is then really a criterion imposed on the *initial conditions*.

If we assume a top-hat filter in Fourier space $W = \theta(k - 1/R)$, each new mode of the density field entering the filter is independent and the smoothed field performs a random walk with R (or equivalently S) as a time variable. The problem can then be rephrased: when does a trajectory $\delta(S)$ first cross the threshold δ_c (Bardeen et al., 1986; Bond et al., 1991)?

Under these assumptions individual trajectories follow a Langevin equation

$$\frac{\partial \delta}{\partial S} = \eta(S), \quad (4.5)$$

with a stochastic driving term η defined by its mean $\langle \eta \rangle = 0$ and variance $\langle \eta(S)\eta(S') \rangle = \delta_D(S - S')$. The probability distribution Π of trajectories then evolves according to the

corresponding Fokker-Planck equation

$$\frac{\partial \Pi}{\partial S} = \frac{1}{2} \frac{\partial^2 \Pi}{\partial \delta^2}, \quad (4.6)$$

with the boundary condition $\Pi(\delta, S = 0) = \delta_D(\delta)$ because the Universe is homogeneous on large scales. However, trajectories can cross the barrier more than once leading to double-counting of halos. To solve this, one demands the additional boundary condition (an absorbing barrier) $\Pi(\delta = \delta_c, S) = 0$.

The solution to Eq. 4.6 is then given by (Bond et al., 1991)

$$\Pi(\delta, \sigma^2) = \frac{1}{2\pi\sigma^2} \left(e^{-\delta^2/2\sigma^2} - e^{-(2\delta_c - \delta)^2/2\sigma^2} \right), \quad (4.7)$$

where the second Gaussian term reflects the fact that trajectories end at the barrier. Omitting it lead to the missing normalisation factor 2 of the Press and Schechter, 1974 prediction.

With the boundary condition the distribution function vanishes for $\delta > \delta_c$, so we express $F(S)$ by subtracting the fraction of trajectories that did not yet cross the threshold

$$F(\sigma^2) = 1 - \int_{-\infty}^{\delta_c} \Pi(\delta, \sigma^2) d\delta, \quad (4.8)$$

from which we can derive the multiplicity function $f(\sigma)$ by using Eq. 4.3 to get the mass function by Press and Schechter, 1974

$$f_k(\sigma) = \sqrt{\frac{2}{\pi}} \frac{\delta_c}{\sigma} e^{-\delta_c^2/(2\sigma^2)}, \quad (4.9)$$

with the correct normalisation. Note that we indicate solutions from non-correlated random walks (using a k -space top-hat) with subscript k .

This approach works reasonably well, but has several shortcomings:

1. Collapse in a Gaussian random field does not occur spherically. In the Zel'dovich approximation, the eigenvalues λ_i of the deformation tensor follow the joint probability distribution (Doroshkevich, 1970)

$$p(\lambda_1, \lambda_2, \lambda_3) = \frac{15^3}{8\pi\sqrt{5}\sigma^6} \exp\left(-\frac{3I_1^2}{\sigma^2} + \frac{15I_2}{2\sigma^2}\right) \quad (4.10)$$

$$\times |(\lambda_3 - \lambda_2)(\lambda_3 - \lambda_1)(\lambda_2 - \lambda_1)|, \quad (4.11)$$

with $I_1 = \lambda_1 + \lambda_2 + \lambda_3$ and $I_2 = (\lambda_1\lambda_2 + \lambda_1\lambda_3 + \lambda_2\lambda_3)$. Isotropic collapse with $\lambda_1 = \lambda_2 = \lambda_3$ therefore does not occur. Instead the Zel'dovich picture suggests a collapse into subsequently walls, sheets, filaments and halos, where the last step occurs typically along a filament in an ellipsoidal fashion. This is fully consistent with structure formation observed in N -body simulations.

2. Real halos do not form out of sharp k -space top-hats. Usually one assumes rather a real-space top-hat as initial condition for the spherical collapse. This leads to coupling of Fourier modes and introduces correlations between steps of the random walk.

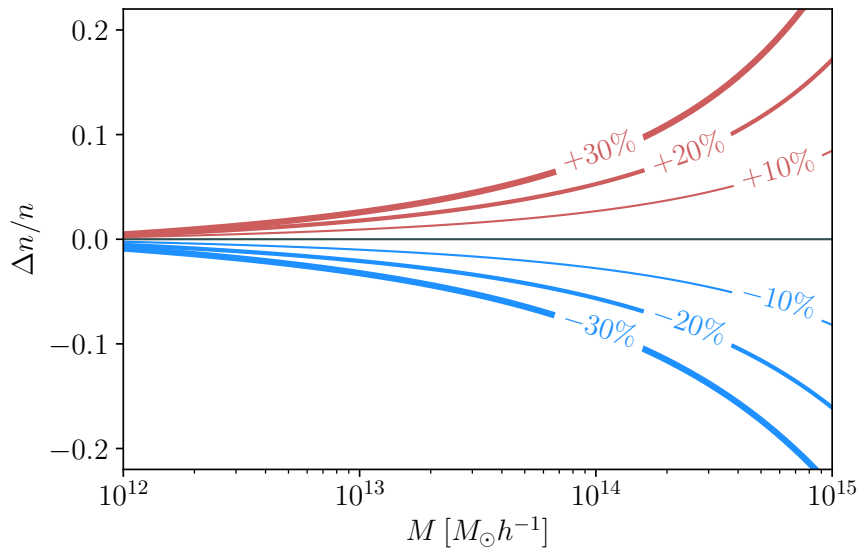


FIGURE 4.1: Effect on the halo mass function when changing the barrier width D_B around the fiducial value $D_B = 0.4$. A broader barrier leads to a smaller suppression of the exponential tail of the mass function and therefore more high-mass objects.

4.3.1 Diffusing, drifting barrier

The non-spherical collapse dynamics can be addressed by modifying the collapse barrier. The main motivation is that low-mass (high σ) halos are more ellipsoidal, while the largest objects are approximately spherical. Ellipsoidal patches collapse later because they have to get rid of angular momentum, which leads to an effective higher threshold. There are various ways to extend the excursion set formalism to account for this, and here we follow Kopp et al., 2013 and introduce a scale-dependent barrier of the form

$$B = \delta_c + \beta S, \quad (4.12)$$

that tends to the spherical collapse threshold δ_c for high-mass halos $\sigma \ll 1$. Even though more general forms for the ellipsoidal collapse barrier B can be found in the literature (e.g. $B = \delta_c + \beta^\gamma S$; see Sheth and Tormen, 2002), the linear approximation adopted in this work is sufficient for typical cluster abundance studies using clusters of mass $M \gtrsim 10^{13.5} M_\odot / h$.

In addition to the barrier drift, the collapse dynamics themselves are complicated by environmental effects and fuzzy halo definitions. In Maggiore and Riotto, 2010b this was taken into account by turning the barrier itself into a Gaussian stochastic variable with a mean $\bar{B} = \delta_c + \beta S$ and width D_B . Both the trajectories and the barrier itself perform a random walk, and the joint probability distribution is obtained from a 2D Fokker-Planck equation (Maggiore and Riotto, 2010b; Corasaniti and Achitouv, 2011)

$$\frac{\partial \Pi}{\partial S} = \frac{1}{2} \frac{\partial^2 \Pi}{\partial \delta^2} + \frac{D_B}{2} \frac{\partial^2 \Pi}{\partial B^2}, \quad (4.13)$$

which is solved by

$$f_k(\sigma) = \sqrt{\frac{2a}{\pi}} \frac{1}{\sigma} e^{-a\bar{B}^2/(2\sigma^2)} \left(\bar{B} - \sigma^2 \frac{d\bar{B}}{d\sigma^2} \right), \quad (4.14)$$

with $a \equiv 1/(1 + D_B)$. Using Eq. 4.12, this reduces to a Press-Schechter like solution with the constant threshold δ_c replaced by the full barrier:

$$f_k(\sigma) = \sqrt{\frac{2a}{\pi}} \frac{\delta_c}{\sigma} e^{-a(\delta_c + \beta\sigma^2)^2/2\sigma^2}. \quad (4.15)$$

The effect of D_B is demonstrated in Fig. 4.1: a broader barrier leads to a smaller factor a in the exponential, boosting the abundance of high-mass clusters because those rare trajectories can cross the threshold easier.

4.3.2 Non-markovian corrections

Accounting for realistic filter functions makes it necessary to consider the deviations from an uncorrelated random walk. Halos form from regions that resemble spherical patches in the initial conditions and several possible window functions to capture the correct form of these proto-halos exist (Bond et al., 1991). Here we assume a real space top-hat, which in Fourier space turns into

$$W(x) = \frac{3j_1(x)}{x}, \quad (4.16)$$

with the spherical Bessel function j_n , which we use from here on to calculate the variance of the density field S in Eq. 4.4. In Maggiore and Riotto, 2010a the authors calculated the corrections induced by correlations between the variance S smoothed at different radii R for this choice of smoothing filter. The general two-point correlation function can be written as

$$\langle \delta_1 \delta_2 \rangle = \min(S_1, S_2) + \Delta(S_1, S_2), \quad (4.17)$$

where we introduced the shorthand $\delta_1 = \delta(R_1)$, and the first term expresses the Markov dynamics leading to the Press-Schechter result with a general barrier in Eq. 4.15. The correction is of the form

$$\Delta(S_1, S_2) = \kappa \frac{S_1(S_2 - S_1)}{S_2} \quad (4.18)$$

with the coefficient

$$\kappa(R) \simeq 0.459 - 0.003R, \quad (4.19)$$

and has a weak dependence on cosmology via the power spectrum. As pointed out above, we deal with a purely Gaussian field in the initial conditions here, and all correlations are introduced by the filter and not by later non-linear mode coupling. This also means that κ should be calculated from the Λ CDM relation in Eq. 4.19 even within a modified gravity model. We will return to this point when discussing the modified gravity mass function.

This leads to the real-space top-hat multiplicity function f_x , to first order in κ (Maggiore and Riotto, 2010a; Kopp et al., 2013),

$$f_x(\sigma) = f_k(\sigma) + f_{1,\beta=0}^{m-m}(\sigma) + f_{\beta^{(1)}}^{m-m}(\sigma) + f_{1,\beta^{(2)}}^{m-m}(\sigma) \quad (4.20)$$

with the Markovian term f_k for a diffusive, drifting barrier given by Eq. 4.15 and corrections

$$f_{1,\beta=0}^{m-m}(\sigma) = a\kappa \frac{\delta_c}{\sigma} \left(e^{a\delta_c^2/2\sigma^2} - \frac{1}{2}\Gamma\left(0, \frac{a\delta_c^2}{2\sigma^2}\right) \right), \quad (4.21)$$

$$f_{\beta^{(1)}}^{m-m}(\sigma) = -a\delta_c\beta \left(a\kappa \operatorname{erfc}\left(\delta_c\sqrt{\frac{a}{2\sigma^2}}\right) + f_{1,\beta=0}^{m-m}(\sigma) \right), \quad (4.22)$$

$$f_{1,\beta^{(2)}}^{m-m}(\sigma) = -a\beta \left(\frac{\beta}{2}\sigma^2 f_{1,\beta=0}^{m-m}(\sigma) + \delta_c f_{1,\beta^{(1)}}^{m-m}(\sigma) \right). \quad (4.23)$$

4.3.3 Spherical collapse in modified gravity

As for the Λ CDM case, the starting point of our analysis is spherical collapse. Kopp et al., 2013 numerically solved the full modified Einstein, scalar field and non-linear fluid equations to obtain δ_c in $f(R)$ gravity, and they parameterised their solution for the threshold by

$$\delta_c^{f(R)}(f_{R0}, M, z) = \delta_c^{\text{GR}}(z) \times \Delta(f_{R0}, M, z) \quad (4.24)$$

where the deviation from GR is captured by the correction factor

$$\begin{aligned} \Delta(f_{R0}, M, z) &= 1 + b_2 (1+z)^{-a_3} \left(m_b - \sqrt{m_b^2 + 1} \right) \\ &\quad + b_3 \left(\tanh(m_b) - 1 \right) \end{aligned} \quad (4.25)$$

$$m_b(f_{R0}, M, z) = (1+z)^{a_3} (\log_{10} M - m_1(1+z)^{-a_4}) \quad (4.26)$$

$$m_1(f_{R0}) = \mu_1 \log_{10} |f_{R0}| + \mu_2$$

$$b_2 = 0.0166$$

$$b_3(f_{R0}) = \beta_3 (2.41 - \log_{10} |f_{R0}|)$$

$$a_3(f_{R0}) = 1 + \exp\left(-2.08 (\log_{10} |f_{R0}| + 5.56)^2\right)$$

$$a_4(f_{R0}) = \alpha_4 \left(\tanh\left(0.69 (\log_{10} |f_{R0}| + 6.65)\right) + 1 \right).$$

The parameterisation converges to the GR limit δ_c^{GR} separately for high z and $|f_{R0}| \rightarrow 0$, which is well approximated by (Nakamura and Suto, 1997)

$$\delta_c^{\text{GR}}(z) = \frac{3(12\pi)^{2/3}}{20} \left(1 - 0.0123 \log_{10} \left(1 + \frac{\Omega_m^{-1} - 1}{(1+z)^3} \right) \right). \quad (4.27)$$

The coefficients $\alpha_4, \beta_3, \mu_1, \mu_2$ from Kopp et al., 2013 are given in Tab. 4.2 which were fitted to numerical solutions and should be regarded as prediction of their spherical collapse model. Here we want to bring this model closer to data before we consider possible constraints from cluster abundance.

TABLE 4.2: Fiducial values for the GR mass function barrier shape and the virial $f(R)$ collapse threshold Eq. 4.24.

GR		$f(R)$			
D_B	β	α_4	β_3	μ_1	μ_2
0.4	0.12	0.11	2.7×10^{-3}	1.99	26.21

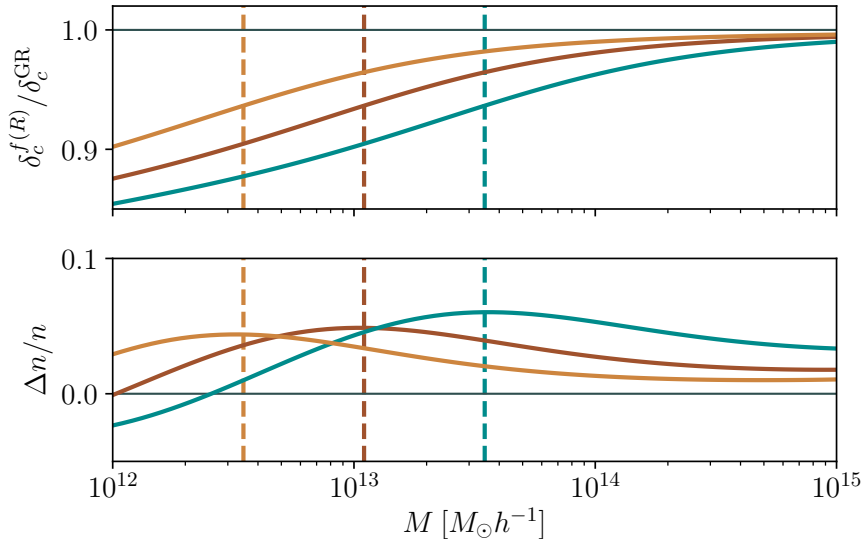


FIGURE 4.2: Top: Relative change in the collapse threshold $\delta_c/\delta_c^{\text{GR}}$ for slightly different values of the screening mass M_{screen} (dashed vertical lines) around $f_{R0} \simeq 10^{-6}$ at $z = 0$. This corresponds to the position of the typical bump in the relative cluster abundance compared to ΛCDM (bottom).

The crucial ingredient of the model is m_b , which sets the transition mass where screening sets in. We will express this scale as the screening mass M_{screen} , defined by $m_b(M_{\text{screen}}) = 0$. In Fig. 4.2 we show the connection between the threshold and the cluster abundance: up to M_{screen} the threshold grows linearly with $\log M$ and afterwards it starts reverting to the fiducial GR value. In the mass function, this scale corresponds to a characteristic peak in the additional relative abundance. Note that the negative relative abundance for lower masses shown in the plot is physical because of mass conservation: additional high-mass objects form from low-mass halos.

For $m_b = 0$, the threshold is given by

$$\delta_c = \delta_c^{\text{GR}} (1 + b_2(1+z)^{-a_3} - b_3), \quad (4.28)$$

and because a lower δ_c leads to a higher cluster abundance, b_2 and b_3 set the height of the additional abundance peak, a_3 and a_4 control the redshift evolution of the screening mass, and μ_1, μ_2 determine how quickly the model reverts to GR when changing f_{R0} .

Fig. 4.3 shows the variation of the threshold as a function of redshift and the f_{R0} parameter for a halo of mass $M_{200} = 10^{14} M_\odot/h$. Considering this mass representative of the lightest objects entering a cosmological cluster catalogue, the leftmost line indicates the limit of cluster abundance studies to constrain the theory at a given redshift where the deviation in δ_c is of order 1%.

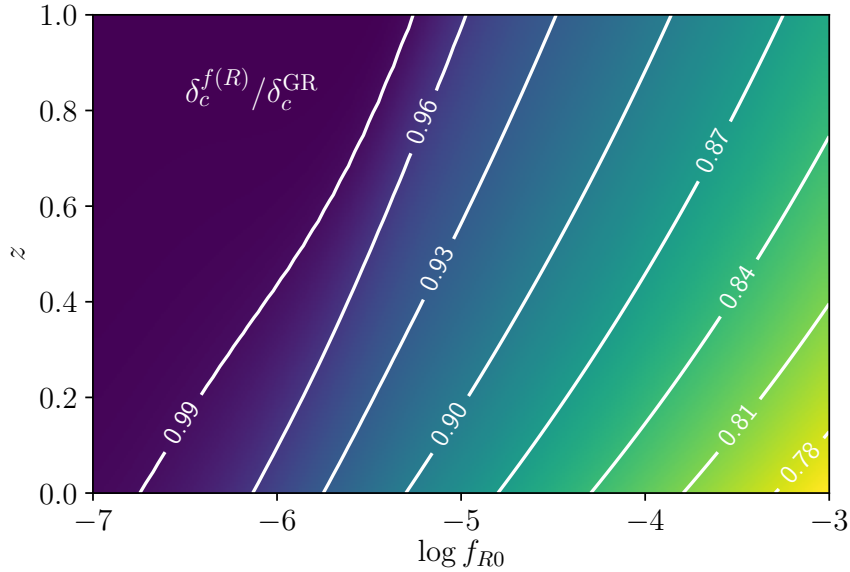


FIGURE 4.3: Change in collapse threshold $\delta_c^{f(R)}/\delta_c^{\text{GR}}$ for a halo of fixed mass $M_{200} = 10^{14}M_{\odot}/h$ with redshift and f_{R0} . The fiducial threshold is lowered due to the fifth force for large f_{R0} . At high redshifts, δ_c reverts to the Λ CDM value. The plot includes the corrections from Sec. 4.3.6.

To write the multiplicity function for $f(R)$ including non-Markovian corrections, we assume that the correlation between steps behaves similar for modified gravity and GR. This is justified because we measure the correlation in the initial conditions where the density fields in both theories are identical – all modifications to the time evolution are absorbed into the threshold $\delta_c(f_{R0}, M, z)$. Therefore we write (Kopp et al., 2013)

$$f_x^{f(R)}(\sigma) \simeq f_x^{\text{GR}}(\sigma) \frac{f_k^{f(R)}}{f_k^{\text{GR}}} \quad (4.29)$$

with the Markovian multiplicity function $f_k^{f(R)}$ derived from the modified gravity barrier $\bar{B} = \delta_c(f_{R0}, M, z) + \beta\sigma^2$ given in eq. 4.24

$$\begin{aligned} f_k^{f(R)}(\sigma) &= \sqrt{\frac{2a}{\pi}} \frac{1}{\sigma} e^{-a\bar{B}^2/(2\sigma^2)} \left(\bar{B} - \sigma^2 \frac{d\bar{B}}{d\sigma^2} \right) \\ &= \sqrt{\frac{2a}{\pi}} \frac{1}{\sigma} e^{-a\bar{B}^2/(2\sigma^2)} \left(\delta_c^{f(R)} - \frac{3M}{2} \frac{\partial \delta_c^{f(R)}}{\partial M} \frac{\partial \ln \sigma}{\partial \ln R} \right). \end{aligned} \quad (4.30)$$

Together with f_k^{GR} (Eq. 4.15) and f_x^{GR} (Eq. 4.20), this defines the full modified gravity multiplicity function (Eq. 4.29), and yields the halo mass function via Eq. 4.2. We emphasize again that all expressions are defined for the smoothed density field σ^{GR} calculated in a *standard cosmology* – as already discussed, the threshold is imposed on the initial conditions, and all subsequent effects of modified gravity are encapsulated in the dynamics of the barrier.

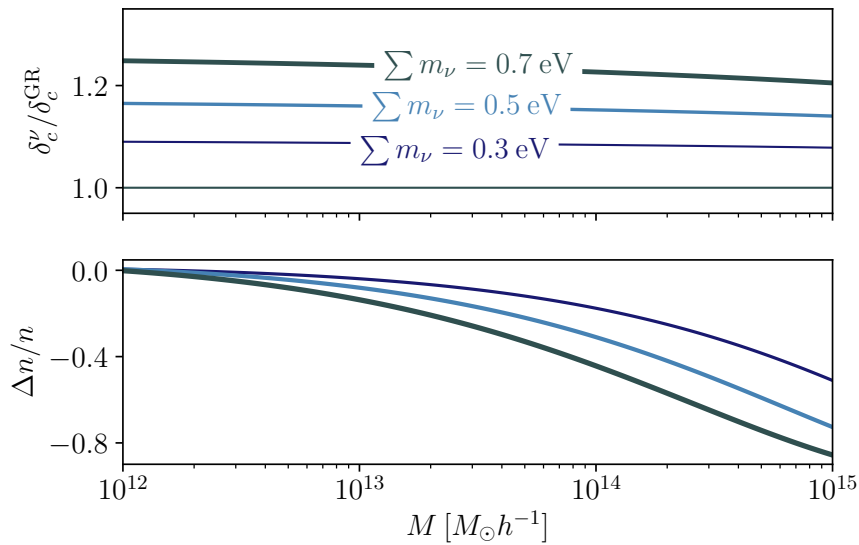


FIGURE 4.4: Top: Change in the collapse threshold δ_c^ν/δ_c for different neutrino masses. The scale dependent growth in ν CDM cosmologies translates to a slight mass dependence of δ_c . The higher threshold leads then to a stronger suppression in the exponential high mass tail of the mass function (bottom).

4.3.4 Neutrinos

As we have seen, the signal of modified gravity is a lower collapse threshold and a resulting higher abundance of clusters compared to Λ CDM. To set realistic limits on deviations from GR, we will now incorporate effects of massive neutrinos. As has been studied before (see e.g. Lesgourgues and Pastor, 2006) they suppress structure growth below the free-streaming scale which leads to a lower abundance of galaxy clusters, counteracting possible effects of $f(R)$. Constraining the neutrino mass is an important goal for cluster cosmology in its own right, but here we will focus on degeneracy with modified gravity effects.

Costanzi et al., 2013 showed that the effect of neutrinos on the cluster abundance can be well captured by rescaling the smoothed density field

$$\sigma^2 \rightarrow \sigma_{\text{cdm}}^2(z) = \int \frac{dk}{k} \frac{k^3 P_{\text{cdm}}(k, z)}{2\pi^2} W^2(kR), \quad (4.31)$$

with the cold dark matter power spectrum obtained by rescaling the total matter power spectrum P_m with the respective transfer functions weighted by the density of each species

$$P_{\text{cdm}}(k, z) = P_m(k, z) \left(\frac{\Omega_{\text{cdm}} T_{\text{cdm}}(k, z) + \Omega_b T_b(k, z)}{T_m(k, z) (\Omega_{\text{cdm}} + \Omega_b)} \right)^2, \quad (4.32)$$

thus assuming that neutrinos are distributed smoothly on cluster scales. The scale dependent growth caused by neutrinos for the other components is also accounted for by the transfer functions. Eq. 4.31 is expressed as a time-dependent rescaling, but we can also again think of the initial density field as fixed and map the change to the collapse threshold

$$\delta_c^\nu = \frac{\sigma(z)}{\sigma_{\text{cdm}}(z)} \delta_c. \quad (4.33)$$

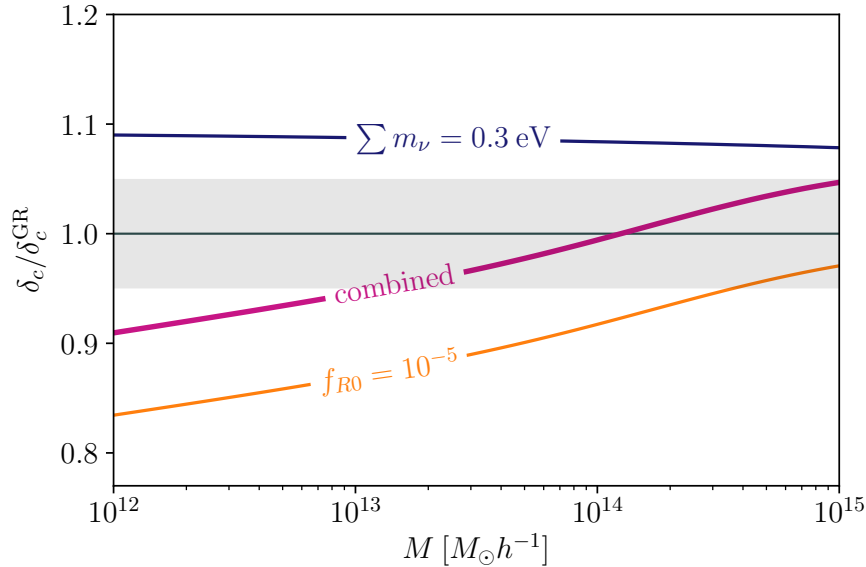


FIGURE 4.5: Change in the effective collapse threshold at $z = 0$ induced by massive neutrinos with $\sum m_\nu = 0.3 \text{ eV}$ (blue), for $f_{R0} = 10^{-5}$ (orange) and the combined effect. The grey shaded region shows a 5% deviation from the fiducial value. Over the mass range $M > 10^{14} M_\odot h^{-1}$ relevant for cluster abundance studies the effects of neutrinos and modified gravity are approximately degenerate.

In this picture, we account for the effect of neutrinos by introducing an appropriate shift in the time variable σ^2 of the random walk. This rescaling expresses the cold dark matter approximation outlined above and it allows us to compare the effects of modified gravity and neutrinos on the threshold directly. While there is some ambiguity how to compare cosmologies with and without neutrinos, in this paper we choose to keep the total matter density Ω_m fixed. Thus when adding neutrinos, we rescale the dark matter density by (Lesgourgues and Pastor, 2006)

$$\Omega'_{\text{cdm}} = \Omega_{\text{cdm}} - \frac{\sum m_\nu}{93.14 \text{ eV}}. \quad (4.34)$$

In Fig. 4.4 we show the rescaled critical density for collapse δ'_c and the resulting effect on the halo mass function. A larger δ_c leads to an increased exponential suppression of high mass halos in Eq. 4.14. Note that the scale dependent growth caused by neutrinos translates to a weak mass dependency of the barrier. To check how this suppression can mask the additional abundance caused by modified gravity, we combine the $f(R)$ threshold with the neutrino rescaling from Eq. 4.33:

$$\delta_c^{\text{eff}} = \frac{\sigma(z)}{\sigma_{\text{CDM}}(z)} \delta_c^{f(R)}. \quad (4.35)$$

A suitable combination of neutrino masses and f_{R0} can then lead to an effective barrier close to its Λ CDM value over the mass range $M > 10^{14} M_\odot h^{-1}$ relevant for cluster surveys, as demonstrated in Fig. 4.5. We will return to this point and check the validity of this approach by comparing to simulations in Sec. 4.3.6.

4.3.5 Halo bias and cluster clustering

The mass function also allows us to derive the corresponding clustering bias. The Eulerian bias is given by the overabundance of objects in a region with an overdensity δ_0 compared to the mean abundance

$$b = 1 + \frac{1}{\bar{n}(M)} \frac{d\bar{n}(M|\delta_0)}{d\delta_0} = 1 + \frac{1}{f(\sigma)} \frac{df(\sigma|\delta_0, \sigma_0)}{d\delta_0} \Big|_{\delta_0=0}, \quad (4.36)$$

therefore the first order bias is the linear response of the halo field to changes in the underlying density field. For a fixed barrier, the conditional mass function $f(\sigma|\delta_0)$ simply involves a shift of the barrier $\delta_c \rightarrow \delta_c - \delta_0$, but for a generic barrier the situation is more complicated.

Achitouv et al., 2016 proposed the conditional mass function for a generic barrier

$$f(S|\delta_0, S_0) = \sqrt{\frac{2}{\pi}} \left(\bar{B} - S \frac{d\bar{B}}{dS} + \frac{S^2}{2} \frac{d^2\bar{B}}{dS^2} - \delta_0 \right) \frac{S/a}{(S/a - S_0)^{3/2}} \quad (4.37)$$

$$\times \exp \left(-\frac{(\bar{B} - \delta_0)^2}{2(S/a - S_0)} \right), \quad (4.38)$$

and found good agreement with Monte Carlo random walks for various barrier shapes. This yields the linear bias

$$b(S) = 1 + \left(\frac{a\bar{B}}{S} - \frac{1}{\bar{B} - S \frac{d\bar{B}}{dS}} \right), \quad (4.39)$$

with the same barrier \bar{B} as used for the mass function, but the bias depends only mildly on the barrier width D_B and drift β for the mass range we focus on in this work. It is mainly sensitive to the mean threshold δ_c .

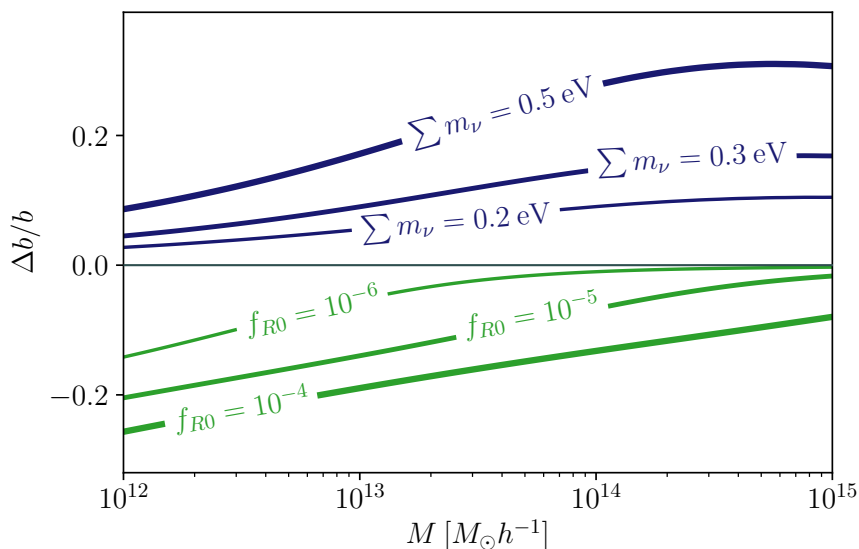


FIGURE 4.6: Deviations from the fiducial GR bias for several values of f_{R0} and $\sum m_\nu$ at redshift $z = 0$. Clusters become more abundant with larger values of f_{R0} , so they become less biased. For neutrinos this trend is reversed, the suppression of high mass objects increases their bias.

We show the changes in the bias induced by modified gravity or massive neutrinos in Fig. 4.6 using the $f(R)$ barrier $\bar{B}(M, z, f_{R0})$. The lower threshold means that clusters form out of smaller overdensities compared to Λ CDM, so they are less biased tracers of the density field. This tendency is only enhanced the stronger the $f(R)$ effect gets and the linear bias shrinks with larger values of f_{R0} . For neutrinos, this effect is reversed: because the high-mass tail of the mass function is suppressed, massive clusters are less abundant overall and therefore only form in very overdense regions. However the absolute scale of the halo bias in Λ CDM is still uncertain (Baxter et al., 2016; Paech et al., 2017), making it very difficult to use this behaviour for constraints – both neutrinos and modified gravity lead to a lower bias of low-mass objects compared to high-mass objects. We therefore leave a forecast analysis also including the clustering of clusters for future work.

4.3.6 Calibration and comparison

The excursion set framework predicts the mass function in terms of the halo mass at virialization dn/dM_{vir} since this is the time at which the halo stops to collapse. Moving to modified gravity, the virial overdensity is even more complicated. While constant in an Einstein-de-Sitter universe, we expect $\Delta_{\text{vir}}^{f(R)}$ to evolve with both redshift and f_{R0} .

From the observational point of view, however, the mass of a cluster is often defined as the mass inside a sphere encompassing an overdensity Δ times a reference value. In this work we adopt $\Delta_m = 200$ with respect to the mean matter density as given in Eq. 4.1 to define our simulated catalogues and calibrate the mass function accordingly.

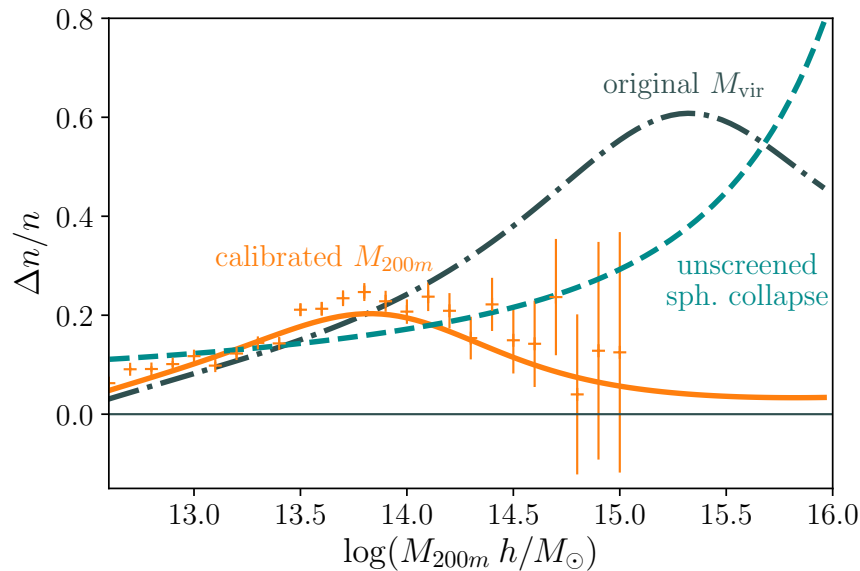


FIGURE 4.7: Relative simulated M_{200m} halo abundance for $f_{R0} = 10^{-5}$ at redshift $z = 0.3$ compared with the original spherical collapse prediction for virial masses (grey, dot-dashed) and our calibrated model (orange, solid). For comparison, we also show the unscreened spherical collapse prescription from Eq. 4.43 (cyan, dashed) used in previous studies as explained in the main text.

A first exemplary comparison between the fiducial barrier model Eq. 4.24 and our simulation is shown in Fig. 4.7 for $f_{R0} = 10^{-5}$ and $z = 0.3$. As expected the virial

TABLE 4.3: Best-fit parameters for the width D_B and the drift β of the fiducial GR barrier and the calibrated values for the modified gravity threshold $\delta_c(f_{R0}, z)$ in Eq. 4.24. The statistical uncertainty of the fit is the last significant digit.

GR		$f(R)$			
D_B	β	α_4	β_3	μ_1	μ_2
0.37	0.11	0.067	5.6×10^{-3}	1.38	21.32

mass function from Kopp et al., 2013 is a bad fit to the M_{200m} catalogue and we can see that the screening mass is offset, leading to a wrong position and amplitude of the $f(R)$ bump. To calibrate the mass function to a new mass definition, we focus on the screening mass m_b in Eq. 4.26. We keep the functional form, but because the position and evolution of the screening mass scale is different for another mass definition, we re-fit the parameters μ_1, μ_2 to account for the evolution with f_{R0}, β_3 to adapt the height of the relative abundance peak and α_4 to adjust the redshift evolution. This is done via minimisation of the Gaussian log-likelihood

$$\ln \mathcal{L} = -\frac{1}{2} (\mathbf{N}^{\text{theo}} - \mathbf{N}^{\text{sim}}) \mathbf{C}^{-1} (\mathbf{N}^{\text{theo}} - \mathbf{N}^{\text{sim}})^T - \frac{1}{2} \ln \det \mathbf{C}^{-1}, \quad (4.40)$$

where the covariance matrix consists of a Poissonian contribution and a sample variance term

$$\mathbf{C}_{ij}^{-1} = \delta_{ij} N_i^{\text{theo}} + b_i b_j N_i^{\text{theo}} N_j^{\text{theo}} \sigma(V_{\text{box}}) \quad (4.41)$$

with theoretical cluster counts N_i^{theo} per mass bin i and $\sigma(V_{\text{box}})$ is the variance of the density field computed inside the box. We calculate the mean bias averaged over a bin ΔM_i as

$$\bar{b}_i = \int_{\Delta M_i} dM \frac{dn}{dM} b(M) / \int_{\Delta M_i} dM \frac{dn}{dM}, \quad (4.42)$$

using Eq. 4.39 for the bias and Eq. 4.29 for the mass function. Note that the barrier shape given by D_B and β is very important for the proper GR limit, but largely cancels in Eq. 4.29. The mass function ratio is therefore almost completely independent from the fiducial barrier values. So while we choose to work within a consistent framework with a mass function that is extended to $f(R)$, one could also replace f_x^{GR} in Eq. 4.29 with another multiplicity function such as ones by Tinker et al., 2008 or Crocce et al., 2010 as long as it is also calibrated to M_{200m} . We do not perform a comprehensive comparison of mass functions here, but we note that our results for bias and multiplicity agree within $\sim 5\%$ with those established results in the literature – a value we take as an estimate for current systematic effects on the halo mass function mainly due to differences in halo definition.

Within our simulations, we find no preference for any redshift evolution in the GR barrier parameters D_B and β . We fit them to our Λ CDM simulations first and keep them fixed while calibrating the remaining $f(R)$ parameters α_4, β_3, μ_1 and μ_2 to our fR4, fR5 and fR6 simulations. The resulting best-fit values with statistical errors are shown in Tab. 4.3. For the Λ CDM barrier values we find qualitative agreement with previous similar studies (Maggiore and Riotto, 2010b; Kopp et al., 2013; Achitouv et al., 2016) while the position and evolution of the screening mass m_b given by the other

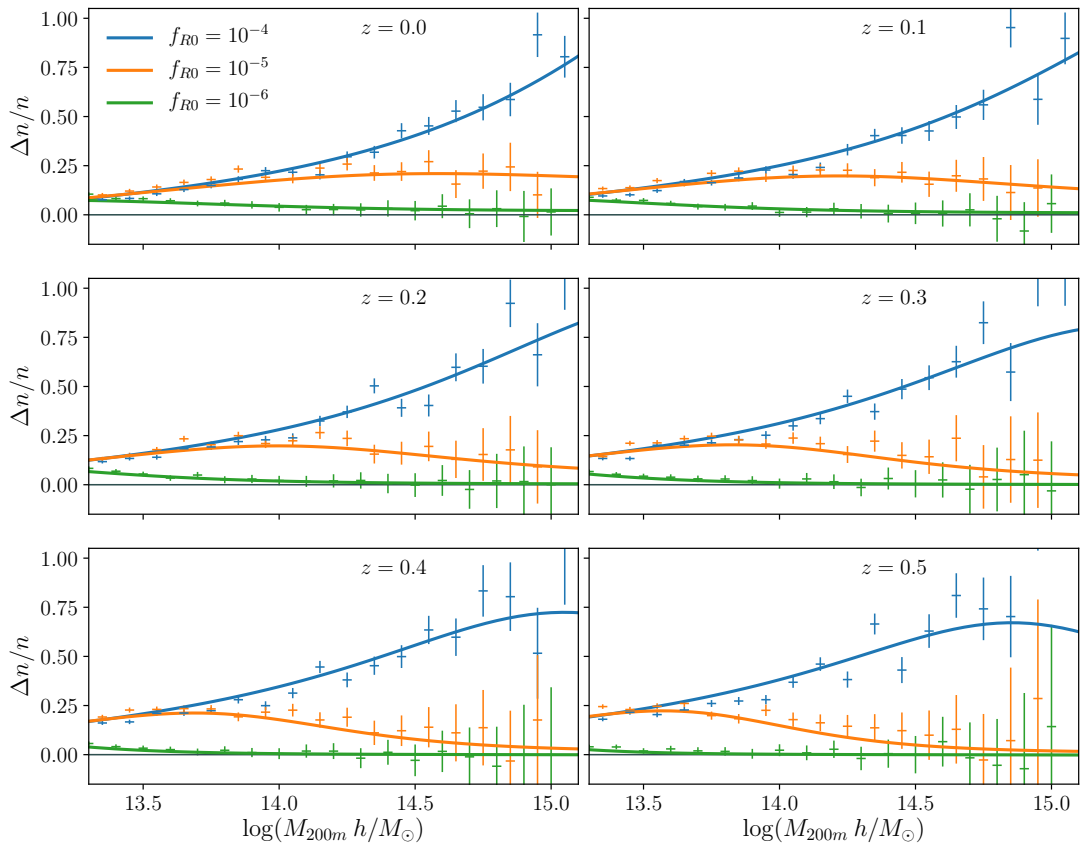


FIGURE 4.8: Calibrated halo mass function ratio between our theoretical model and the simulation suite for various redshifts and values of $f_{R0} = 10^{-4}$ (blue), 10^{-5} (orange) and 10^{-6} (green). The characteristic $f(R)$ bump in the relative abundance moves towards lower masses with redshift.

parameters deviates substantially from the virial mass function from Kopp et al., 2013. The results are compared to our simulated catalogues in Fig. 4.8 for a wide range of redshifts and values of f_{R0} . We find that our model for the halo mass function can reproduce the simulated data by fitting only four parameters to account for the full non-linear behaviour of the modified gravity model.

For completeness, we also compare our result to a previously used prescription for the modified gravity mass function in Fig. 4.7. In this ansatz proposed by Cataneo et al., 2015, the relative effect of $f(R)$ is captured by a ratio of ellipsoidal collapse multiplicity functions

$$\frac{f^{f(R)}}{f^{\text{GR}}} \approx \frac{f^{\text{ST}}(\sigma^{f(R)}, \delta_{c,\text{unscr.}}^{f(R)})}{f^{\text{ST}}(\sigma^{\text{GR}}, \delta_{c,\text{GR}}^{\text{GR}})}, \quad (4.43)$$

where f^{ST} denotes the mass function by Sheth and Tormen, 2002. The density variance is calculated using the linear power spectrum $P(k)$ in the respective theory, and $\delta_{c,\text{unscr.}}^{f(R)}$ denotes the threshold for spherical collapse in case the theory is unscreened everywhere, i.e. gravity is enhanced by 4/3 (Schmidt, Vikhlinin, and Hu, 2009)

$$\delta_{c,\text{unscr.}}^{f(R)}(z) = 1.7063 \left(1 - 0.0136 \log_{10} \left(1 + \frac{\Omega_m^{-1} - 1}{(1+z)^3} \right) \right), \quad (4.44)$$

which shares the functional form of Eq. 4.27 but differs in the numerical coefficients. In comparison to our simulations, we can see that this prescription fails to properly predict the onset and shape of the characteristic enhancement peak.

The next step is to test the inclusion of neutrinos into our framework via Eq. 4.35. We show the combined effect of neutrinos and modified gravity measured from our simulations in Fig. 4.9 - note that the simulations including neutrinos were not used to fit the mass function parameters. Both cosmologies show an approximate degeneracy leading to an abundance of clusters that is within 10% consistent with Λ CDM expectation at $z = 0$, and the behaviour is well captured by our mass function. This cancellation weakly depends on redshift, so cosmologies with similar mass functions at $z = 0$ will in general differ at earlier times. The precise degeneracy depends on the survey specifications such as redshift range and selection function, and we will return to this problem within the full cosmological parameter space in the next section.

The fact that the inclusion of neutrinos via Eq. 4.35 works so well is actually surprising because it suggests universality of the $f(R)$ mass function when expressed in terms of $\nu = \delta_c^2(f_{R0}, z)/\sigma^2$ once the explicit evolution of the collapse threshold is accounted for. In GR, this behaviour is ensured by the Birkhoff theorem, but we cannot rely on it in modified gravity theories.

4.4 Forecasts

To assess if differences in the cluster abundance are measurable, it is important to consider the changes in the halo mass function in the context of a survey with a specific selection function.

We now show with two idealised test cases the consequences of our results for the ability of current and future surveys to constrain f_{R0} . The abundance of clusters is mostly sensitive to $(\Omega_m, \sigma_8, \sum m_\nu, \log f_{R0})$; as for the other relevant cosmological parameters we include priors from different probes. This has to be done with caution, because datasets might show different results when analysed in a $f(R)$ framework. We therefore make use of the fact that the model reproduces a Λ CDM expansion history and limit ourselves to *geometrical* probes.

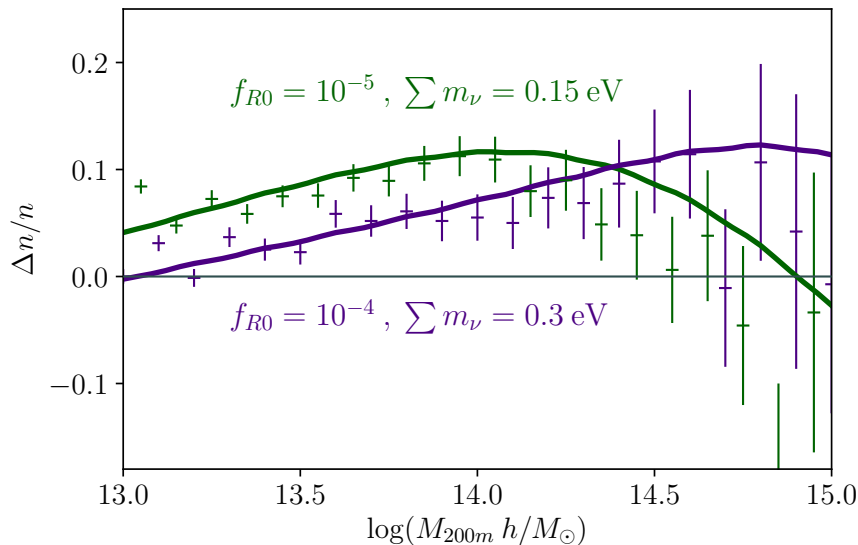


FIGURE 4.9: Joint effect of modified gravity and neutrinos on the relative halo abundance at $z = 0$. The theoretical abundance is calculated by combining the calibrated $f(R)$ barrier with the neutrino rescaling (Eq. 4.33). Both cluster abundance predictions deviate by less than 10% from the Λ CDM predictions.

TABLE 4.4: A summary of the complementary BAO and BBN mock data sets used in combination with cluster counts if indicated. We assume these result in Gaussian priors on the measured quantity with mean μ and width σ .

Probe	Quantity	μ	σ
BAO	$D_V(z = 0.38)/r_s$	10.05	0.17
	$D_V(z = 0.51)/r_s$	12.84	0.13
	$D_V(z = 0.61)/r_s$	14.77	0.13
BBN	$100 \times \Omega_b h^2$	2.224	0.046

We add baryon acoustic oscillation priors on the distance scale $D_V(z)$ based on BOSS DR12 data (Alam et al., 2017) at redshifts $z = 0.38, 0.51$ and 0.61 . We centre them on our fiducial cosmology and assume pre-reconstruction errors on the data points, i.e. without assuming a Λ CDM model to linearise the BAO signal, which results in conservative results. We denote this data set with BAO. Complementary, big-bang nucleosynthesis measurements constrain the baryon density $\Omega_b h^2$ in the early universe, where any $f(R)$ effects are negligible. The width of the error bar is based on Cooke et al., 2014. A summary of both sets of Gaussian priors is given in Tab. 4.4.

The most powerful complementary data set comes from the CMB. If indicated, we combine the cluster data with priors on the primary CMB parameters derived from the Planck-high- ℓ temperature power spectrum. We use the publicly available chains either for the base model or including varying neutrino masses to derive the covariance matrix and use this Gaussian prior, again centred on our fiducial cosmology. While changes to the temperature anisotropy power spectrum by $f(R)$ gravity are introduced via the integrated Sachs-Wolfe effect at late times, the impact on multipoles $\ell > 30$ is very small for the relevant parameter space.

4.4.1 Optical cluster surveys

We now explore these effects in the context of a forecast for an optical cluster survey, where the main observable is the cluster richness λ . We model the expected number counts per bin in redshift Δz_i and richness $\Delta \lambda_j$ as

$$\langle N_{ij} \rangle = \Omega \int_{\Delta z_i} dz \frac{dV}{dz} \int_0^\infty dM \frac{dn}{dM} \int_{\Delta \lambda_j} d\lambda p(\lambda|M), \quad (4.45)$$

where the survey area Ω is fixed, and introduce the probability $p(\lambda|M)$ for a cluster of mass M to be observed with a richness λ . We assume a log-normal distribution, which allows us to solve the integration over the observable to arrive at

$$\langle N_{ij} \rangle = \Omega \int_{\Delta z_i} dz \frac{dV}{dz} \int_0^\infty dM \frac{1}{2} \left(\operatorname{erfc}(x_{\min}) - \operatorname{erfc}(x_{\max}) \right) \frac{dn}{dM}, \quad (4.46)$$

with

$$x_{\min/\max} \equiv \frac{\ln \lambda_{\min/\max} - \langle \ln \lambda \rangle(M)}{\sqrt{2\sigma_{\ln \lambda}^2}}. \quad (4.47)$$

We use the weak-lensing calibrated $M - \lambda$ relation measured by Murata et al., 2018 on SDSS clusters:

$$\langle \ln \lambda \rangle(M) = A + B \ln \left(\frac{M}{M^*} \right) \quad (4.48)$$

$$\sigma_{\ln \lambda}(M) = \sigma_0 + q \ln \left(\frac{M}{M^*} \right), \quad (4.49)$$

where $M^* = 3 \times 10^{14} M_\odot / h$ is the pivot mass of the relation and A, B, σ_0 and q are free parameters varied within priors given by the measurements by Murata et al., 2018. Note that the weak lensing mass estimate of a given cluster is not affected by $f(R)$ because geodesics are unchanged up to a negligible factor $1 + f_{R0}$.

In addition to these observational uncertainties, also the mass function measured in simulations shows systematic scatter. This is mainly caused by ambiguities in the halo definition, so even an identical underlying dark matter field can result in slightly different halo statistics. Typically, different halo finders vary in the resulting amplitude and tilt of the mass function (Knebe et al., 2011), so we assume

$$\frac{dn}{dM} \rightarrow \frac{dn}{dM} \left(\gamma + \eta \log \left(\frac{M}{M^*} \right) \right) \quad (4.50)$$

with γ and η free to vary with Gaussian priors with width $\sigma = 0.05$ centred at 1 and 0 respectively. Because these systematic errors are by far larger than statistical uncertainty in our fit of barrier parameters, we keep the latter fixed.

The selection function is crucial for the specific degeneracy between parameters, so we distinguish two cases: Either a large, shallow layout or a deeper survey focused on a smaller sky area.

For the shallow case, we assume an area of 10^4 deg^2 with eight richness bins as in Murata et al., 2018 $\lambda \in [20, 25, 30, 35, 40, 47.5, 55, 77.5, 100]$ and one redshift bin $z \in [0.1, 0.3]$. This translates to an approximately flat limiting mass of $M_{\min} \sim 10^{14.4} M_\odot / h$. All bins are well populated with over 100 clusters so we assume a Gaussian likelihood as in Eq. 4.40. This mock survey is combined with either

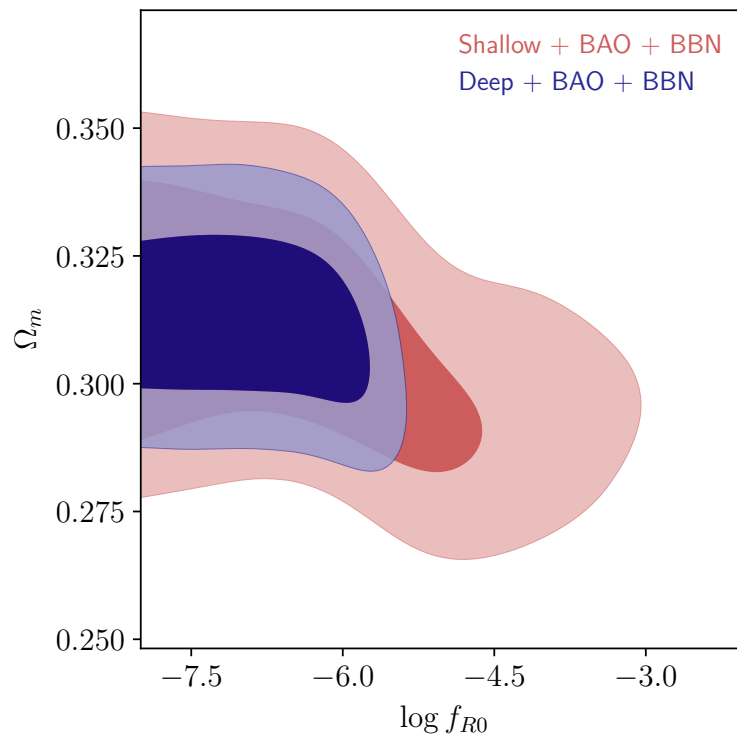


FIGURE 4.10: Expected constraints on f_{R0} from a shallow or deep optical cluster survey as described in the text. The cases shown here keep the neutrino mass fixed.

CMB or BAO + BBN priors as given in Tab. 4.4 and we evaluate the resulting likelihood using the Monte Carlo Markov Chain code `MontePython` (Audren et al., 2013; Brinckmann and Lesgourgues, 2018).

We show the cluster count distribution in redshift and richness for a shallow survey in Fig. 4.11. For the given selection function, at low redshifts the effects of neutrinos and modified gravity are almost completely degenerate. Both roughly translate into a shift in the overall amplitude which is also easily mimicked by the amplitude of the $M - \lambda$ relation. The richness information does help to break this degeneracy slightly because neutrinos tend to cause a strong suppression of very massive clusters while modified gravity leads to a higher abundance of low- and intermediate mass objects. The resulting limits on f_{R0} that can be achieved with such a survey are shown in Tab. 4.5. If cluster counts are only combined with BAO information, the limits are rather weak and when adding neutrinos we find no relevant upper bound. Adding the CMB improves the situation by pinning down the other cosmological parameters, but even then adding neutrinos weakens the bounds considerably. Note that there is a small additional effect due to broader CMB constraints on other parameters in a ν CDM cosmology, but this mostly extends the contours in the direction of larger allowed Ω_m values while f_{R0} is anti-correlated with the matter density.

For the deep survey, we take an area of 5000 deg^2 – the total area that will be covered by the Dark Energy Survey¹ – and bins in richness $\lambda \in [20, 30, 45, 60, 200]$ and redshift $z \in [0.2, 0.35, 0.5, 0.65, 0.8]$. The resulting cluster counts for this configuration in redshift and richness are shown in Fig. 4.12. Information about the abundance at higher redshifts helps in breaking the degeneracy, because while neutrinos suppress

¹<https://www.darkenergysurvey.org>

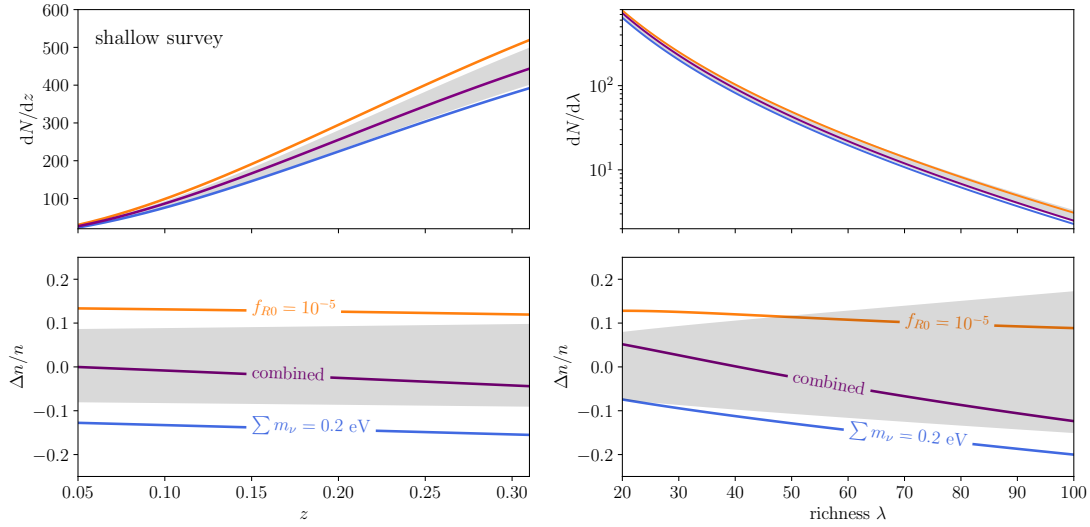


FIGURE 4.11: Left: Evolution of cluster counts with redshift for the shallow optical cluster survey described in the text. Grey shaded bands indicate 1σ uncertainty in the mass-richness-relation. The bottom plot shows relative deviations caused by modified gravity (orange), massive neutrinos (blue), or both (violet). For low redshifts with the given selection function, both effects are approximately a shift in total amplitude of the counts. Right: Richness distribution of cluster counts. The bottom plot shows relative deviations.

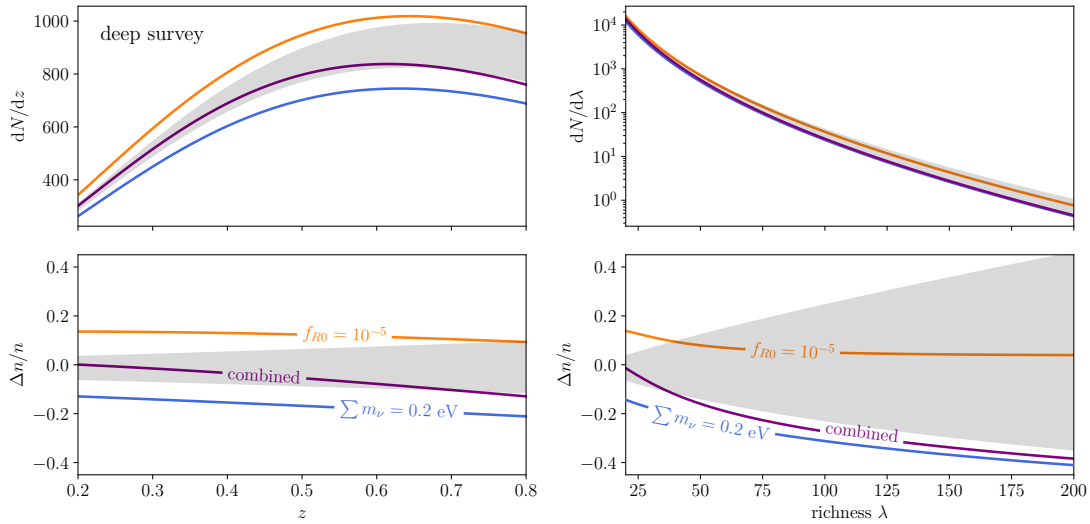


FIGURE 4.12: Left: Evolution of cluster counts with redshift for the deep optical cluster survey described in the text. Grey shaded bands indicate 1σ uncertainty in the mass-richness-relation. The bottom plot shows relative deviations caused by modified gravity (orange), massive neutrinos (blue), or both (violet). While degenerate at low redshifts, neutrino effects are more pronounced at high z (where the $f(R)$ mass function reverts to GR). Right: Richness distribution of cluster counts. The bottom plot shows relative deviations. The degeneracy here crucially depends on the position of the $f(R)$ peak in the relative abundance.

TABLE 4.5: Expected constraints from optical cluster surveys in various configurations as described in the text.

Probes	Limit (95 %)
Shallow + BAO + BBN	$ f_{R0} < 8.1 \times 10^{-4}$
Shallow + BAO + BBN + ν	–
Shallow + BAO + BBN + CMB	$ f_{R0} < 7.6 \times 10^{-5}$
Shallow + BAO + BBN + CMB + ν	$ f_{R0} < 1.5 \times 10^{-4}$
Deep + BAO + BBN + ν	$ f_{R0} < 2.0 \times 10^{-6}$

the population there, the $f(R)$ mass function reverts to GR for $z > 0.5$. Even though modified gravity boosts the abundance of high mass clusters at low redshifts as shown in Fig. 4.8, integrated over z the effect on low-richness clusters is dominant as shown on the right panel of Fig. 4.12. Neutrinos on the other hand suppress the high-mass end of the halo mass function, so that – when combined – the two effects largely break the degeneracy between $f(R)$ and neutrinos. Even without adding CMB information, such a survey can constrain f_{R0} down to the effective cluster floor of $\sim 10^{-6}$ independent of neutrinos. We show the resulting posterior from both surveys combined with BAO and BBN priors for vanishing neutrino mass in Fig. 4.10.

4.4.2 SZ cluster surveys

The thermal Sunyaev-Zeldovitch (SZ) effect is the heating of CMB photons by scattering with hot electron plasma in clusters of galaxies, leading to a characteristic distortion of the blackbody spectrum. The measured amplitude is expressed by the Compton y -parameter and is given by the integrated electron density n_e weighted with their temperature T_e along the line of sight

$$y \propto \int n_e T_e dl \propto M \langle T_e \rangle. \quad (4.51)$$

If we assume a virialised system, $\langle T_e \rangle \propto M^{2/3}$ and the amplitude scales as $y \propto M^{5/3}$. The potential energy of such a cluster is given by

$$\langle E_{\text{pot}} \rangle \propto -\frac{GM^2}{R} \propto -GM^{5/3} \propto -y, \quad (4.52)$$

therefore the thermal SZ effect is a probe of the potential energy. In unscreened $f(R)$ gravity, potentials are deeper by a factor of 4/3 and thus a cluster with the same mass will induce a larger SZ signal compared to a standard cosmology.

A SZ selected cluster sample will hence show a higher abundance in modified gravity both due to the mass function enhancement discussed so far, but also due to modifications of the selection function because lower mass clusters will surpass the detection threshold.

To model this effect, we consider the relative strength of gravity

$$g(r) \equiv \frac{d\psi/dr}{d\psi_N/dr} \quad (4.53)$$

normalised by the Newtonian expectation ψ_N which varies between 1 in the screened regime and 4/3 for the unscreened case. From this we can derive the weighted average

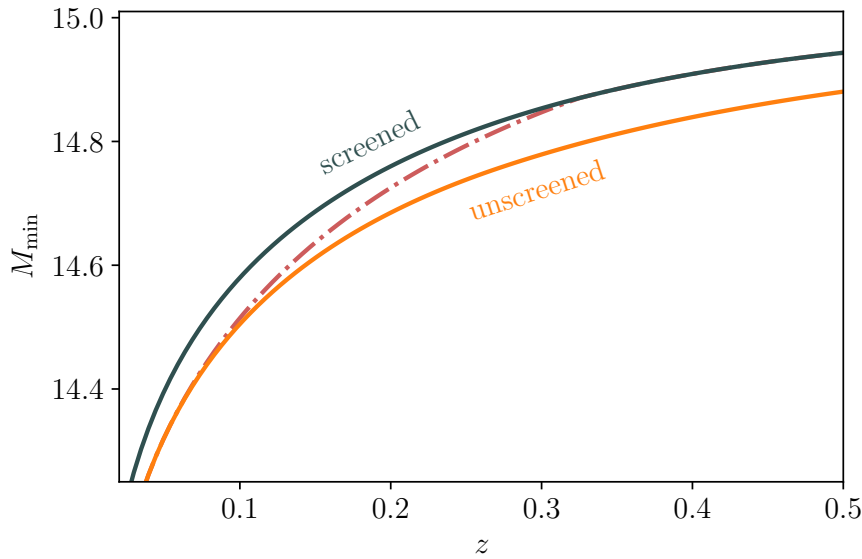


FIGURE 4.13: Limiting mass using the Planck SZ cluster selection function for the fiducial case (grey), assuming all clusters are unscreened for a high value of $f_{R0} = 10^{-4}$ (orange) and an intermediate case where parts of the sample are screened with $f_{R0} = 5 \times 10^{-5}$ (red, dot-dashed).

$$\bar{g} = \frac{\int dr r^2 w(r) g(r)}{\int dr r^2 w(r)}, \quad (4.54)$$

with the weighting function

$$w(r) = \rho(r) r \frac{d\psi_N}{dr} \quad (4.55)$$

which corresponds to the averaged additional potential energy. We follow Schmidt, 2010 and make the simplified assumption that the fifth force is only sourced by mass outside of the radius given by Eq. 3.65. Therefore we write

$$g(r) = 1 + \frac{1}{3} \frac{M(< r) - M(< r_{\text{screen}})}{M(< r)}, \quad (4.56)$$

where r_{screen} is the radius where the equality in Eq. 3.65 holds. The time evolution of r_{screen} and subsequently \bar{g} is induced by the background evolution of f_R

$$\bar{f}_R(z) = f_{R0} \frac{\Omega_m + 4\Omega_\Lambda}{\Omega_m(1+z)^3 + 4\Omega_\Lambda}, \quad (4.57)$$

and the integrals in Eq. 4.54 can be solved by assuming NFW profiles so both density and potential are determined. Note that \bar{g} is only very weakly sensitive to the concentration of the profiles, so we fix the relation to the results of Bullock et al., 2001. Even though halos tend to be more concentrated in $f(R)$, this does not change our qualitative argument.

From Eq. 4.52 we therefore expect the mass estimate to be biased compared to GR by

$$M_{\text{eff}} = \bar{g}^{3/5} M_{\text{true}}, \quad (4.58)$$

i.e. the SZ signal coming from an unscreened cluster of fixed mass is higher by a factor of $(4/3)^{3/5} \simeq 1.19$ compared to the GR expectation. Similar arguments have been used

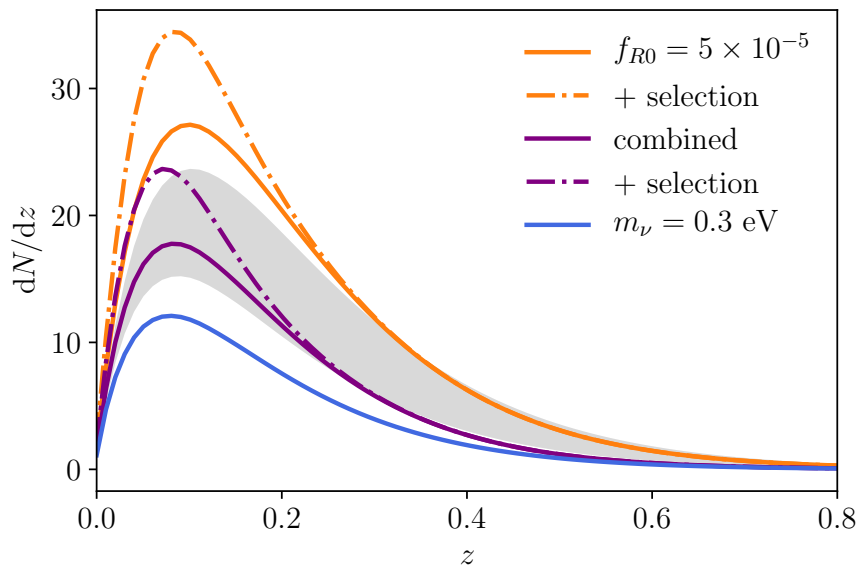


FIGURE 4.14: Redshift distribution for the Planck cluster counts due the halo mass function into account (solid) and selection function effects (dot-dashed). Grey bands indicate a 10% uncertainty in the cluster mass scale set by $(1 - b)$.

before to constrain $f(R)$ by comparing lensing masses with X-ray (Wilcox et al., 2015) or dynamical mass estimates (Pizzuti et al., 2017). Here we want to incorporate the effect into a cluster abundance framework.

To illustrate the method, we consider the consequences for the Planck SZ cluster sample (Planck Collaboration et al., 2015). There, the hydrostatic mass bias $(1 - b)$ is introduced to account for the difference between masses inferred from lensing and the corresponding hydrostatic SZ signal. In $f(R)$, we therefore expect $(1 - b)$ to be modified by an additional factor $\bar{g}^{3/5}$. Because the mass definition used in SZ surveys is typically M_{500c} , we calculate NFW potentials to determine \bar{g} using this mass definition and we consider a cluster fully screened if the condition in Eq. 3.65 has not been met at R_{500c} .

In Fig. 4.13 we show the resulting limiting mass for the Planck SZ selection function. Because the clusters in the sample are very massive, they are screened unless f_{R0} reaches quite high values $\sim 10^{-4}$. However, if all clusters in the Planck sample are unscreened, this would be completely absorbed by the fiducial measurement of the bias factor - but because the lensing calibration is performed on very massive objects, smaller objects can still exhibit deviations. This is illustrated with the dot-dashed line for $|f_{R0}| = 5 \times 10^{-5}$.

The resulting Planck SZ cluster counts are shown in Fig. 4.14. Here we recalibrate our mass function to M_{500c} using the rescaling outlined in Hu and Kravtsov, 2003. While this simplified procedure will not predict the position of the screening mass and the subsequent position of the $f(R)$ peak in the mass function correctly, we just want to point out that the effect of the adjusted selection function can be quite powerful - in this case as important as the higher cluster abundance from the mass function itself.

The high mass scale for the Planck clusters limits the usefulness of this method here, but upcoming X-ray surveys such as *eRosita*² are expected to detect clusters and groups down to $M \sim 10^{13} M_{\odot} / h$ where similar methods can be very powerful.

²<http://www.mpe.mpg.de/eROSITA>

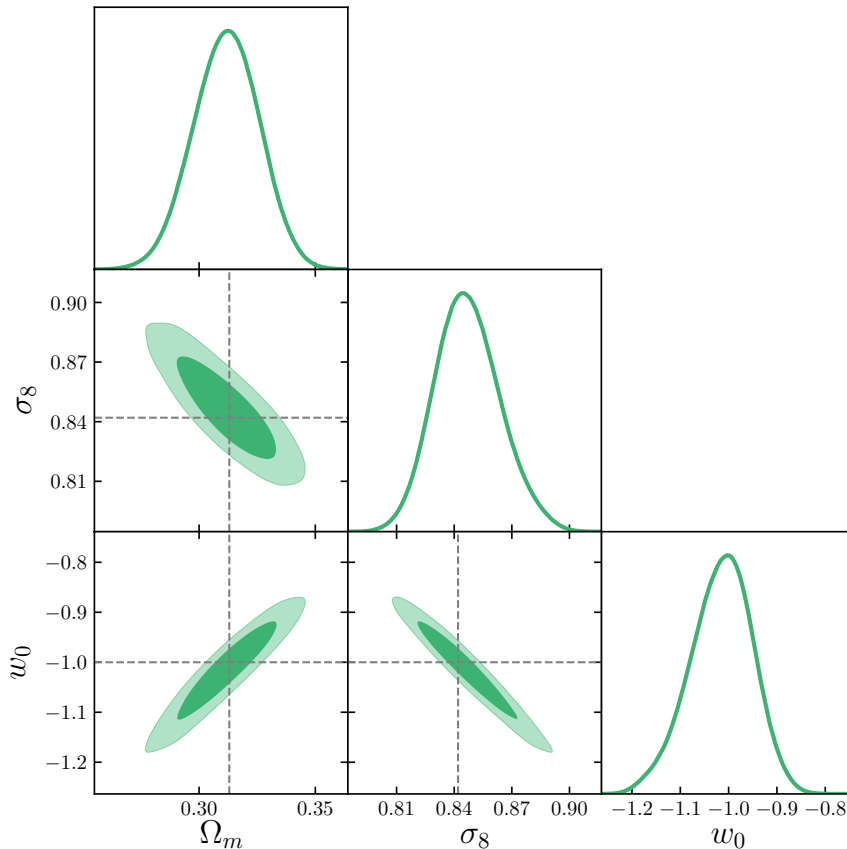


FIGURE 4.15: Posterior distribution of the main cosmological parameters for the shallow survey + BBN + BAO + CMB with a fiducial model generated using $f_{R0} = 10^{-4}$. All parameters are fully consistent with a vanilla Λ CDM model and none (including nuisance parameters not plotted here) show significant deviations $> 1\sigma$ from their fiducial values indicated by dashed lines.

4.4.3 Searching for modified gravity with other parametrisations

The problem in searching for modifications of gravity is that theory space is enormous, and there are potentially many models to test. Current and future cosmological surveys are mostly designed to search for deviations in the dark energy equation of state w from -1 , so we might wonder if these standard searches are sufficient to detect deviations from Λ CDM without assuming a specific model. The hope is then that once an anomaly is detected (for example an equation of state $w \neq -1$), one can resolve the tension in an extended model involving new physics.

As a test case, we set $\sum m_\nu = 0$ and generate a fiducial cluster catalogue with $f_{R0} = 10^{-4}$ for the shallow optical cluster survey described above combined with CMB and BAO + BBN information. This value of f_{R0} is larger than the 95 % upper limit $f_{R0} < 7.2 \times 10^{-5}$ from the same combination of data sets given in Tab. 4.5. We then explore the posterior assuming a w CDM model and use the according CMB covariance matrix for our prior.

We find that the best-fit w CDM model does not show any significant deviations from the vanilla case. The full posterior distribution of the major cosmological parameters is shown in Fig. 4.15, and while there are small deviations in the nuisance parameters, all of them are within 1σ compatible with their standard values without

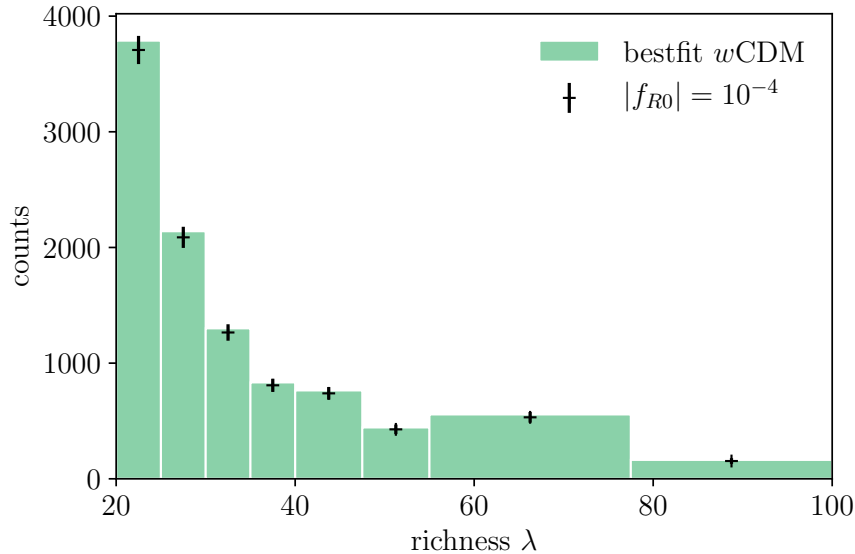


FIGURE 4.16: Bars show the binned richness distribution of clusters for the best-fit w CDM model compared to the fiducial data points generated with $f_{R0} = 10^{-4}$. All parameters for the best-fit model agree within 1σ with their fiducial values.

any peculiar features.

We also compare the richness distribution of cluster counts for the best-fit model with the $f(R)$ mock data in Fig. 4.16 and find no significant deviations. The full parameter space (including the nuisance parameters described above) proves to be flexible enough to account even for a large value of f_{R0} that could be detected if the correct model is assumed in the analysis. This indicates that w CDM might not be a good approach to search for generic deviations from Λ CDM for models that are not captured by this particular parametrisation.

Therefore we can not necessarily exclude modified gravity (or other) models just from the lack of tensions in the Λ CDM or w CDM analysis of cosmological surveys. Instead, it is necessary to consider the phenomenology of models individually in order to rule them out.

4.5 Cluster kinematics in modified gravity

The presence of force enhancement inside the cluster can also have an effect on other observables. The kinematics of cluster members is a prime example and connected to the gravitational potential via the virial theorem. The same discussion as in Sec. 4.4.2 therefore applies: a modification of the dynamical potential leads to systematic deviations from the GR expectation. In the case of kinematics, we expect the velocity dispersions to be larger in $f(R)$.

We measure the velocity dispersion σ of dark matter particles in our simulations for a wide range of clusters. The results are presented in Fig. 4.17. All $f(R)$ models included here converge to the same virial value of σ in the unscreened regime for cluster $M < 10^{14} M_{\odot} h^{-1}$ where the additional force is present. For very massive clusters $M \approx 10^{15} M_{\odot} h^{-1}$ the $f_{R0} = 10^{-5}$ models revert to the Λ CDM value, while $f_{R0} = 10^{-4}$ still shows deviations. Note that these very massive clusters are screened for all models, but for $f_{R0} = 10^{-4}$ the velocity dispersions still carry an imprint of the past force

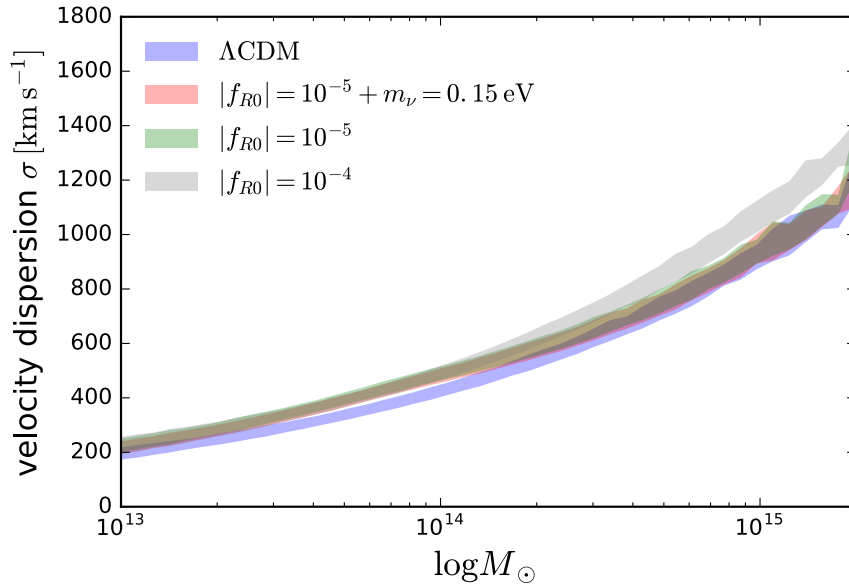


FIGURE 4.17: Average velocity dispersion σ of dark matter particles in halos measured in our simulations. The shaded areas correspond to the statistical error bars. Low-mass halos are unscreened for $|f_{R0}| = 10^{-5}$ (red) and $|f_{R0}| = 10^{-4}$ (grey) and virialise to higher values of σ . Massive clusters are screened, so the $|f_{R0}| = 10^{-5}$ model reverts to the fiducial Λ CDM value. Neutrinos have no measurable effect on the intra-cluster dynamics.

enhancement and did not relax to the new virial equilibrium yet. Neutrinos have no measurable effect on the measured cluster kinematics, so a comparison between lensing mass and kinematic mass to constrain f_{R0} is not affected by them.

This seems very appealing, but intermediate and low mass halos, which are the most interesting objects to find any $f(R)$ effects, have relatively low richness $\lambda \leq 20$. This makes a study on single objects very challenging, but a stacked analysis could become competitive to other methods.

4.6 Conclusion

In this chapter, we presented an accurate halo mass function based on a spherical collapse framework valid for modified gravity and neutrino cosmologies, and calibrated it to a suite of specifically-designed cosmological simulations, the *DUSTGRAIN-pathfinder* runs. This allows joint constraints from cluster abundance studies. We keep the additional relative change and the fiducial GR mass function separate, so our results can be used with any other mass function calibrated to our mass definition of M_{200m} .

The cluster mass definition is crucial to accurately predict the characteristic $f(R)$ peak in the relative abundance because it governs the onset of screening effects. Mass functions for other commonly used mass definitions such as M_{500c} therefore require recalibration of the screening mass, which we refer to future work.

We also demonstrate that the inclusion of neutrinos via a rescaling of the density field Eq. 4.31 still holds in extended models, and we find a degeneracy between effects of $f(R)$ and massive neutrinos in the abundance of clusters that limits the ability of

surveys with small redshift reach to disentangle them. This is likely to weaken existing limits on f_{R0} from cluster abundance, and we will use the mass function for joint constraints using cluster data in a follow-up paper.

Deeper cluster surveys however can tell neutrinos and modified gravity reliably apart by their different redshift evolution, and future optical cluster samples will be able to probe the entire phenomenologically relevant parameter range of the model even when accounting for systematic uncertainties. This could be realised by the complete Dark Energy Survey, eRosita or Euclid³ cluster samples.

We also explore the possibility to include $f(R)$ effects in the selection function of SZ or X-ray surveys directly as proposed by Schmidt, 2010 and we find potentially large effects if the sample can be extended to include nearby, intermediate and low mass objects with $M \lesssim 10^{14} M_{\odot}/h$. Even though neutrinos can mask the additional abundance in the mass function at low redshifts, it is still possible to detect fifth forces through these selection effects. This allows to incorporate the limits on f_{R0} from comparing lensing mass estimates and X-ray, SZ or dynamical mass estimates consistently into cluster abundance studies in a fully consistent framework.

Finally we find that generic searches for w CDM do not necessarily lead to significant tensions or conspicuous features when used to analyse mock $f(R)$ data – even if the value of f_{R0} could be detected with the same data set in a dedicated analysis. This emphasizes the need to model phenomenology of Λ CDM extensions carefully. A lack of tensions within a parametrisation does not imply the absence of new physics.

³<https://www.euclid-ec.org/>

Chapter 5

Summary and outlook

The large-scale structure holds a wealth of information about our Universe. The only question is how to make use of it. For this work, we mostly focused on clusters of galaxies to learn about the dynamics of the underlying density field and to search for deviations from the cosmological standard model.

In Chapter 2, we discussed the detection of galaxy clusters via the SZ effect, which causes the cluster to appear as a characteristic shadow (below 217 GHz) or bright spot (above 217 GHz) on the maps of the CMB. The method is not only powerful because the spectral feature is very unique, but also because the SZ amplitude has a direct connection to the gravitational potential of the halo. This makes one of the problems of cluster cosmology slightly easier - the connection between observed galaxy clusters and the dark matter halos in which they form.

The currently largest SZ selected cluster sample was detected by the Planck satellite, and we discussed the theoretical model that statistically connects the observed SZ flux to the mass of the dark matter halo. This model has to be calibrated by external weak lensing measurements, and current disagreement between various calibrations are the major limiting factor for the interpretation of the cosmological results. We also calculated modifications in the likelihood function induced by the correlation between halos themselves. Even though massive clusters are very rare objects in the universe, they trace the density field and are not randomly distributed. The resulting corrections are noticeable for Planck, but sub-dominant compared to the systematic uncertainty associated with determining the cluster mass scale. For future surveys however, this effect will become relevant.

In the coming years, several currently planned or ongoing cluster surveys will surpass the size of the Planck catalogue by far. We illustrated the power of these upcoming surveys by performing a forecast for the expected cosmological constraints from SZ-selected CORE cluster number counts. While the mission is primarily designed to map the CMB anisotropy just like Planck, we find that the information provided by clusters improves the expected constraints on the dark energy equation of state parameter w_0 drastically.

We then considered possible deviations from Λ CDM more general in Chapter 3. Since we do not have a theoretically appealing contender to the standard model right now, it is tempting to test for deviations in a way as model-independent as possible. For the background evolution, this is usually phrased in terms of the equation of state parameters w_0 and w_a . Since the expansion history is quite tightly constrained today, we move towards the growth of perturbations where Newtonian gravity can be modified by two phenomenological parameters μ and γ which change the strength of gravity and the strength of gravitational lensing respectively. But the restriction to a Newtonian framework limits the usefulness of this approach. For example it is not possible to calculate the CMB anisotropies once μ and γ are specified since dynamics

at the horizon scale are responsible for the shape of the power spectrum. We therefore extended the model to a fully relativistic setting. The full framework is valid at all times and fully self-consistent since it is constructed to obey the relativistic local conservation laws.

The relativistic parametrisation was implemented in the Einstein-Boltzmann code CLASS, which allows us to calculate cosmological perturbations for given μ and γ . The only limitations are numerical stability constraints for solving the perturbations in the early universe, where strong deviations from standard gravity violate underlying assumptions of the approximation schemes. However, such severe modifications are constrained by the data anyway so this is not a severe restriction.

Then we used the parametrised framework for a concrete example, and showed how the perturbations in $f(R)$ gravity can be mapped onto the μ and γ functions. This allows to compute the full linear perturbations for modified gravity cosmologies of that kind. However, we also discussed that the restriction to linear scales is problematic in practice – most information available in the large-scale structure resides on non-linear scales, and on a practical side it is very difficult to find purely linear measurements of growth.

Therefore we turned to the full non-linear dynamics in order to constrain $f(R)$ in Chapter 4 and developed a halo mass function for modified gravity. This was done in a generalised spherical collapse framework, and we used a suite of N -body simulations to calibrate the collapse barrier in $f(R)$. We found that massive neutrinos are a crucial nuisance parameter, since they suppress the abundance of massive clusters which can counteract the boost of the halo mass function expected in modified gravity. Our framework includes both components, modified gravity and neutrinos, and we extensively tested its predictions by comparing it to simulations.

To illustrate the consequence of the $f(R)$ -neutrino degeneracy, we performed forecasts for idealised current and future optical cluster surveys. While the effect is relevant for existing limits, which all neglected neutrino effects so far, the large upcoming samples will be able to distinguish between them. We find that the different redshift evolution of the cluster abundance is key here, so a deep survey (such as the full Dark Energy Survey) can reliably disentangle $f(R)$ from all other cosmological parameters. An application of the mass function to data in order to derive the first constraints on $f(R)$ while fully accounting for systematic uncertainties and neutrino effects is currently ongoing.

We also investigated the consequences of modified gravity effects inside the cluster for the selection function for SZ- or X-ray surveys. If the cluster is unscreened, the additional force contribution boosts the expected SZ or X-ray signal, so lower mass systems make it into the sample that would not surpass the detection threshold in GR. We provide a simplified model in terms of the additional potential energy due to $f(R)$ effects and connect them to observables via the virial theorem. Since the mass function is very steep, a higher signal from systems with fixed mass can have quite large effects. We find that the most promising objects for this kind of analysis are intermediate mass clusters $M \sim 10^{14} M_{\odot} h^{-1}$ at low redshifts $z < 0.2$. Taking the Planck selection function as an example, we demonstrated that the additional abundance due to these astrophysical effects can be as important as the higher abundance caused by the halo mass function.

Then we tested the possibility to detect $f(R)$ effects using other commonly used parametrisations, such as w_0 and w_a . We created artificial $f(R)$ catalogues for values of f_{R0} that could be detected when analysed with the correct model, but fitted a w CDM cosmology to the mock data. We found no suspicious features in the posterior distribution, which is fully compatible with a vanilla Λ CDM model. We conclude

that parametrisations can be a dangerous tool – they do not necessarily capture the features we should be looking for. We are currently working on similar tests for other parametrisations such as μ and γ . Another way is to try to reconstruct an effective linear growth rate D_+^{obs} from cluster data directly.

Cluster kinematics are also a potentially powerful tool to find deviations from standard gravity, and we are currently working on an analysis based on the phase space of member galaxies to build on the discussion about velocity dispersion in modified gravity in Chapter 4. Since relaxation times for cluster are long, of order 10% of the age of the universe, signatures of the enhanced gravitational force can survive in phase space even though the halo might be screened today.

Acknowledgements

This thesis would not have been possible without the support of many people. First of all, it is a pleasure to thank Jochen Weller for your advice, guidance and for always having an open ear. Thank you for four great years! Your homemade sausages are also excellent.

Special thanks also to my collaborators, especially the discussions with Matteo Costanzi were incredibly helpful! Marco Baldi's knowledge about simulations was essential to the results presented in chapter 4. Thanks also to Benjamin Moster, Klaus Dolag and Stefan Hilbert for cross-checking many of our results and rebuilding parts of my shattered trust in N -body simulations. My office mates, Giorgia and Tea, were always there for the crucial coffee breaks, movie nights and very welcome distractions. Thanks! Thanks also to Vanessa and Korbinian for many (not only, but also) scientific discussions, and for being there to tell me how my ideas were wrong. That was great!

I also want to mention the whole physcos group for our great meetings, parties and journal clubs. Kerstin, thank you for the crucial plot style meetings, Python tricks and excellent cookies! Nico, for sharing many beers and long discussions about bias and emptiness. And thanks to Ben, for your advice and never ending optimism. Please teach the machines to go easy on us once they take over. You all made these four years a great experience.

And special thanks to Raffaella and Korbinian for reading parts of this thesis. Your feedback was tremendously helpful, and all mistakes left in here are completely my own.

Bibliography

- Aad, Georges et al. (2015). “Combined Measurement of the Higgs Boson Mass in p p Collisions at $\sqrt{s} = 7$ and 8 TeV with the ATLAS and CMS Experiments”. In: *Physical review letters* 114.19, p. 191803.
- Abbott, TMC et al. (2017). “Dark energy survey year 1 results: cosmological constraints from galaxy clustering and weak lensing”. In: *arXiv preprint arXiv:1708.01530*.
- Achitouv, I. et al. (2016). “Imprint of $f(R)$ gravity on nonlinear structure formation”. In: *Phys. Rev. D* 93.10, 103522, p. 103522. DOI: [10.1103/PhysRevD.93.103522](https://doi.org/10.1103/PhysRevD.93.103522). arXiv: [1511.01494](https://arxiv.org/abs/1511.01494).
- Alam, S. et al. (2017). “The clustering of galaxies in the completed SDSS-III Baryon Oscillation Spectroscopic Survey: cosmological analysis of the DR12 galaxy sample”. In: *MNRAS* 470, pp. 2617–2652. DOI: [10.1093/mnras/stx721](https://doi.org/10.1093/mnras/stx721). arXiv: [1607.03155](https://arxiv.org/abs/1607.03155).
- Albrecht, A. and P. J. Steinhardt (1982). “Cosmology for grand unified theories with radiatively induced symmetry breaking”. In: *Physical Review Letters* 48, pp. 1220–1223. DOI: [10.1103/PhysRevLett.48.1220](https://doi.org/10.1103/PhysRevLett.48.1220).
- Allen, S. W., A. E. Evrard, and A. B. Mantz (2011). “Cosmological Parameters from Observations of Galaxy Clusters”. In: *ARA&A* 49, pp. 409–470. DOI: [10.1146/annurev-astro-081710-102514](https://doi.org/10.1146/annurev-astro-081710-102514). arXiv: [1103.4829](https://arxiv.org/abs/1103.4829) [[astro-ph.CO](https://arxiv.org/archive/astro)].
- Amendola, L. et al. (2012). “Cosmology and fundamental physics with the Euclid satellite”. In: *ArXiv e-prints*. arXiv: [1206.1225](https://arxiv.org/abs/1206.1225) [[astro-ph.CO](https://arxiv.org/archive/astro)].
- Araki, T. et al. (2005). “Measurement of Neutrino Oscillation with KamLAND: Evidence of Spectral Distortion”. In: *Physical Review Letters* 94.8, 081801, p. 081801. DOI: [10.1103/PhysRevLett.94.081801](https://doi.org/10.1103/PhysRevLett.94.081801).
- Arnold, C., V. Springel, and E. Puchwein (2016). “Zoomed cosmological simulations of Milky Way-sized haloes in $f(R)$ gravity”. In: *MNRAS* 462, pp. 1530–1541. DOI: [10.1093/mnras/stw1708](https://doi.org/10.1093/mnras/stw1708). arXiv: [1604.06095](https://arxiv.org/abs/1604.06095).
- Arnold, C. et al. (2018). “The modified gravity lightcone simulation project I: Statistics of matter and halo distributions”. In: *ArXiv e-prints* 1805.09824. arXiv: [1805.09824](https://arxiv.org/abs/1805.09824).
- Arnold, Christian, Ewald Puchwein, and Volker Springel (2015). “The Lyman alpha forest in $f(R)$ modified gravity”. In: *Mon. Not. Roy. Astron. Soc.* 448.3, pp. 2275–2283. DOI: [10.1093/mnras/stv146](https://doi.org/10.1093/mnras/stv146). arXiv: [1411.2600](https://arxiv.org/abs/1411.2600) [[astro-ph.CO](https://arxiv.org/archive/astro)].
- Astier, Pierre et al. (2006). “The Supernova Legacy Survey: Measurement of Ω_M , Ω_Λ and w from the First Year Data Set”. In: *Astron. Astrophys.* 447, pp. 31–48. DOI: [10.1051/0004-6361:20054185](https://doi.org/10.1051/0004-6361:20054185). arXiv: [astro-ph/0510447](https://arxiv.org/abs/astro-ph/0510447).
- Audren, Benjamin et al. (2013). “Conservative Constraints on Early Cosmology: an illustration of the Monte Python cosmological parameter inference code”. In: *JCAP* 1302, p. 001. DOI: [10.1088/1475-7516/2013/02/001](https://doi.org/10.1088/1475-7516/2013/02/001). arXiv: [1210.7183](https://arxiv.org/abs/1210.7183) [[astro-ph.CO](https://arxiv.org/archive/astro)].
- Baldauf, T. et al. (2013). “Halo Stochasticity from Exclusion and non-linear Clustering”. In: *arXiv:1305.2917*. arXiv: [1305.2917](https://arxiv.org/abs/1305.2917) [[astro-ph.CO](https://arxiv.org/archive/astro)].
- Baldi, Marco and Francisco Villaescusa-Navarro (2018). “Cosmic degeneracies – II. Structure formation in joint simulations of warm dark matter and $f(R)$ gravity”. In: *Mon. Not. Roy. Astron. Soc.* 473.3, pp. 3226–3240. DOI: [10.1093/mnras/stx2594](https://doi.org/10.1093/mnras/stx2594). arXiv: [1608.08057](https://arxiv.org/abs/1608.08057) [[astro-ph.CO](https://arxiv.org/archive/astro)].

- Baldi, Marco et al. (2014). “Cosmic degeneracies – I. Joint N-body simulations of modified gravity and massive neutrinos”. In: *Mon. Not. Roy. Astron. Soc.* 440.1, pp. 75–88. DOI: [10.1093/mnras/stu259](https://doi.org/10.1093/mnras/stu259). arXiv: [1311.2588](https://arxiv.org/abs/1311.2588) [astro-ph.CO].
- Bardeen, J. M. et al. (1986). “The statistics of peaks of Gaussian random fields”. In: *ApJ* 304, pp. 15–61. DOI: [10.1086/164143](https://doi.org/10.1086/164143).
- Bardeen, James M. (1980). “Gauge-invariant cosmological perturbations”. In: *Phys. Rev. D* 22 (8), pp. 1882–1905. DOI: [10.1103/PhysRevD.22.1882](https://doi.org/10.1103/PhysRevD.22.1882). URL: <https://link.aps.org/doi/10.1103/PhysRevD.22.1882>.
- Bartelmann, Matthias (2010). “The Dark Universe”. In: *Rev.Mod.Phys.* 82, pp. 331–382. arXiv: [0906.5036](https://arxiv.org/abs/0906.5036) [astro-ph.CO].
- Battye, R. A. and J. Weller (2003). “Constraining cosmological parameters using Sunyaev-Zel’dovich cluster surveys”. In: *Phys. Rev. D* 68.8, 083506, p. 083506. DOI: [10.1103/PhysRevD.68.083506](https://doi.org/10.1103/PhysRevD.68.083506). eprint: [astro-ph/0305568](https://arxiv.org/abs/astro-ph/0305568).
- Baumann, D. et al. (2018). “First Measurement of Neutrinos in the BAO Spectrum”. In: *ArXiv e-prints*. arXiv: [1803.10741](https://arxiv.org/abs/1803.10741).
- Baxter, E. J. et al. (2016). “Constraining the mass-richness relationship of redMaPPer clusters with angular clustering”. In: *MNRAS* 463, pp. 205–221. DOI: [10.1093/mnras/stw1939](https://doi.org/10.1093/mnras/stw1939). arXiv: [1604.00048](https://arxiv.org/abs/1604.00048).
- Bernardeau, F et al. (2002). “Large-scale structure of the Universe and cosmological perturbation theory”. In: *Physics reports* 367.1-3, pp. 1–248.
- Blas, D., J. Lesgourgues, and T. Tram (2011). “The Cosmic Linear Anisotropy Solving System (CLASS). Part II: Approximation schemes”. In: *J. Cosmology Astropart. Phys.* 7, 034, p. 034. DOI: [10.1088/1475-7516/2011/07/034](https://doi.org/10.1088/1475-7516/2011/07/034). arXiv: [1104.2933](https://arxiv.org/abs/1104.2933).
- Bond, J. R. et al. (1991). “Excursion set mass functions for hierarchical Gaussian fluctuations”. In: *ApJ* 379, pp. 440–460. DOI: [10.1086/170520](https://doi.org/10.1086/170520).
- Brinckmann, Thejs and Julien Lesgourgues (2018). “MontePython 3: boosted MCMC sampler and other features”. In: arXiv: [1804.07261](https://arxiv.org/abs/1804.07261) [astro-ph.CO].
- Bullock, J. S. et al. (2001). “Profiles of dark haloes: evolution, scatter and environment”. In: *MNRAS* 321, pp. 559–575. DOI: [10.1046/j.1365-8711.2001.04068.x](https://doi.org/10.1046/j.1365-8711.2001.04068.x). eprint: [astro-ph/9908159](https://arxiv.org/abs/astro-ph/9908159).
- Burgess, C. P. (2013). “The Cosmological Constant Problem: Why it’s hard to get Dark Energy from Micro-physics”. In: *ArXiv e-prints*. arXiv: [1309.4133](https://arxiv.org/abs/1309.4133) [hep-th].
- Carlstrom, J. E., G. P. Holder, and E. D. Reese (2002). “Cosmology with the Sunyaev-Zel’dovich Effect”. In: *ARA&A* 40, pp. 643–680. DOI: [10.1146/annurev.astro.40.060401.093803](https://doi.org/10.1146/annurev.astro.40.060401.093803).
- Carrasco, John Joseph M, Mark P Hertzberg, and Leonardo Senatore (2012). “The effective field theory of cosmological large scale structures”. In: *Journal of High Energy Physics* 2012.9, p. 82.
- Carroll, Sean M. (2001). “The cosmological constant”. In: *Living Rev. Rel.* 4, p. 1. arXiv: [astro-ph/0004075](https://arxiv.org/abs/astro-ph/0004075).
- Cataneo, M. et al. (2015). “New constraints on f(R) gravity from clusters of galaxies”. In: *Phys. Rev. D* 92.4, 044009, p. 044009. DOI: [10.1103/PhysRevD.92.044009](https://doi.org/10.1103/PhysRevD.92.044009). arXiv: [1412.0133](https://arxiv.org/abs/1412.0133).
- Cataneo, M. et al. (2016). “Cluster abundance in chameleon f(R) gravity I: toward an accurate halo mass function prediction”. In: *J. Cosmology Astropart. Phys.* 12, 024, p. 024. DOI: [10.1088/1475-7516/2016/12/024](https://doi.org/10.1088/1475-7516/2016/12/024). arXiv: [1607.08788](https://arxiv.org/abs/1607.08788).
- Chevallier, Michel and David Polarski (2001). “Accelerating universes with scaling dark matter”. In: *Int.J.Mod.Phys. D10*, pp. 213–224. DOI: [10.1142/S0218271801000822](https://doi.org/10.1142/S0218271801000822). arXiv: [gr-qc/0009008](https://arxiv.org/abs/gr-qc/0009008) [gr-qc].
- Cooke, R. J. et al. (2014). “Precision Measures of the Primordial Abundance of Deuterium”. In: *ApJ* 781, 31, p. 31. DOI: [10.1088/0004-637X/781/1/31](https://doi.org/10.1088/0004-637X/781/1/31).

- Corasaniti, P. S. and I. Achitouv (2011). “Toward a Universal Formulation of the Halo Mass Function”. In: *Physical Review Letters* 106.24, 241302, p. 241302. DOI: [10.1103/PhysRevLett.106.241302](https://doi.org/10.1103/PhysRevLett.106.241302). arXiv: [1012.3468](https://arxiv.org/abs/1012.3468) [astro-ph.CO].
- CORE Collaboration et al. (2018a). “Exploring cosmic origins with CORE: Cluster science”. In: *J. Cosmology Astropart. Phys.* 4, 019, p. 019. DOI: [10.1088/1475-7516/2018/04/019](https://doi.org/10.1088/1475-7516/2018/04/019). arXiv: [1703.10456](https://arxiv.org/abs/1703.10456).
- CORE Collaboration et al. (2018b). “Exploring cosmic origins with CORE: Cosmological parameters”. In: *J. Cosmology Astropart. Phys.* 4, 017, p. 017. DOI: [10.1088/1475-7516/2018/04/017](https://doi.org/10.1088/1475-7516/2018/04/017). arXiv: [1612.00021](https://arxiv.org/abs/1612.00021).
- CORE Collaboration et al. (2018c). “Exploring cosmic origins with CORE: Gravitational lensing of the CMB”. In: *J. Cosmology Astropart. Phys.* 4, 018, p. 018. DOI: [10.1088/1475-7516/2018/04/018](https://doi.org/10.1088/1475-7516/2018/04/018). arXiv: [1707.02259](https://arxiv.org/abs/1707.02259).
- CORE Collaboration et al. (2018d). “Exploring cosmic origins with CORE: Inflation”. In: *J. Cosmology Astropart. Phys.* 4, 016, p. 016. DOI: [10.1088/1475-7516/2018/04/016](https://doi.org/10.1088/1475-7516/2018/04/016). arXiv: [1612.08270](https://arxiv.org/abs/1612.08270).
- Costanzi, M. et al. (2013). “Cosmology with massive neutrinos III: the halo mass function and an application to galaxy clusters”. In: *J. Cosmology Astropart. Phys.* 12, 012, p. 012. DOI: [10.1088/1475-7516/2013/12/012](https://doi.org/10.1088/1475-7516/2013/12/012). arXiv: [1311.1514](https://arxiv.org/abs/1311.1514) [astro-ph.CO].
- Crocce, M. et al. (2010). “Simulating the Universe with MICE: the abundance of massive clusters”. In: *MNRAS* 403, pp. 1353–1367. DOI: [10.1111/j.1365-2966.2009.16194.x](https://doi.org/10.1111/j.1365-2966.2009.16194.x). arXiv: [0907.0019](https://arxiv.org/abs/0907.0019).
- Davis, Marc et al. (1985). “The Evolution of Large Scale Structure in a Universe Dominated by Cold Dark Matter”. In: *Astrophys.J.* 292, pp. 371–394. DOI: [10.1086/163168](https://doi.org/10.1086/163168).
- Despali, Giulia et al. (2015). “The universality of the virial halo mass function and models for non-universality of other halo definitions”. In: *Monthly Notices of the Royal Astronomical Society* 456.3, pp. 2486–2504.
- Doroshkevich, A. G. (1970). “Spatial structure of perturbations and origin of galactic rotation in fluctuation theory”. In: *Astrophysics* 6, pp. 320–330. DOI: [10.1007/BF01001625](https://doi.org/10.1007/BF01001625).
- Ebeling, H et al. (1998). “The ROSAT Brightest Cluster Sample—I. The compilation of the sample and the cluster log N—log S distribution”. In: *Monthly Notices of the Royal Astronomical Society* 301.4, pp. 881–914.
- Efstathiou, George and Pablo Lemos (2017). “Problems with KiDS”. In: *arXiv preprint arXiv:1707.00483*.
- Giocoli, C., M. Baldi, and L. Moscardini (2018). “Weak Lensing Light-Cones in Modified Gravity simulations with and without Massive Neutrinos”. In: *ArXiv e-prints: 1806.04681*. arXiv: [1806.04681](https://arxiv.org/abs/1806.04681).
- Grandis, S. et al. (2016). “Information gains from cosmological probes”. In: *Journal of Cosmology and Astroparticle Physics* 2016.05, p. 034. URL: <http://stacks.iop.org/1475-7516/2016/i=05/a=034>.
- Hagstotz, S. et al. (2018). “Joint halo mass function for modified gravity and massive neutrinos I: simulations and cosmological forecasts”. In: *ArXiv e-prints*. arXiv: [1806.07400](https://arxiv.org/abs/1806.07400).
- Hikage, Chiaki, Eiichiro Komatsu, and Takahiko Matsubara (2006). “Primordial non-Gaussianity and analytical formula for Minkowski functionals of the cosmic microwave background and large-scale structure”. In: *The Astrophysical Journal* 653.1, p. 11.
- Hildebrandt, H. et al. (2017). “KiDS-450: cosmological parameter constraints from tomographic weak gravitational lensing”. In: *MNRAS* 465, pp. 1454–1498. DOI: [10.1093/mnras/stw2805](https://doi.org/10.1093/mnras/stw2805). arXiv: [1606.05338](https://arxiv.org/abs/1606.05338).

- Hoekstra, H. et al. (2015). "The Canadian Cluster Comparison Project: detailed study of systematics and updated weak lensing masses". In: *MNRAS* 449, pp. 685–714. DOI: [10.1093/mnras/stv275](https://doi.org/10.1093/mnras/stv275). arXiv: [1502.01883](https://arxiv.org/abs/1502.01883).
- Hogg, D. W. (1999). "Distance measures in cosmology". In: *ArXiv Astrophysics e-prints*. eprint: [astro-ph/9905116](https://arxiv.org/abs/astro-ph/9905116).
- Hojjati, A., L. Pogosian, and G.-B. Zhao (2011). "Testing gravity with CAMB and CosmoMC". In: *J. Cosmology Astropart. Phys.* 8, 005, p. 005. DOI: [10.1088/1475-7516/2011/08/005](https://doi.org/10.1088/1475-7516/2011/08/005). arXiv: [1106.4543](https://arxiv.org/abs/1106.4543) [[astro-ph.CO](https://arxiv.org/abs/astro-ph)].
- Hojjati, A. et al. (2016). "Searching for scalar gravitational interactions in current and future cosmological data". In: *Phys. Rev. D* 93.4, 043531, p. 043531. DOI: [10.1103/PhysRevD.93.043531](https://doi.org/10.1103/PhysRevD.93.043531). arXiv: [1511.05962](https://arxiv.org/abs/1511.05962).
- Hu, W. and J. D. Cohn (2006). "Likelihood methods for cluster dark energy surveys". In: *Phys. Rev. D* 73.6, 067301, p. 067301. DOI: [10.1103/PhysRevD.73.067301](https://doi.org/10.1103/PhysRevD.73.067301). eprint: [astro-ph/0602147](https://arxiv.org/abs/astro-ph/0602147).
- Hu, W. and A. V. Kravtsov (2003). "Sample Variance Considerations for Cluster Surveys". In: *ApJ* 584, pp. 702–715. DOI: [10.1086/345846](https://doi.org/10.1086/345846). eprint: [astro-ph/0203169](https://arxiv.org/abs/astro-ph/0203169).
- Hu, W. and I. Sawicki (2007). "Models of $f(R)$ cosmic acceleration that evade solar system tests". In: *Phys. Rev. D* 76.6, 064004, p. 064004. DOI: [10.1103/PhysRevD.76.064004](https://doi.org/10.1103/PhysRevD.76.064004). arXiv: [0705.1158](https://arxiv.org/abs/0705.1158).
- Hubble, Edwin (1929). "A relation between distance and radial velocity among extragalactic nebulae". In: *Proc.Nat.Acad.Sci.* 15, pp. 168–173.
- Ivezic, Z. et al. (2008). "LSST: from Science Drivers to Reference Design and Anticipated Data Products". In: *arXiv:0805.2366*. arXiv: [0805.2366](https://arxiv.org/abs/0805.2366) [[astro-ph](https://arxiv.org/abs/astro-ph)].
- Joudaki, S. et al. (2017). "KiDS-450: testing extensions to the standard cosmological model". In: *MNRAS* 471, pp. 1259–1279. DOI: [10.1093/mnras/stx998](https://doi.org/10.1093/mnras/stx998). arXiv: [1610.04606](https://arxiv.org/abs/1610.04606).
- Knebe, A. et al. (2011). "Haloes gone MAD: The Halo-Finder Comparison Project". In: *MNRAS* 415, pp. 2293–2318. DOI: [10.1111/j.1365-2966.2011.18858.x](https://doi.org/10.1111/j.1365-2966.2011.18858.x). arXiv: [1104.0949](https://arxiv.org/abs/1104.0949).
- Kopp, Michael et al. (2013). "Spherical collapse and halo mass function in $f(R)$ theories". In: *Phys. Rev. D* 88 (8), p. 084015.
- Kravtsov, A. V. and S. Borgani (2012). "Formation of Galaxy Clusters". In: *ARA&A* 50, pp. 353–409. DOI: [10.1146/annurev-astro-081811-125502](https://doi.org/10.1146/annurev-astro-081811-125502). arXiv: [1205.5556](https://arxiv.org/abs/1205.5556).
- Lesgourgues, J. and S. Pastor (2006). "Massive neutrinos and cosmology". In: *Phys. Rep.* 429, pp. 307–379. DOI: [10.1016/j.physrep.2006.04.001](https://doi.org/10.1016/j.physrep.2006.04.001). eprint: [astro-ph/0603494](https://arxiv.org/abs/astro-ph/0603494).
- Lesgourgues, Julien and Sergio Pastor (2006). "Massive neutrinos and cosmology". In: *Phys. Rept.* 429, pp. 307–379. DOI: [10.1016/j.physrep.2006.04.001](https://doi.org/10.1016/j.physrep.2006.04.001). arXiv: [astro-ph/0603494](https://arxiv.org/abs/astro-ph/0603494).
- Lewis, A. and A. Challinor (2006). "Weak gravitational lensing of the CMB". In: *Phys. Rep.* 429, pp. 1–65. DOI: [10.1016/j.physrep.2006.03.002](https://doi.org/10.1016/j.physrep.2006.03.002). eprint: [astro-ph/0601594](https://arxiv.org/abs/astro-ph/0601594).
- Lewis, Antony, Anthony Challinor, and Anthony Lasenby (2000). "Efficient Computation of CMB anisotropies in closed FRW models". In: *Astrophys. J.* 538, pp. 473–476. DOI: [10.1086/309179](https://doi.org/10.1086/309179). arXiv: [astro-ph/9911177](https://arxiv.org/abs/astro-ph/9911177).
- Linde, A. D. (1982). "A new inflationary universe scenario: A possible solution of the horizon, flatness, homogeneity, isotropy and primordial monopole problems". In: *Physics Letters B* 108, pp. 389–393. DOI: [10.1016/0370-2693\(82\)91219-9](https://doi.org/10.1016/0370-2693(82)91219-9).
- Linder, Eric V. (2003). "Exploring the expansion history of the universe". In: *Phys.Rev.Lett.* 90, p. 091301. DOI: [10.1103/PhysRevLett.90.091301](https://doi.org/10.1103/PhysRevLett.90.091301). arXiv: [astro-ph/0208512](https://arxiv.org/abs/astro-ph/0208512) [[astro-ph](https://arxiv.org/abs/astro-ph)].

- Lombriser, L. et al. (2012). “Constraints on $f(R)$ gravity from probing the large-scale structure”. In: *Phys. Rev. D* 85.12, 124038, p. 124038. DOI: [10.1103/PhysRevD.85.124038](https://doi.org/10.1103/PhysRevD.85.124038). arXiv: [1003.3009](https://arxiv.org/abs/1003.3009).
- Lovelock, David (1972). “The Four Dimensionality of Space and the Einstein Tensor”. In: *Journal of Mathematical Physics* 13.6, pp. 874–876. DOI: [10.1063/1.1666069](https://doi.org/10.1063/1.1666069). eprint: <https://doi.org/10.1063/1.1666069>. URL: <https://doi.org/10.1063/1.1666069>.
- Ma, Chung-Pei and Edmund Bertschinger (1995). “Cosmological perturbation theory in the synchronous and conformal Newtonian gauges”. In: *Astrophys. J.* 455, pp. 7–25. DOI: [10.1086/176550](https://doi.org/10.1086/176550). arXiv: [astro-ph/9506072](https://arxiv.org/abs/astro-ph/9506072).
- MacCrann, Niall et al. (2015). “Cosmic discordance: are Planck CMB and CFHTLenS weak lensing measurements out of tune?” In: *Monthly Notices of the Royal Astronomical Society* 451.3, pp. 2877–2888. DOI: [10.1093/mnras/stv1154](https://doi.org/10.1093/mnras/stv1154). eprint: [/oup/backfile/content_public/journal/mnras/451/3/10.1093/mnras/stv1154/2/stv1154.pdf](https://oup.com/backfile/content_public/journal/mnras/451/3/10.1093/mnras/stv1154/2/stv1154.pdf). URL: <http://dx.doi.org/10.1093/mnras/stv1154>.
- Maggiore, M. and A. Riotto (2010a). “The Halo Mass Function from Excursion Set Theory. I. Gaussian Fluctuations with Non-Markovian Dependence on the Smoothing Scale”. In: *ApJ* 711, pp. 907–927. DOI: [10.1088/0004-637X/711/2/907](https://doi.org/10.1088/0004-637X/711/2/907). arXiv: [0903.1249](https://arxiv.org/abs/0903.1249) [[astro-ph](https://arxiv.org/abs/astro-ph).CO].
- (2010b). “The Halo mass function from Excursion Set Theory. II. The Diffusing Barrier”. In: *ApJ* 717, pp. 515–525. DOI: [10.1088/0004-637X/717/1/515](https://doi.org/10.1088/0004-637X/717/1/515). arXiv: [0903.1250](https://arxiv.org/abs/0903.1250).
- Melin, J.-B. and J. G. Bartlett (2015). “Measuring cluster masses with CMB lensing: a statistical approach”. In: *A&A* 578, A21, A21. DOI: [10.1051/0004-6361/201424720](https://doi.org/10.1051/0004-6361/201424720). arXiv: [1408.5633](https://arxiv.org/abs/1408.5633).
- Mohr, J. J. et al. (2003). “Studying dark energy with galaxy cluster surveys”. In: *Nuclear Physics B Proceedings Supplements* 124, pp. 63–67. DOI: [10.1016/S0920-5632\(03\)02078-4](https://doi.org/10.1016/S0920-5632(03)02078-4). eprint: [astro-ph/0208102](https://arxiv.org/abs/astro-ph/0208102).
- Murata, R. et al. (2018). “Constraints on the Mass-Richness Relation from the Abundance and Weak Lensing of SDSS Clusters”. In: *ApJ* 854, 120, p. 120. DOI: [10.3847/1538-4357/aaaab8](https://doi.org/10.3847/1538-4357/aaaab8). arXiv: [1707.01907](https://arxiv.org/abs/1707.01907).
- Naik, A. P. et al. (2018). “Imprints of Chameleon $f(R)$ Gravity on Galaxy Rotation Curves”. In: *ArXiv e-prints* 1805.12221. arXiv: [1805.12221](https://arxiv.org/abs/1805.12221).
- Nakamura, T. T. and Y. Suto (1997). “Strong Gravitational Lensing and Velocity Function as Tools to Probe Cosmological Parameters — Current Constraints and Future Predictions —”. In: *Progress of Theoretical Physics* 97. DOI: [10.1143/PTP.97.49](https://doi.org/10.1143/PTP.97.49). eprint: [astro-ph/9612074](https://arxiv.org/abs/astro-ph/9612074).
- Nicola, Andrina, Alexandre Refregier, and Adam Amara (2016). “Integrated approach to cosmology: Combining CMB, large-scale structure, and weak lensing”. In: *Physical Review D* 94.8, p. 083517.
- Ostrogradski, M (1850). “M. Ostrogradski, Mem. Ac. St. Petersburg VI 4, 385 (1850).” In: *Mem. Ac. St. Petersburg* VI 4, p. 385.
- Paech, K. et al. (2017). “Cross-correlation of galaxies and galaxy clusters in the Sloan Digital Sky Survey and the importance of non-Poissonian shot noise”. In: *MNRAS* 470, pp. 2566–2577. DOI: [10.1093/mnras/stx1354](https://doi.org/10.1093/mnras/stx1354). arXiv: [1612.02018](https://arxiv.org/abs/1612.02018).
- Peel, A. et al. (2018). “Breaking degeneracies in modified gravity with higher (than 2nd) order weak-lensing statistics”. In: *ArXiv e-prints*. arXiv: [1805.05146](https://arxiv.org/abs/1805.05146).
- Perlmutter, S. et al. (1999). “Measurements of Omega and Lambda from 42 High-Redshift Supernovae”. In: *Astrophys. J.* 517, pp. 565–586. DOI: [10.1086/307221](https://doi.org/10.1086/307221). arXiv: [astro-ph/9812133](https://arxiv.org/abs/astro-ph/9812133).

- Pizzuti, L. et al. (2017). “CLASH-VLT: constraints on $f(R)$ gravity models with galaxy clusters using lensing and kinematic analyses”. In: *J. Cosmology Astropart. Phys.* 7, 023, p. 023. DOI: [10.1088/1475-7516/2017/07/023](https://doi.org/10.1088/1475-7516/2017/07/023). arXiv: [1705.05179](https://arxiv.org/abs/1705.05179).
- Planck Collaboration et al. (2014a). “Planck 2013 results. XX. Cosmology from Sunyaev-Zeldovich cluster counts”. In: *A&A* 571, A20, A20. DOI: [10.1051/0004-6361/201321521](https://doi.org/10.1051/0004-6361/201321521). arXiv: [1303.5080](https://arxiv.org/abs/1303.5080).
- Planck Collaboration et al. (2014b). “Planck 2013 results. XXIX. The Planck catalogue of Sunyaev-Zeldovich sources”. In: *A&A* 571, A29, A29. DOI: [10.1051/0004-6361/201321523](https://doi.org/10.1051/0004-6361/201321523). arXiv: [1303.5089](https://arxiv.org/abs/1303.5089).
- Planck Collaboration et al. (2015). “Planck 2015 results. XXIV. Cosmology from Sunyaev-Zeldovich cluster counts”. In: *ArXiv e-prints*. arXiv: [1502.01597](https://arxiv.org/abs/1502.01597).
- (2016a). “Planck 2015 results. XIII. Cosmological parameters”. In: *A&A* 594, A13, A13. DOI: [10.1051/0004-6361/201525830](https://doi.org/10.1051/0004-6361/201525830). arXiv: [1502.01589](https://arxiv.org/abs/1502.01589).
- Planck Collaboration et al. (2016b). “Planck 2015 results. XVII. Constraints on primordial non-Gaussianity”. In: *A&A* 594, A17, A17. DOI: [10.1051/0004-6361/201525836](https://doi.org/10.1051/0004-6361/201525836). arXiv: [1502.01592](https://arxiv.org/abs/1502.01592).
- Press, W. H. and P. Schechter (1974). “Formation of Galaxies and Clusters of Galaxies by Self-Similar Gravitational Condensation”. In: *ApJ* 187, pp. 425–438. DOI: [10.1086/152650](https://doi.org/10.1086/152650).
- Puchwein, E., M. Baldi, and V. Springel (2013). “Modified-Gravity-GADGET: a new code for cosmological hydrodynamical simulations of modified gravity models”. In: *MNRAS* 436, pp. 348–360. DOI: [10.1093/mnras/stt1575](https://doi.org/10.1093/mnras/stt1575). arXiv: [1305.2418](https://arxiv.org/abs/1305.2418) [[astro-ph.CO](https://arxiv.org/abs/1305.2418)].
- Ratra, Bharat and P. J. E. Peebles (1988). “Cosmological Consequences of a Rolling Homogeneous Scalar Field”. In: *Phys. Rev. D* 37, p. 3406. DOI: [10.1103/PhysRevD.37.3406](https://doi.org/10.1103/PhysRevD.37.3406).
- Riess, Adam G. et al. (1998). “Observational Evidence from Supernovae for an Accelerating Universe and a Cosmological Constant”. In: *Astron. J.* 116, pp. 1009–1038. DOI: [10.1086/300499](https://doi.org/10.1086/300499). arXiv: [astro-ph/9805201](https://arxiv.org/abs/astro-ph/9805201).
- (2016). “A 2.4% Determination of the Local Value of the Hubble Constant”. In: *arXiv:1604.01424*. arXiv: [1604.01424](https://arxiv.org/abs/1604.01424) [[astro-ph.CO](https://arxiv.org/abs/1604.01424)].
- Roncarelli, M., M. Baldi, and F. Villaescusa-Navarro (2018). “The kinematic Sunyaev-Zeldovich effect of the large-scale structure (II): the effect of modified gravity”. In: *ArXiv e-prints*. arXiv: [1805.11607](https://arxiv.org/abs/1805.11607).
- Rozo, Eduardo et al. (2010). “Cosmological Constraints from the SDSS maxBCG Cluster Catalog”. In: *Astrophys. J.* 708, pp. 645–660. DOI: [10.1088/0004-637X/708/1/645](https://doi.org/10.1088/0004-637X/708/1/645). arXiv: [0902.3702](https://arxiv.org/abs/0902.3702) [[astro-ph.CO](https://arxiv.org/abs/0902.3702)].
- Sachs, R. K. and A. M. Wolfe (1967). “Perturbations of a Cosmological Model and Angular Variations of the Microwave Background”. In: *ApJ* 147, p. 73. DOI: [10.1086/148982](https://doi.org/10.1086/148982).
- Schmalzing, Jens, Martin Kerscher, and Thomas Buchert (1995). “Minkowski functionals in cosmology”. In: *arXiv preprint astro-ph/9508154*.
- Schmidt, F. (2010). “Dynamical masses in modified gravity”. In: *Phys. Rev. D* 81.10, 103002, p. 103002. DOI: [10.1103/PhysRevD.81.103002](https://doi.org/10.1103/PhysRevD.81.103002). arXiv: [1003.0409](https://arxiv.org/abs/1003.0409) [[astro-ph.CO](https://arxiv.org/abs/1003.0409)].
- Schmidt, F., A. Vikhlinin, and W. Hu (2009). “Cluster constraints on $f(R)$ gravity”. In: *Phys. Rev. D* 80.8, 083505, p. 083505. DOI: [10.1103/PhysRevD.80.083505](https://doi.org/10.1103/PhysRevD.80.083505). arXiv: [0908.2457](https://arxiv.org/abs/0908.2457) [[astro-ph.CO](https://arxiv.org/abs/0908.2457)].
- Sellentin, E. and R. Durrer (2015). “Detecting the cosmological neutrino background in the CMB”. In: *Phys. Rev. D* 92.6, 063012, p. 063012. DOI: [10.1103/PhysRevD.92.063012](https://doi.org/10.1103/PhysRevD.92.063012). arXiv: [1412.6427](https://arxiv.org/abs/1412.6427).

- Sheth, R. K. and G. Tormen (2002). “An excursion set model of hierarchical clustering: ellipsoidal collapse and the moving barrier”. In: *MNRAS* 329, pp. 61–75. DOI: [10.1046/j.1365-8711.2002.04950.x](https://doi.org/10.1046/j.1365-8711.2002.04950.x). eprint: [astro-ph/0105113](https://arxiv.org/abs/astro-ph/0105113).
- Sheth, Ravi K. and Giuseppe Tormen (1999). “Large scale bias and the peak background split”. In: *Mon. Not. Roy. Astron. Soc.* 308, p. 119. DOI: [10.1046/j.1365-8711.1999.02692.x](https://doi.org/10.1046/j.1365-8711.1999.02692.x). arXiv: [astro-ph/9901122](https://arxiv.org/abs/astro-ph/9901122).
- Shi, X. and E. Komatsu (2014). “Analytical model for non-thermal pressure in galaxy clusters”. In: *MNRAS* 442, pp. 521–532. DOI: [10.1093/mnras/stu858](https://doi.org/10.1093/mnras/stu858). arXiv: [1401.7657](https://arxiv.org/abs/1401.7657).
- Smith, G. P. et al. (2016). “LoCuSS: Testing hydrostatic equilibrium in galaxy clusters”. In: *MNRAS* 456, pp. L74–L78. DOI: [10.1093/mnrasl/slv175](https://doi.org/10.1093/mnrasl/slv175). arXiv: [1511.01919](https://arxiv.org/abs/1511.01919).
- Springel, V. et al. (2001). “Populating a cluster of galaxies - I. Results at $z=0$ ”. In: *MNRAS* 328, pp. 726–750. DOI: [10.1046/j.1365-8711.2001.04912.x](https://doi.org/10.1046/j.1365-8711.2001.04912.x). eprint: [arXiv:astro-ph/0012055](https://arxiv.org/abs/astro-ph/0012055).
- Springel, Volker (2005). “The cosmological simulation code GADGET-2”. In: *Mon. Not. Roy. Astron. Soc.* 364, pp. 1105–1134. arXiv: [astro-ph/0505010](https://arxiv.org/abs/astro-ph/0505010).
- Srednicki, Mark (2007). *Quantum field theory*. Cambridge University Press.
- Starobinsky, Alexei A. (1980). “A new type of isotropic cosmological models without singularity”. In: *Phys. Lett.* B91, pp. 99–102. DOI: [10.1016/0370-2693\(80\)90670-X](https://doi.org/10.1016/0370-2693(80)90670-X).
- Takada, M. and D. N. Spergel (2014). “Joint analysis of cluster number counts and weak lensing power spectrum to correct for the super-sample covariance”. In: *MNRAS* 441, pp. 2456–2475. DOI: [10.1093/mnras/stu759](https://doi.org/10.1093/mnras/stu759). arXiv: [1307.4399](https://arxiv.org/abs/1307.4399).
- Tinker, J. et al. (2008). “Toward a Halo Mass Function for Precision Cosmology: The Limits of Universality”. In: *ApJ* 688, 709–728, pp. 709–728. DOI: [10.1086/591439](https://doi.org/10.1086/591439). arXiv: [0803.2706](https://arxiv.org/abs/0803.2706).
- Verlinde, Erik (2017). “Emergent gravity and the dark universe”. In: *SciPost Physics* 2.3, p. 016.
- Viel, Matteo, Martin G. Haehnelt, and Volker Springel (2010). “The effect of neutrinos on the matter distribution as probed by the Intergalactic Medium”. In: *JCAP* 1006, p. 015. DOI: [10.1088/1475-7516/2010/06/015](https://doi.org/10.1088/1475-7516/2010/06/015). arXiv: [1003.2422](https://arxiv.org/abs/1003.2422) [[astro-ph](https://arxiv.org/abs/astro-ph)].
- Vikhlinin, A. et al. (2009). “Chandra Cluster Cosmology Project II: Samples and X-ray Data Reduction”. In: *Astrophys. J.* 692, pp. 1033–1059. DOI: [10.1088/0004-637X/692/2/1033](https://doi.org/10.1088/0004-637X/692/2/1033). arXiv: [0805.2207](https://arxiv.org/abs/0805.2207) [[astro-ph](https://arxiv.org/abs/astro-ph)].
- Villaescusa-Navarro, F. et al. (2017). “The imprint of neutrinos on clustering in redshift-space”. In: *ArXiv e-prints*. arXiv: [1708.01154](https://arxiv.org/abs/1708.01154).
- von Braun-Bates, F. et al. (2017). “The f(Script R) halo mass function in the cosmic web”. In: *J. Cosmology Astropart. Phys.* 3, 012, p. 012. DOI: [10.1088/1475-7516/2017/03/012](https://doi.org/10.1088/1475-7516/2017/03/012). arXiv: [1702.06817](https://arxiv.org/abs/1702.06817).
- von der Linden, A. et al. (2014). “Robust weak-lensing mass calibration of Planck galaxy clusters”. In: *MNRAS* 443, pp. 1973–1978. DOI: [10.1093/mnras/stu1423](https://doi.org/10.1093/mnras/stu1423). arXiv: [1402.2670](https://arxiv.org/abs/1402.2670).
- Weinberg, S. (2008). *Cosmology*. Oxford University Press.
- Weinberg, Steven (1989). “The cosmological constant problem”. In: *Rev. Mod. Phys.* 61, pp. 1–23. DOI: [10.1103/RevModPhys.61.1](https://doi.org/10.1103/RevModPhys.61.1).
- Wetterich, C. (1988). “Cosmology and the Fate of Dilatation Symmetry”. In: *Nucl. Phys.* B302, p. 668. DOI: [10.1016/0550-3213\(88\)90193-9](https://doi.org/10.1016/0550-3213(88)90193-9).
- Wilcox, H. et al. (2015). “The XMM Cluster Survey: testing chameleon gravity using the profiles of clusters”. In: *MNRAS* 452, pp. 1171–1183. DOI: [10.1093/mnras/stv1366](https://doi.org/10.1093/mnras/stv1366). arXiv: [1504.03937](https://arxiv.org/abs/1504.03937).

- Winther, Hans A. et al. (2015). "Modified Gravity N-body Code Comparison Project". In: *Mon. Not. Roy. Astron. Soc.* 454.4, pp. 4208–4234. DOI: [10.1093/mnras/stv2253](https://doi.org/10.1093/mnras/stv2253). arXiv: [1506.06384](https://arxiv.org/abs/1506.06384) [[astro-ph](https://arxiv.org/archive/astro-ph).[C0](https://arxiv.org/archive/astro-ph)].
- Woodard, R. (2007). "Avoiding Dark Energy with 1/R Modifications of Gravity". In: *The Invisible Universe: Dark Matter and Dark Energy*. Ed. by L. Papantonopoulos. Vol. 720. Lecture Notes in Physics, Berlin Springer Verlag, p. 403. eprint: [astro-ph/0601672](https://arxiv.org/abs/astro-ph/0601672).
- Zennaro, M. et al. (2017). "Initial conditions for accurate N-body simulations of massive neutrino cosmologies". In: *MNRAS* 466, pp. 3244–3258. DOI: [10.1093/mnras/stw3340](https://doi.org/10.1093/mnras/stw3340). arXiv: [1605.05283](https://arxiv.org/abs/1605.05283).
- Zhao, G.-B. et al. (2009). "Searching for modified growth patterns with tomographic surveys". In: *Phys. Rev. D* 79.8, 083513, p. 083513. DOI: [10.1103/PhysRevD.79.083513](https://doi.org/10.1103/PhysRevD.79.083513). arXiv: [0809.3791](https://arxiv.org/abs/0809.3791).